

# ROBOTIC REFILL FRICTION STIR SPOT WELDING FOR AEROSPACE APPLICATIONS

A Dissertation by

Guruvignesh Lakshmi Balasubramaniam

Bachelor of Engineering, Karpagam College of Engineering, India, 2011

Submitted to the Department of Industrial Engineering  
and the faculty of the Graduate School of  
Wichita State University  
in partial fulfillment of  
the requirements for the degree of  
Doctor of Philosophy

December 2021

© Copyright 2021 by Guruvignesh Lakshmi Balasubramaniam

All Rights Reserved

## ROBOTIC REFILL FRICTION STIR SPOT WELDING FOR AEROSPACE APPLICATIONS

The following faculty members have examined the final copy of this dissertation for form and content, and recommend that it be accepted in partial fulfillment of the requirement for the degree of Doctor of Philosophy with a major in Industrial Engineering

Enkhsaikhan Boldsaikhan, Committee Chair

Krishna Krishnan, Committee Member

Gamal Weheba, Committee Member

Rajeev Nair, Committee Member

Saideep Nannapaneni, Committee Member

Accepted for the College of Engineering

Dr. Anthony Muscat, Dean

Accepted for the Graduate School

Dr. Coleen Pugh, Dean

## ACKNOWLEDGEMENTS

I would like to express my gratitude to my advisor Dr. Enkhsaikhan Boldsaikhan for the opportunity, guidance and support given by him throughout the project. Second, I would like to thank my dissertation committee members Dr. Krishna Krishnan, Dr. Gamal Weheba, Dr. Rajeev Nair, and Dr. Saideep Nannapaneni for providing helpful feedback. They have been great teachers who have prepared me to get to this place in my academic life. This project would not be nearly as good without their help. Third, I would like to thank graduate students Saravana Prabu Ravichandran, Logeshwar Pounraj, Sanjay Kumar Madras Karunamurthy and Graciano Fernandez Joseph Rosario for their help and support during the project. And finally, I would like to thank my parents, Balasubramaniam and Lakshmi, and my brother Suriya Prakaash for their continued support and encouragement. Without such a team behind me, I doubt that I would be in this place today.

I would also like to acknowledge and thank Kawasaki Heavy Industries and CFSP (Centre for Friction Stir Processing) for funding this project. Also, I thank NIAR (National Institute of Aviation Research) for providing their space and time in developing the project.

## ABSTRACT

The consumption of high-strength aluminum alloys in aerospace industries is increasing and refill friction stir spot welding is found to be a suitable joining technology for aerospace aluminum alloys. Currently, aerospace industries use riveting to assemble aircraft components as it bears well-established standards and specifications. Refill Friction stir Spot Welding (RFSSW) that can replace riveting is an emerging solid-state spot-welding technology that thermo-mechanically produces a molecular level bond between workpieces. RFSSW does not require any filler or foreign materials and hence no additional weight is added to the assembly. There is no major lack of fusion or material deterioration exhibited by RFSSW as it does not involve phase transitions during the welding process in general. Unlike the conventional friction stir spot welding, RFSSW produces a spot joint with a flush surface finish that is free from a key or exit hole. Kawasaki Heavy Industries (KHI) has developed a robotic system with an RFSSW end effector. The aim of this study is to evaluate the mechanical properties of refill friction stir spot welds produced by the robotic RFSSW system with an emphasis on aerospace applications. As the aerospace applications require rigorous standards and specification, this study also explores potential methodologies for developing standards and specifications for RFSSW

*Keywords:* Refill Friction Stir Spot Welding; Refill Friction Stir Spot Joining; Aerospace Aluminum Alloy; Robotic Spot Welding; Aerospace Manufacturing

## TABLE OF CONTENTS

Chapter	Page
1. Chapter 1: INTRODUCTION	
i. REFILL FRICTION STIR SPOT WELDING TECHNIQUE .....	1
ii. RIVETING TECHNIQUE .....	6
2. Chapter 2: EFFECTS OF REFILL FRICTION STIR SPOT WELD SPACING AND EDGE MARGIN OF MULTI-SPOT-WELDED PANELS	
i. OBJECTIVE.....	12
ii. MATERIALS AND METHODOLOGY.....	12
iii. RESULTS AND DISCUSSION.....	17
iv. SUMMARY.....	29
3. Chapter 3: COMPARISON OF REFILL FRICTION STIR SPOT WELDING VERSUS RIVETING IN AIRCRAFT APPLICATIONS	
i. OBJECTIVE .....	32
ii. MATERIALS AND METHODOLOGY .....	32
iii. RESULTS .....	37
iv. DISCUSSION ... ..	44
v. SUMMARY .....	51

TABLE OF CONTENTS (continued)

Chapter	Page
4. Chapter 4: FATIGUE PERFORMANCE OF REFILL FRICTION STIR SPOT WEILDING	
i. OBJECTIVE .....	53
ii. MATERIALS AND METHODOLOGY .....	53
iii. RESULTS AND DISCUSSION .....	59
iv. SUMMARY .....	74
5. Chapter 5: FATIGUE PERFORMANCE OF REFILL FRICTION STIR SPOT WEILDING	
i. INTRODUCTION .....	76
ii. OBJECTIVE .....	77
i. MATERIALS AND METHODOLOGY .....	77
ii. RESULTS .....	87
iii. DISCUSSION .....	108
iv. SUMMARY .....	115
REFERENCES .....	118

## LIST OF TABLES

Table	Page
1. Mechanical Properties of AA7075-T6 .....	13
2. DoE runs for Making Nine-Spot-Weld Panels .....	14
3. Coupon Quantities .....	38
4. Chemical Composition of AA6013-T6 and AA2029-T8 .....	54
5. Mechanical Properties of AA6013-T6 and AA2029-T8. ....	54
6. DoE Factors and their Three Levels .....	56
7. DoE Test Results. (NP-Nugget Pullout; IF – Interfacial Failure).....	61
8. Analysis of Variance (ANOVA) for Failure Load .....	65
9. DoE Validation Experiment Results (13 coupons) .....	70
10. Chemical Composition of AA6013-T6 and AA2029-T8 .....	78
11. Mechanical Properties of AA6013-T6 and AA2029-T8 .....	78
12. Guided Static Test results of Four-Spot Coupons per NASM1312-21 .....	90
13. Guided Fatigue Test Results of Four-Spot Coupons per NASM1312-21 .....	91
14. Guided Fatigue Test Results of 45% Load Level Four-Spot coupons .....	95

## LIST OF FIGURES

Figure	Page
1. Kawasaki robot with RFSSW end effector .....	3
2. RFSSW Process Stages .....	3
3. Cross-sectional image of refill spot weld .....	5
4. Cross-sectional microhardness map of refill spot weld .....	5
5. Protruding head and flush head rivets .....	7
6. Aluminum rivet with flush head and front & back sides of riveted sample	8
7. Kuka robot (Drilling Process) .....	9
8. Deburring tool .....	10
9. Riveting Tool Kit .....	11
10. Heat affected zone (HAZ) and spot weld spacing (Pitch) .....	15
11. Heat affected zone (HAZ) and edge margin (EM) .....	15
12. Nine-spot-weld panel configuration and cut plan .....	17
13. Cross-section specimen and microhardness measurement lines .....	17
14. Examples of nine-spot-weld panels with different edge margins (EM) .....	18

LIST OF FIGURES (continued)

Figure	Page
15. Edge swelling caused by 1D edge margin (EM) during RFSSW .....	20
16. Surface dent of 1D edge margin and surface dent of 2D edge margin panels ..	20
17. Side view of unguided lap-shear static pull testing of single-spot coupon .....	21
18. Main effects plot of pitch and edge margin (EM) .....	23
19. Estimated response surface of pitch and edge margin (EM) .....	24
20. Top view and bottom view of nugget pullout (NP) failure of 3D-Pitch 2D-EM coupon after static pull testing .....	24
21. Top view and bottom view of top sheet breakdown (TSB) failure of 2D-Pitch 1.5D-EM coupon after static pull testing .....	25
22. Examples of two-spot cross-section specimens .....	25
23. Microhardness values of 2D pitch cross-section specimens .....	26
24. Microhardness values of 3D pitch cross-section specimens .....	27
25. Microhardness values of 4D pitch cross-section specimens .....	28
26. Lap joint configurations: (a) refill spot weld configuration and (b) rivet joint configuration .....	33

LIST OF FIGURES (continued)

Figure	Page
27. Two-spot coupon configurations in accordance with NASM-1312-4.....	35
28. Cross-coupon configurations in accordance with ISO-14272 .....	36
29. Four-spot coupon configurations in accordance with NASM-1312-21 .....	36
30. Mechanical test setups .....	37
31. Box-whisker plots of static load test results.....	39
32. Two-spot coupons before and after static load lap shear tests .....	40
33. Cross coupons before and after static cross-tension load tests .....	41
34. Fatigue test results.....	41
35. Four-spot coupons before and after fatigue lap shear pull tests.....	42
36. Refill spot weld regions .....	45
37. Mechanical failures of refill spot welds .....	47
38. Refill spot weld cross-section schematics with external loading conditions, including pure shear loading, pure tension loading, and shear-and-tension loading .....	48
39. Schematics of refill spot weld failures .....	49
40. Schematics of refill spot weld failures (coupled shear-and-tension loading) ....	49

## LIST OF FIGURES (continued)

Figure	Page
41. Material preparation.....	55
42. Face centered central composite design (15+1 runs) .....	57
43. A single spot straight coupon configuration and weld fixture setup.....	58
44. Unguided static lap-shear pull test setup.....	59
45. Front and Back of Run-3 Coupons and Run-4 Coupons .....	62
46. Front and Back of Run-9 Coupons and Run-10 Coupons .....	63
47. Run-10 Coupons and Run-9 Coupons .....	64
48. Main effects plot, normal probability, and residual plot.....	67
49. Standardized Pareto chart for failure load.....	69
50. Front and back of additional Run-1 coupons .....	71
51. Front and back of additional Run-9 coupons after static lap-shear tests .....	72
52. Front and back of Run-17 coupons after unguided static lap-shear pull tests ...	73
53. Unguided static lap-shear pull test results of DoE validation experiment .....	74

LIST OF FIGURES (continued)

Figure	Page
54. Material preparation.....	79
55. NASM-1312-21 coupon configuration and weld clamp setup .....	81
56. NASM-1312-21 guided lap-shear pull test setup.....	82
57. Welded 4 spot coupons .....	82
58. Notch Geometry .....	83
59. Coupon configuration for the crack growth test analysis .....	85
60. NASM-1312-21 lap-shear pull test setup. Weld fixture setup for crack growth analysis test coupons.....	85
61. Front and back of the top sheet parent metal coupons .....	86
62. Front and back of the bottom sheet parent metal coupons.....	86
63. Front and back of the top sheet welded coupons .....	87
64. Front and backside of the bottom sheet welded coupons.....	87
65. Top-Sheet Tensile Failure (TSTF).....	88
66. Crack initiating in TMAZ/HAZ.....	89

LIST OF FIGURES (continued)

Figure	Page
67. Guided fatigue test results of four-spot coupons per NASM1312-21 .....	92
68. Front and back of Coupon 14.....	92
69. Front and back of Coupon 15 .....	93
70. Crack initiating and propagating through the TMAZ/HAZ in the top sheet .....	93
71. 4 spot coupon with TSTF and failure surfaces showing the crack initiation, propagation, and catastrophic rupture .....	94
72. Crack growth vs the number of cycles to failure of the top sheet coupons .....	98
73. Crack growth vs the number of cycles to failure of the bottom sheet coupons..	98
74. Crack growth vs the number of cycles to failure (top sheet welded coupons vs bottom sheet welded coupons) .....	99
75. Crack propagating through top sheet parent metal coupon (Left). Top sheet parent metal after failure (Right) .....	111
76. Front and back of the failure surfaces of top sheet parent metal coupon.....	111
77. Crack propagating through the HAZ in the top sheet welded coupon (Left). Top sheet parent welded coupon after complete rupture (Right) .....	112
78. Front and back of the failure surfaces of top sheet welded coupon .....	112
79. Crack propagating through the Bottom sheet parent metal coupon (Left). Bottom sheet parent metal after failure (Right) .....	113
80. Front and back of the failure surfaces of bottom sheet parent metal coupon.....	113

LIST OF FIGURES (continued)

Figure	Page
81. Crack propagating through the HAZ in the bottom sheet welded coupon (Left). Bottom sheet parent welded coupon after complete rupture (Right).....	114
82. Front and back of the failure surfaces of bottom sheet welded coupon.....	114

## CHAPTER 1: INTRODUCTION

### Refill Friction Stir Spot Welding Technique

The consumption of aluminum alloys is growing as they are lightweight and easy to recycle. This attracts interest in developing welding technologies for aluminum alloys to fabricate joints with satisfactory mechanical properties [1]. Aluminum alloys welded with conventional fusion welding techniques experience the formation of brittle intermetallic compounds that usually lead to severe intermetallic cracking [2]. Hence, it is difficult to weld aluminum alloys using conventional fusion welding techniques.

Mazda Motor Corporation and Kawasaki Heavy Industry (KHI) [3, 4] have documented a friction stir spot welding (FSSW) method for joining aluminum alloys for automotive applications. FSSW is a solid-state welding technique as a variant of friction stir welding (FSW) that was invented by The Welding Institute in 1991 [5]. FSSW leaves behind a keyhole, which is a tool exit hole at the center of the spot weld. A keyhole causes stress concentrations that reduce the structural integrity of the assembly. A keyhole is also susceptible to corrosion as its internal surfaces are difficult to reach for painting. Therefore, refilling strategies for alleviating a keyhole have been explored by numerous researchers [6, 7, and 8].

Refill Friction Stir Spot Welding (RFSSW) that can replace riveting is an emerging solid-state spot-welding technology that thermo-mechanically produces a molecular-level bond between workpieces. RFSSW does not require any filler or foreign materials and hence no additional weight is added to the assembly. There is no major lack of fusion or material deterioration exhibited by RFSSW as it does not involve phase transitions during the welding process in general. Unlike the conventional friction stir spot welding, RFSSW produces a spot joint with a flush surface finish that is free from a key or exit hole. Kawasaki Heavy Industries (KHI) [7,8] has

developed a robotic system with an RFSSW end effector. Researchers [7, 8, 9, 10] successfully demonstrated the use of RFSSW for joining high-strength aerospace aluminum alloys.

The robotic RFSSW system used in this study is shown in Fig. 1.1. A weld tool consisting of a retractable probe, a shoulder and a cylindrical clamp is used for RFSSW. The size of a refill spot weld is defined by the tool diameter and its plunge depth. The RFSSW process consists of 5 stages as shown in Fig 1.2.

Stage 1: It involves workpiece clamping and preheating. The workpieces are firmly clamped between the backing anvil and the clamp tip. Then, the rotating weld tool touches down and resides on top of the work-piece surface for a certain period of time to preheat the material through friction.

Stage 2: In this stage, the shoulder plunges into the workpiece and the probe retracts. The retraction of the probe opens up a cavity to accommodate the material displaced by the shoulder. When the targeted plunge depth is reached, the weld tool may dwell in that position for a certain period of time. The shoulder-plunging process requires a higher plunge force. However, the shoulder-plunging process stirs more volume of material and can produce stronger joints [11]. In this study, the shoulder-plunging process was employed in Stage 2.

Stage 3: In the third stage, the rotating probe and the shoulder move in the reverse directions and re-inject the displaced material back into the process / weld zone. Furthermore, to improve the flushness of the surface, the probe and the shoulder may keep moving in the reverse directions until they slightly exceed their aligned position [11].

Stage 4: In Stage 4, the probe and the shoulder are aligned with each other right on top of the workpiece top surface to establish the final flush surface finish.

Stage 5: In the fifth stage, the weld tool is removed.

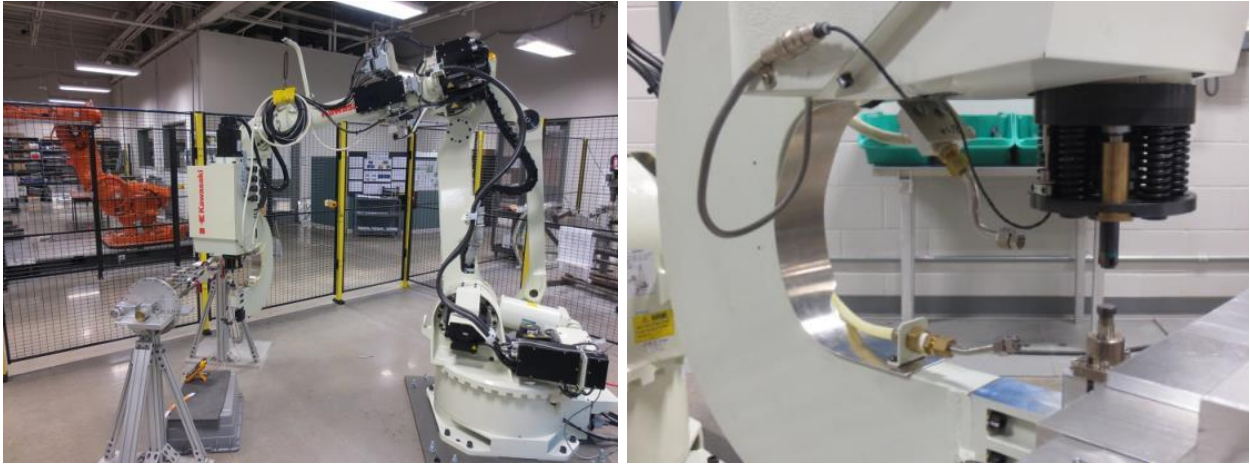


**Fig.1.1: Kawasaki robot (left) with RFSSW end effector (right).**

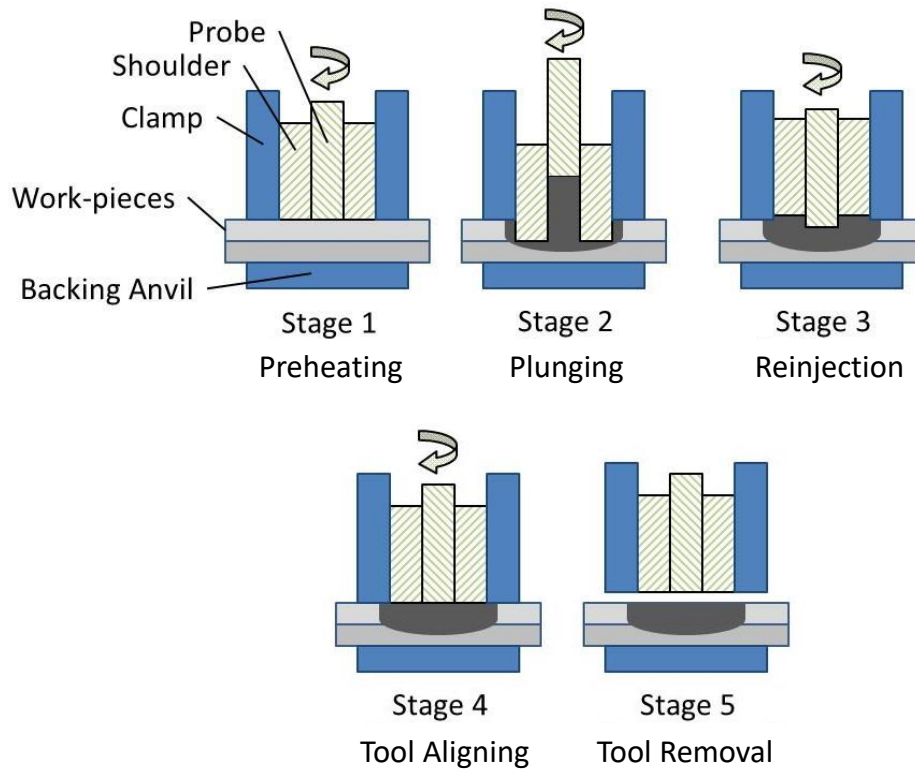


**Fig. 1.2: RFSSW process stages.**

RFSSW imposes three distinct weld zones on heat-treatable aluminum alloys, which are a Heat Affected Zone (HAZ), a Thermo-Mechanically Affected Zone (TMAZ), and a weld nugget. The heat affected zone (HAZ) is a region of the heat-treatable base metal that spans around the weld as its outermost shell. It is affected by the process heat but not the mechanical stirring. The thermo-mechanically affected zone (TMAZ) is an interlayer between HAZ and the weld nugget. It is affected by the process heat as well as the mechanical stirring involved in the weld nugget. The weld nugget is located at the center of the weld, where the tool forges and stirs the plasticized material during welding. It experiences the greatest heat and plastic deformation that leads to significant grain refinement and re-precipitation. The size of the RFSSW weld nugget is defined by the diameter of the weld tool and its plunge depth. The metal grain size usually coarsens in TMAZ and HAZ during the welding process. However, the grain size becomes fine and equiaxed in the weld nugget due to dissolution and re-precipitation involved in there.

Fonda and Bingert [12] investigated the TMAZ-and-HAZ boundary of FSW of AA2519 to determine its effects on the mechanical properties of the weld. The micrographic map revealed that the location of the fracture was at the boundary between TMAZ and HAZ, where the metal grains are coarser [12]. According to Paglia and Buchheit [13], the sensitization in HAZ is responsible for the corrosion susceptibility of FSW of aluminum alloys. Khodir and Shibayanagi [14] studied the microstructure and the mechanical properties of FSW of dissimilar AA2024-T3 and AA7075-T6. They found that the hardness values of FSW increase with the tool travel speed [14].

FSSW demonstrates a higher weld strength with a lower tool spindle speed [15-18]. However, a too low spindle speed may induce an insufficient heat input and may cause a lack-of-consolidation defect or tool breakage. The failure load of dissimilar-aluminum-alloy-spot-friction welds

increased with increased processing time [19]. Literatures on the effects of various factors on the friction stir spot weld strengths are diverse. The presented research focuses on the effects of the refill spot joint spacing and edge margin on the mechanical properties of multi-spot-weld panels.

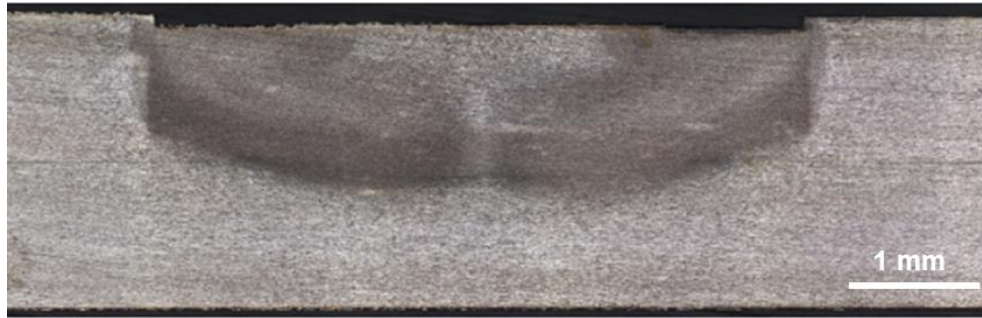


**Fig. 1.3: Cross-sectional image of refill spot weld. The top and bottom sheets are 1.6mm-thick AA7075-T6.**

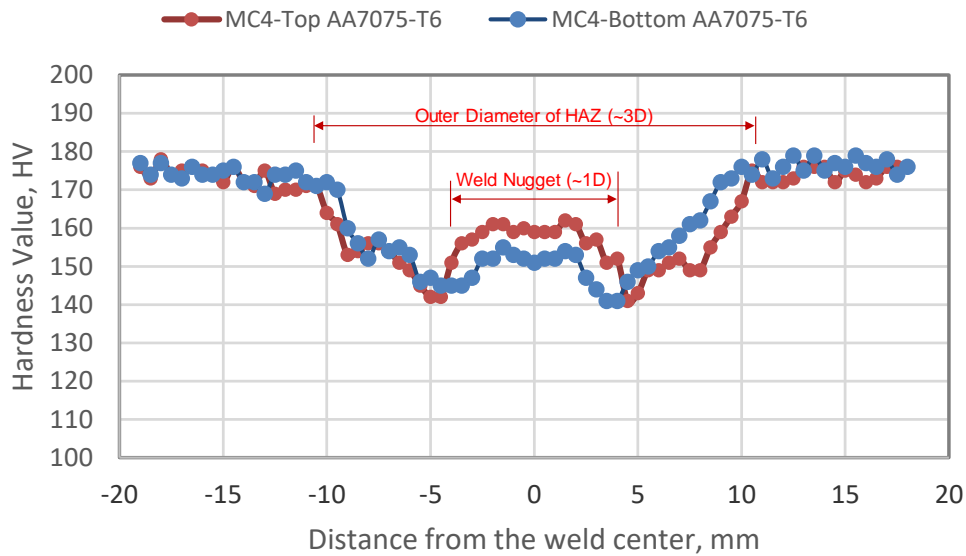


**Fig. 1.4: Cross-sectional microhardness map of refill spot weld. The hardness values are taken from the midplane lines of the top sheet and the bottom sheet of the weld cross-section in Fig. 1.3.**

As RFSSW is a derivative of FSW and FSSW, RFSSW exhibits mechanical and microstructural properties similar to that of FSW and FSSW. Under an extreme external load, a refill spot weld usually starts to fail in TMAZ / HAZ, where the metal grains are coarser. Therefore, the extent of HAZ / TMAZ of a refill spot weld is critical to defining a spot weld spacing and an edge margin for multi-spot-weld structures. The cross-sectional image of a refill spot weld in Fig. 1.3 and its microhardness map in Fig. 1.4 suggest that the HAZ diameter is about 3 times the diameter of the refill spot weld. The top and bottom sheets of the refill spot weld are 1.6mm-thick AA7075-T6. Optimized RFSSW parameters were used for joining 1.6mm-thick AA7075-T6 to 1.6mm-thick AA7075-T6. In Fig.1.4, D is the diameter of the refill spot weld, which is 7 mm.

### **Riveting Technique**

On the other hand, Riveting is a widely used fastening method for making load-bearing mechanical joints of aircraft structures. It has well-established standards and specifications for aerospace applications. The performance data of rivets can be found in the MMPDS (Metallic Materials Properties Development and Standardization) documents [25]. The MMPDS documents are maintained by a committee of industries and government agencies. The MMPDS document [25] identifies five types of mechanical fasteners. They are Solid/round head rivets, Semi- tubular rivets, Blind rivets, Oscar rivets, Drive rivet, Flush rivet, Friction-lock rivet, Rivet alloys, shear strengths, and driving condition.

- Solid rivets – Solid rivets are single-piece fasteners that are installed by mechanically clenching one end.
- Threaded fasteners – Threaded fasteners are any re-usable threaded pins that can be easily removed and installed.

- Swaged collar fasteners – A swaged collar fastener consists of multiple pieces including a solid pin and a malleable collar that is swaged to grip the joint.
- Blind fasteners – A blind fastener has a self-upsetting mechanism that can be used for assemblies accessible from one side only.
- Special fasteners – The special fasteners include sleeves, panel bolts, and inserts that are less commonly used in primary aircraft structures than the four categories listed above.

Mechanical fasteners listed above can also be categorized into protruding head fasteners and flush head fasteners. A protruding head fastener has a head that protrudes above the workpiece surface, while a flush head fastener has a head that goes into a countersunk hole for a flush surface finish as displayed in Fig 1.5. For our application, we are using flush rivets shown in Fig 1.6.

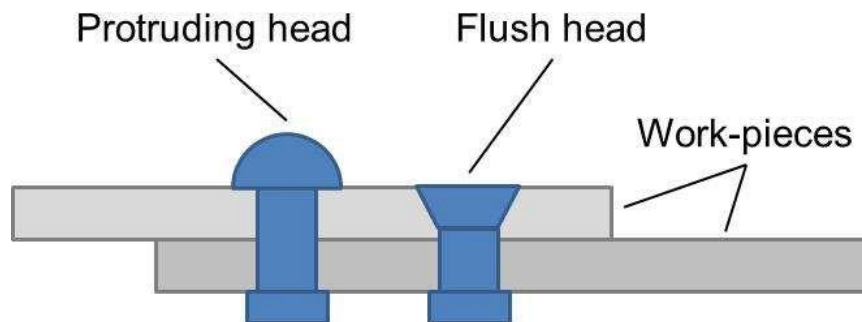


**Fig. 1.5: Protruding head and flush head rivets.**



**Fig. 1.6: MS20426-AD5 aluminum rivet with flush head (left) and front & back sides of riveted sample (right). The rivets may look larger than their original sizes.**

There are different steps in the riveting process. They are drilling a hole, deburring, fastener insertion and fastener clinching. This method is used in aerospace because of its simplicity and reliability in spite of its tedious process. The aerospace industry uses riveting process to fix skin and stiffeners of airplanes. The skin is made up of AA7075-T6 1.27mm. Aluminum (blended with small quantities of other metals) is used on most types of aircraft because it is lightweight and strong. Also, Aluminum alloys do not corrode. The stiffeners are made up of AA2024-T3 1.6mm. It is used in applications requiring high strength to weight ratio, as well as good fatigue resistance.

## Hole Drilling

After the selection of rivets, the next step is to drill hole to the size of the rivet. The Kuka robots were preferred to drill the holes due to their accuracy and reliability. The Kuka robot is shown in Fig 1.7.



**Fig. 1.7: Kuka robot**

## Deburring

It is a process of removing burrs that are produced after the drilling process. Deburring eliminates sharp edges so that the worker can handle it without the possibility of getting injured because of it. Also, Burrs cause more stress to be concentrated at the edges of the holes, decreasing resistance to fracture, and shortening its fatigue life. The tool which is used to deburr is shown in the Fig 1.8.



**Fig. 1.8: Deburring tool.**

### **Clenching**

The next step is fastener insertion and clamping. In the drilled hole the rivets are inserted, and it is clamped using cleco clamps. Then the rivet is clinched using a pneumatic hammer. For the pneumatic hammer, the desired pressure level is fixed, and the rivets are clinched. These are the different steps involved in the riveting process. The riveting tool kit that was used is shown in the Fig. 1.9.

## Riveting Tools



**Fig. 1.9: Riveting Tool Kit.**

## **CHAPTER 2: EFFECTS OF REFILL FRICTION STIR SPOT WELD SPACING AND EDGE MARGIN OF MULTI-SPOT-WELDED PANELS**

### **OBJECTIVE**

The aim of the study is to investigate the effects of the refill friction stir spot weld spacing and edge margin on mechanical properties of multi-spot-welded panels with an emphasis on aerospace applications. The study uses a baseline aerospace aluminum alloy, AA7075-T6, used in aircraft structures [25]. A spot weld spacing (pitch) is a center-to-center distance between two adjacent spot welds in the same row. An edge margin (EM) is a center-to-edge distance between a spot weld and the material edge. The experimental strategy uses Design of Experiments (DoE) to characterize the failure loads of multi-spot-welded AA7075-T6 panels in terms of the spot weld spacing, the edge margin, and the spot weld HAZ. The multi-spot-welded panels are subjected to static lap-shear pull tests and Vickers microhardness tests to identify their failure loads and the spot weld HAZ patterns, respectively. The spot weld spacing (pitch) and the edge margin are studied in relation to the size of the HAZ. As mentioned earlier, the RFSSW process leaves behind a thermal “imprint” as HAZ in heat-treatable aluminum alloys.

### **MATERIALS AND METHODOLOGY**

Panels used in this research are bare 1.6mm-thick AA7075-T6 sheets that have mechanical properties listed in Table 1. AA7075-T6 is a generic stiffener material of aircraft structures. Panels were refill friction stir spot welded in pairs in a lap joint configuration. The RFSSW process used a weld tool that consists of a retractable pin with a diameter of 4 mm and a sleeve shoulder with a diameter of 7 mm. The shoulder-plunging method was used for RFSSW. The weld parameters for making all refill spot joints are as follows.

- Plunge depth: 1.9 mm
- Probe speed: 4 mm/s
- Spindle speed: 1400 rpm

They are optimum parameters for joining 1.6mm-thick AA7075-T6. In accordance with Fig. 4, each refill spot joint exhibits a heat affected zone that covers a radial region with a diameter of three times the diameter of the spot joint.

**Table 2.1: Mechanical properties of AA7075-T6**

	<b>AA7075-T6</b>
<b>Hardness Value, Vickers</b>	175 HV
<b>Ultimate Tensile Strength</b>	572 Mpa
<b>Tensile Yield Strength</b>	503 Mpa
<b>Elongation</b>	11%

**Table 2.2: DoE runs for making nine-spot-weld panels. D (=7mm) is the spot weld diameter.**

<b>Run #</b>	<b>Edge Margin</b>	<b>Spot Spacing (Pitch)</b>
<b>1</b>	1D (= 7mm)	2D (= 14mm)
<b>2</b>	1D	3D
<b>3</b>	1D	4D
<b>4</b>	1.5D	2D
<b>5</b>	1.5D	3D
<b>6</b>	1.5D	4D
<b>7</b>	2D	2D
<b>8</b>	2D	3D
<b>9</b>	2D	4D

The experimentation used a Design of Experiments (DoE) method. A  $3^2$  full factorial design was employed with two design factors, which are the spot spacing (pitch) and the edge margin (EM). The spot spacing or pitch defines a center-to-center distance between two adjacent spot joints in the same row. The edge margin defines a center-to-edge distance between a spot weld and the material edge. The  $3^2$  full factorial design consists of nine DoE runs as listed in Table 2.

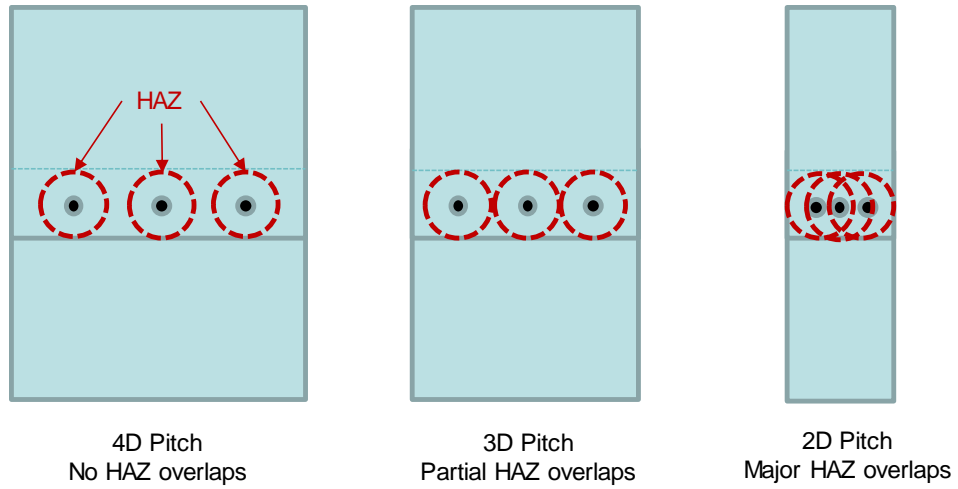


**Fig. 2.1: Heat affected zone (HAZ) and spot weld spacing (Pitch).  $D = 7\text{mm}$ .**

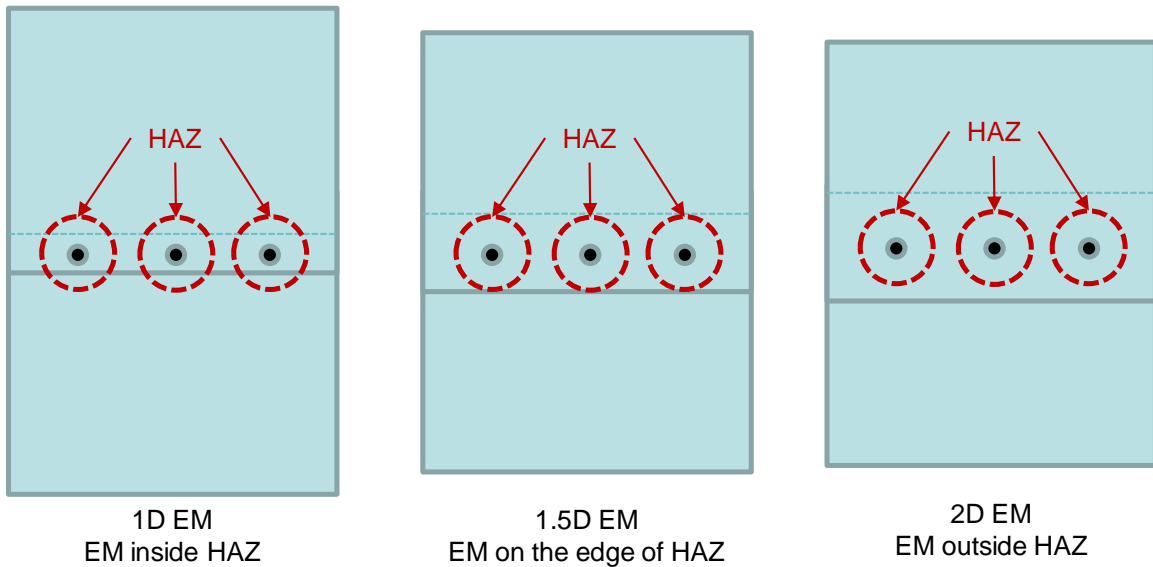


**Fig. 2.2: Heat affected zone (HAZ) and edge margin (EM).  $D = 7\text{mm}$ .**

Nine DoE runs produced nine nine-spot-weld panels, whereas the pitch and the edge margin were systematically varied. The DoE response variable was the ultimate lap-shear load of RFSSW. The pitch factor was varied between 2D, 3D, and 4D, whereas  $D$  is 7mm that is the spot

weld diameter. The edge margin factor was varied between 1D, 1.5D, and 2D. These design factor variations were based on the HAZ size of RFSSW.

The 1D pitch causes HAZs of adjacent spot welds to overlap as the diameter of HAZ is about 3D. The 2D pitch causes HAZs of adjacent spot welds to barely touch each other. The 4D pitch causes no HAZ overlaps. The spot weld HAZs and the spot spacings are illustrated in Fig. 2.1.

Likewise, the 1D edge margin puts the workpiece edge inside HAZ. The 1.5D edge margin puts the workpiece edge on the edge of HAZ. The 2D edge margin puts the workpiece edge outside HAZ. The spot weld HAZs and the edge margins are illustrated in Fig. 2.2.

Each panel pair is welded in a lap joint configuration as shown in Fig. 2.3. No industrial specification was used for the panel configuration. Each welded panel contains nine spot welds. The nine spot welds were numbered from left to right. The 1-9-5-3-7-2-8-4-6 welding sequence was used for producing every welded panel. All welded panels were naturally aged for at least two weeks. After natural aging, from each welded panel, Spot Weld 3, Spot Weld 4, and Spot Weld 5 were extracted as three separate single-spot coupons for unguided lap-shear static pull testing. The pull rate for unguided lap-shear static pull testing was 1.27 mm/min.

In addition to single-spot coupons, Spot Weld 6 and Spot Weld 7 were extracted as a two-spot specimen for cross-sectional microhardness measurements. The overall cut plan is depicted in the second image of Fig. 2.3. The cross-section specimens were etched with Keller's reagent. The cross-section specimen and microhardness measurement lines are indicated in Fig. 2.4. The microhardness values were taken from the midplane lines of the top sheet and the bottom sheet of the cross-section specimen, whereas a diamond indenter with a 0.5kg load was used for making 2 indents per mm along the measurement lines.

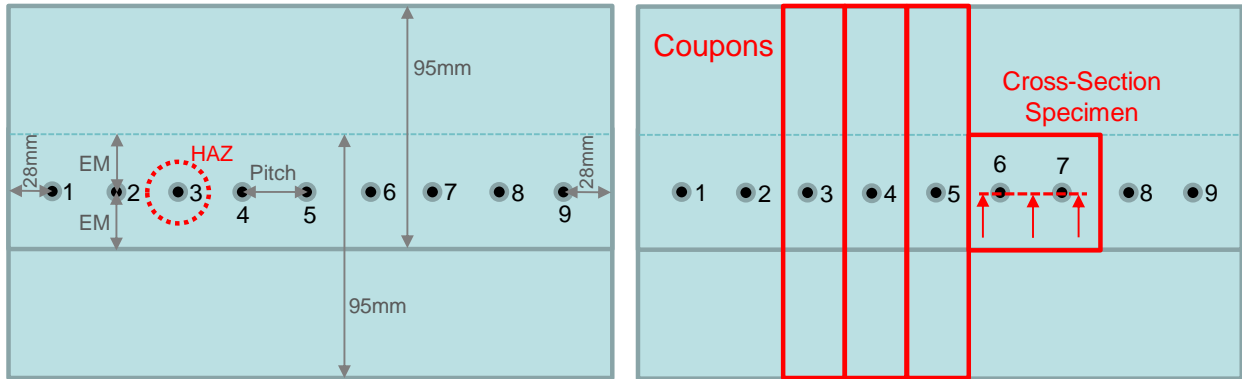


**Fig. 2.3: Nine-spot-weld panel configuration (left) and cut plan (right). Refill spot welds of each welded panel are numbered from left to right. Notes: Edge Margin = EM; Spot Weld Spacing = Pitch; HAZ = Heat Affected Zone.**

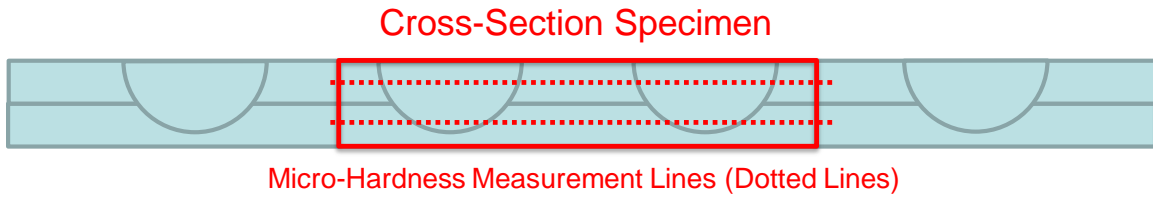


**Fig. 2.4: Cross-section specimen and microhardness measurement lines. The microhardness lines are midplane lines of the top sheet and the bottom sheet.**

## RESULTS AND DISCUSSION

The DoE runs produced nine nine-spot-weld panels with different spot spacings and edge margins. Fig. 2.4 depicts a few examples of welded panels. All welded panels were naturally aged for at least two weeks. After natural aging, single-spot coupons and two-spot specimens were extracted from the welded panels in accordance with the cut plan depicted in Fig.2.3. After

extracting the samples, each DoE run had three single-spot coupons and one two-spot specimen. Lap-shear static pull tests were carried out on the single-spot coupons to identify their failure loads as the response of the DoE runs. Vickers microhardness tests were carried out on the two-spot specimens to identify their microhardness values.

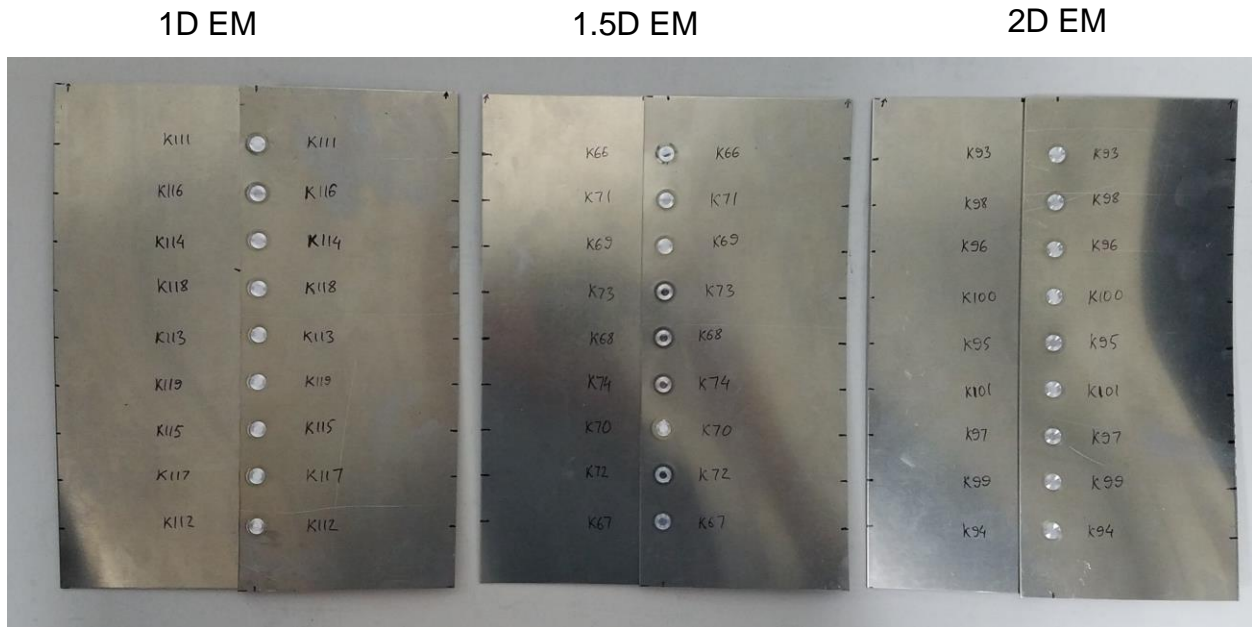


**Fig. 2.5: Examples of nine-spot-weld panels with different edge margins (EM). The spot weld spacing of the welded panels is 3D.  $D (=7\text{mm})$  is the spot weld diameter.**

During welding, the 1D edge margin caused edge swelling and a noticeable dent in the weld crown. Note that  $D (=7\text{mm})$  is the spot weld diameter. Fig. 2.6 displays edge swelling caused by the 1D edge margin (EM). None of the panels with 1.5D EM and 2D EM exhibited similar edge swelling during welding. Visual inspections indicate that the edge swelling gets worse if the workpiece edge gets inside the heat affected zone (HAZ) of RFSSW. Furthermore, an edge swelling lets the plasticized material drift away from the process zone and causes a noticeable dent in the weld crown as depicted in Fig. 2.7. The panels with 1D EM exhibit a 0.6mm-deep dent in

the weld crown. However, the panels with 1.5D EM and 2D EM demonstrate a 0.2mm-deep dent in the weld crown, which is a typical dent produced by RFSSW during this experimentation.

During the unguided lap-shear static pull testing, a single-spot coupon deformed due to asymmetric pull loads applied to it as illustrated in Fig. 2.8. The pull rate was 1.27 mm/min. The failure loads, which are the response of the DoE runs, were measured in the pull load direction. The deformation and the asymmetric pull loads imposed a minor tension load and a major shear load on the joint. These loads contribute to the formation of different mechanical failures.

Researchers [20, 21, 22, 23] explain possible causes of mechanical failures of friction stir spot joints under extreme external loads. A combination of stress concentrations, material properties, and the load-bearing regions of the joint determine the crack propagation in a friction stir spot joint [20]. Chen *et al* [21] carried out FSSW on aluminum alloys and found out that the tool pin penetration depth has a significant effect on the failure mode of friction stir spot welds. Su *et al* [22] observed that the energy input during the welding process influences the failure mode of friction stir spot welds under extreme external loads. In this study, mechanical failures demonstrated by refill spot joints under lap-shear loading are as follows.

- Nugget pullout (NP) is a failure that makes the weld nugget pulled out of the parent metal [23]. An NP failure usually occurs around the weld nugget within TMAZ/HAZ, where the metal grains are coarser. Metal regions with coarser grains demonstrate weaker mechanical strengths.
- The top sheet breakdown (TSB) failure occurs within the top sheet of the assembly [23]. TSB also originates in TMAZ/HAZ and propagates into the parent metal if the weld nugget is stronger than the parent metal.

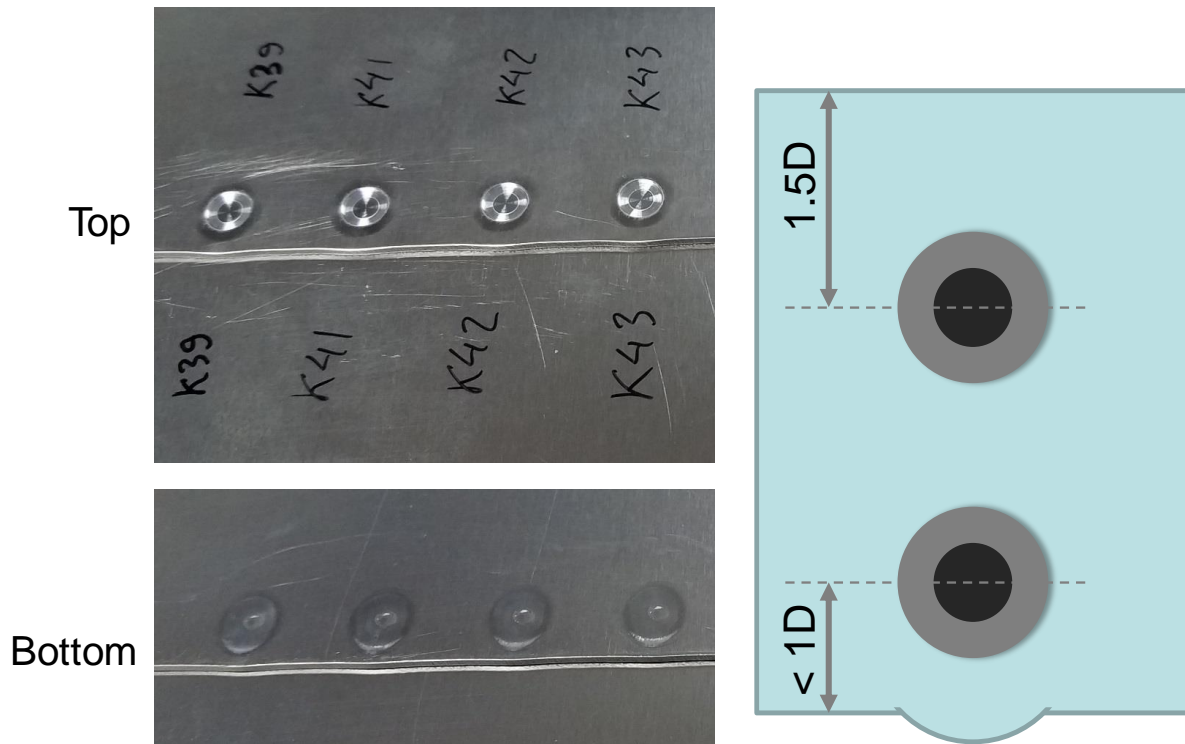


**Fig. 2.6:** Edge swelling caused by 1D edge margin (EM) during RFSSW. 1.5D EM and 2D EM did not cause any edge swelling.  $D (=7\text{mm})$  is the spot weld diameter.

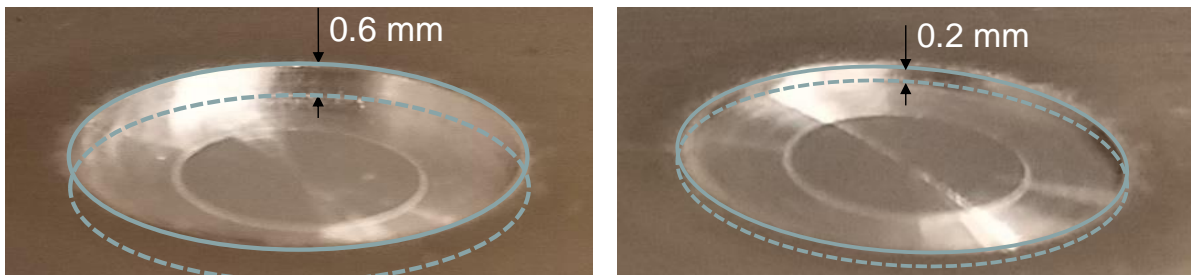


**Fig. 2.7:** Surface dent of 1D edge margin (left) and surface dent of 2D edge margin (right) panels.  $D (=7\text{mm})$  is the spot weld diameter.

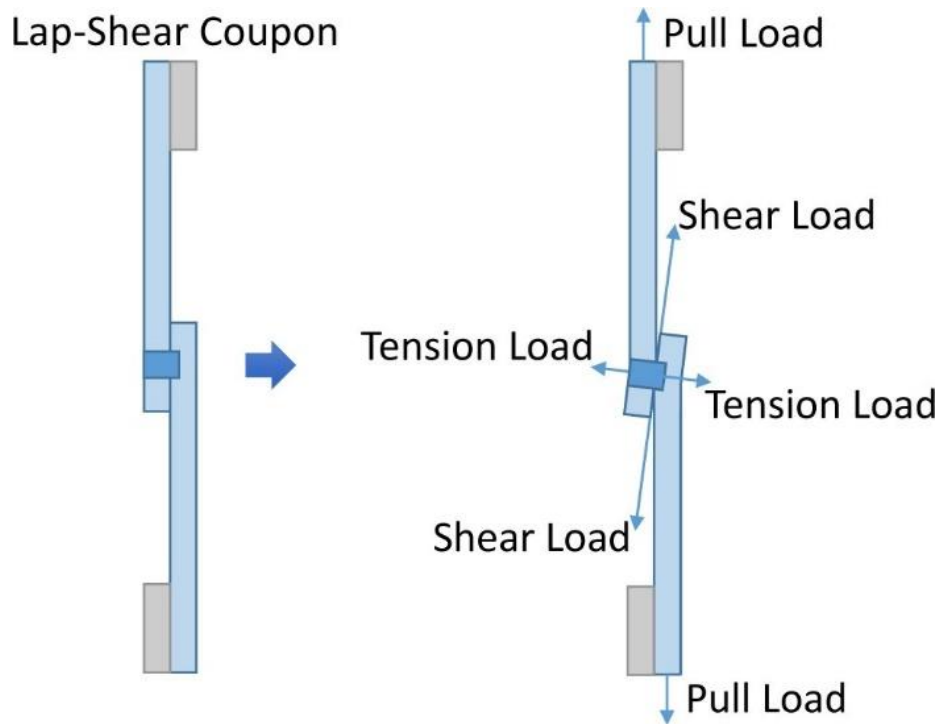


**Fig. 2.8: Side view of unguided lap-shear static pull testing of single-spot coupon. The coupon deforms due to asymmetric pull loads.**

Fig. 2.9 displays the DoE main effects plot and Fig. 2.10 depicts the DoE response surface for the failure load. Each DoE run had 3 repetitions. All static-test coupons, except coupons of DoE Run 2 and DoE Run 3, demonstrated nugget pullouts during mechanical tests as shown in Fig. 2.11. The coupons of DoE Run 2 and DoE Run 3 demonstrated TSB failures during mechanical tests as shown in Fig. 2.12. The failure loads of the DoE coupons were used for estimating a second order response surface. A response surface analysis [24] was performed with the use of the Statgraphic<sup>®</sup> software. The statistics of the response surface analysis are as follows.

- R-squared = 94.5595 %
- Standard Error of Estimation = 244.139 N
- Mean absolute error = 169.568 N

- p-value = 0.002

The R-squared statistic of 94.5595 % indicates that the response surface as fitted explains 94.5595% of the variability in the failure load. The standard error of the estimate shows the standard deviation of the residuals to be 244.139 N. The mean absolute error (MAE) of 169.568 N is the average value of the residuals. A p-value of 0.002 implies that the estimated response surface is statistically significant as it is less than 0.05.

The main effects plot in Fig. 2.9 suggests that the panels with larger spot spacings are stronger than the panels with smaller spot spacings. Also, smaller edge margins were associated with slightly higher failure loads. Note that the edge swelling issue was caused by the 1D edge margin (EM), but not 1.5D EM and 2D EM. It is assumed that a smaller spot weld spacing leads to a higher heat input applied to the workpiece during the welding process, but the higher heat input negatively affects the microstructural properties of the workpiece and weakens its mechanical strengths. This assumption is in a good agreement with the DoE results and can also be verified with cross-sectional microhardness maps.

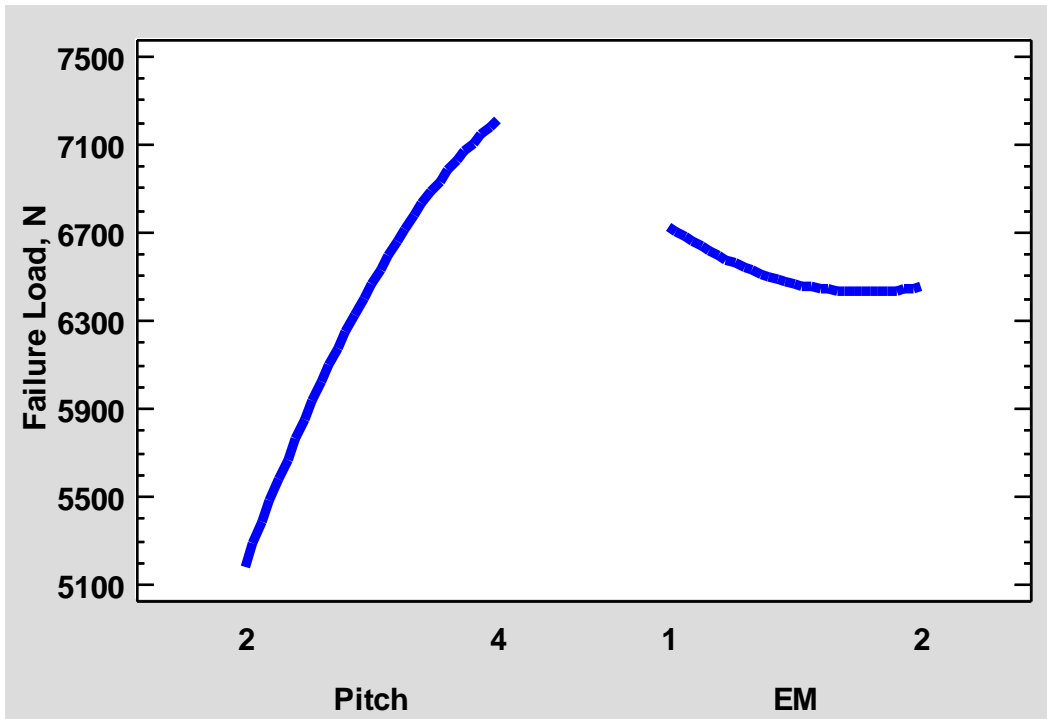


**Fig. 2.9: Main effects plot of pitch and edge margin (EM).  $D = 7\text{mm}$ .**

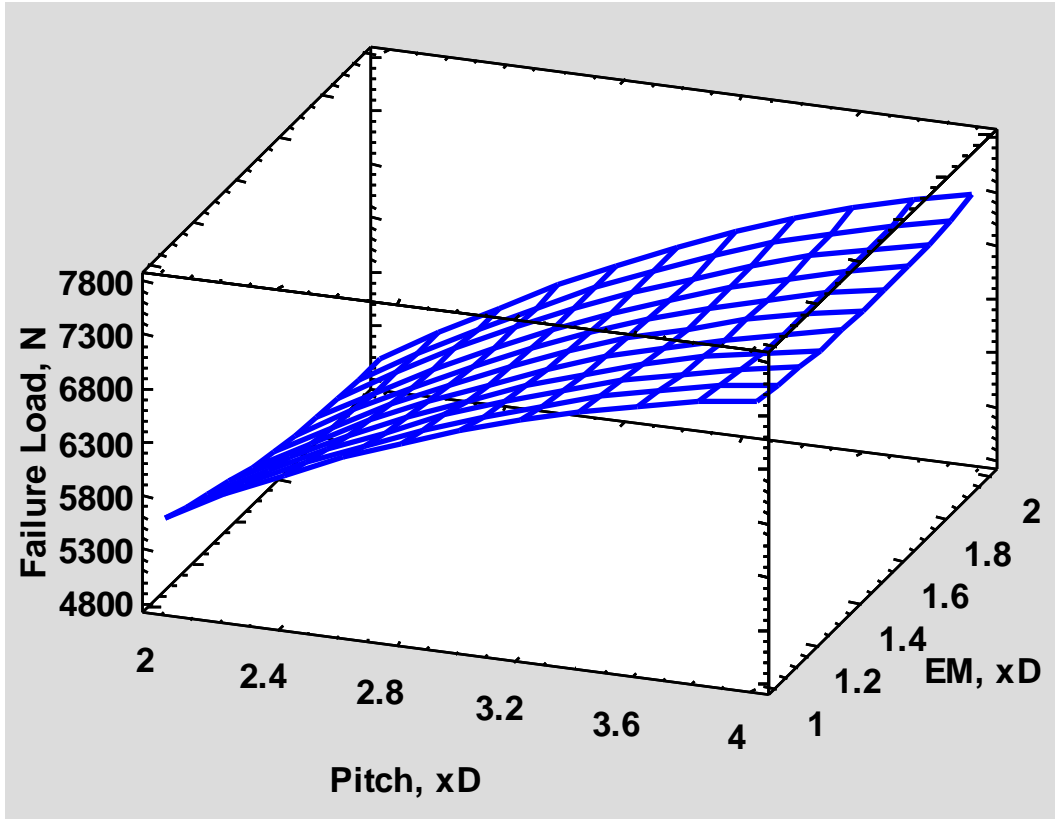


Fig. 2.10: Estimated response surface of pitch and edge margin (EM).  $D = 7\text{mm}$ .

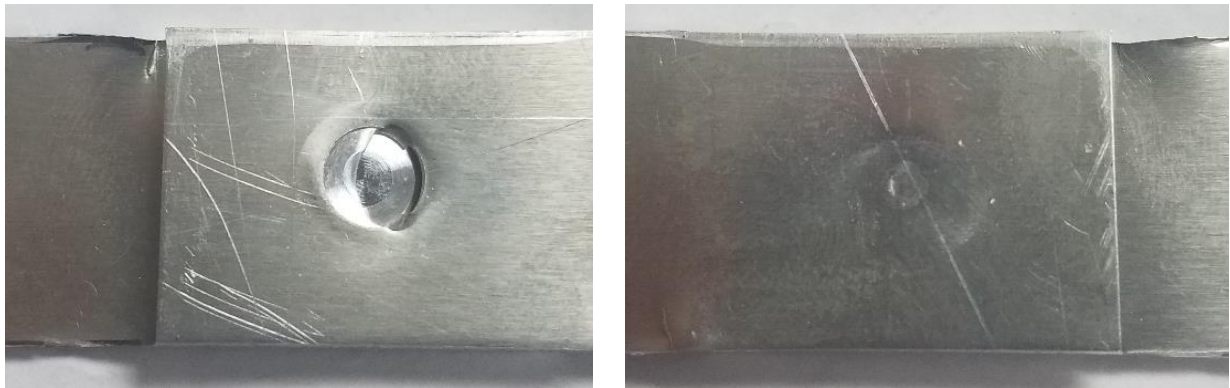
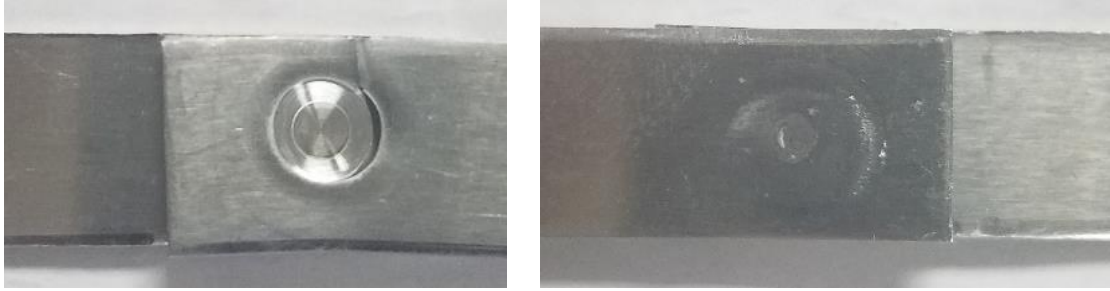
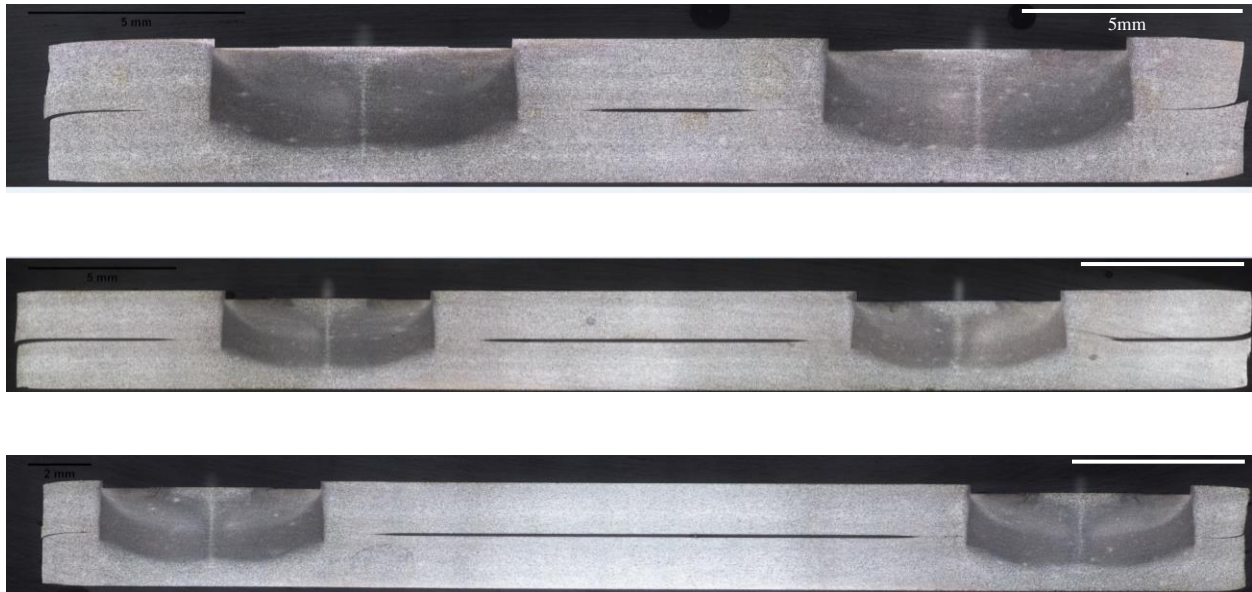


Fig. 2.11: Top view (left) and bottom view (right) of nugget pullout (NP) failure of 3D-Pitch 2D-EM coupon after static pull testing.  $D = 7\text{mm}$ ; EM = Edge Margin.



**Fig. 2.12: Top view (left) and bottom view (right) of top sheet breakdown (TSB) failure of 2D-Pitch 1.5D-EM coupon after static pull testing.  $D = 7\text{mm}$ ; EM = Edge Margin.**



**Fig. 2.13: Examples of two-spot cross-section specimens. 2D pitch (top), 3D pitch (middle), and 4D pitch (bottom).  $D = 7\text{mm}$ .**

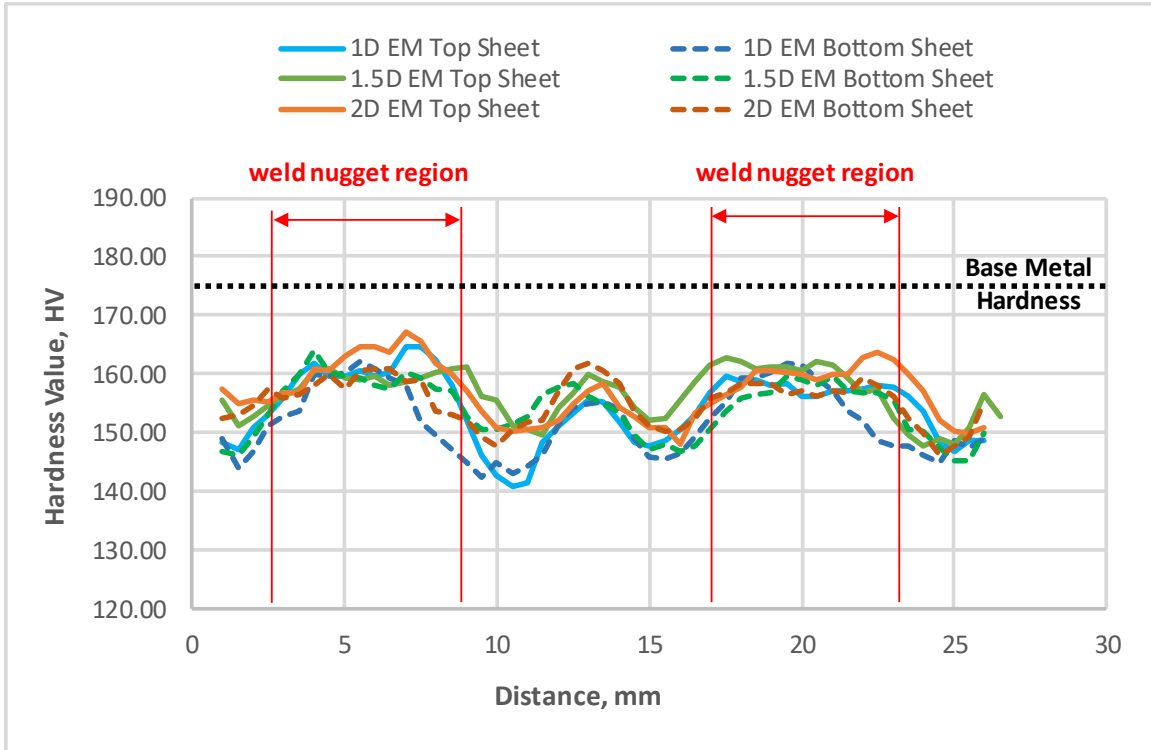


**Fig. 2.14: Microhardness values of 2D pitch cross-section specimens. D = 7mm; EM = Edge Margin.**

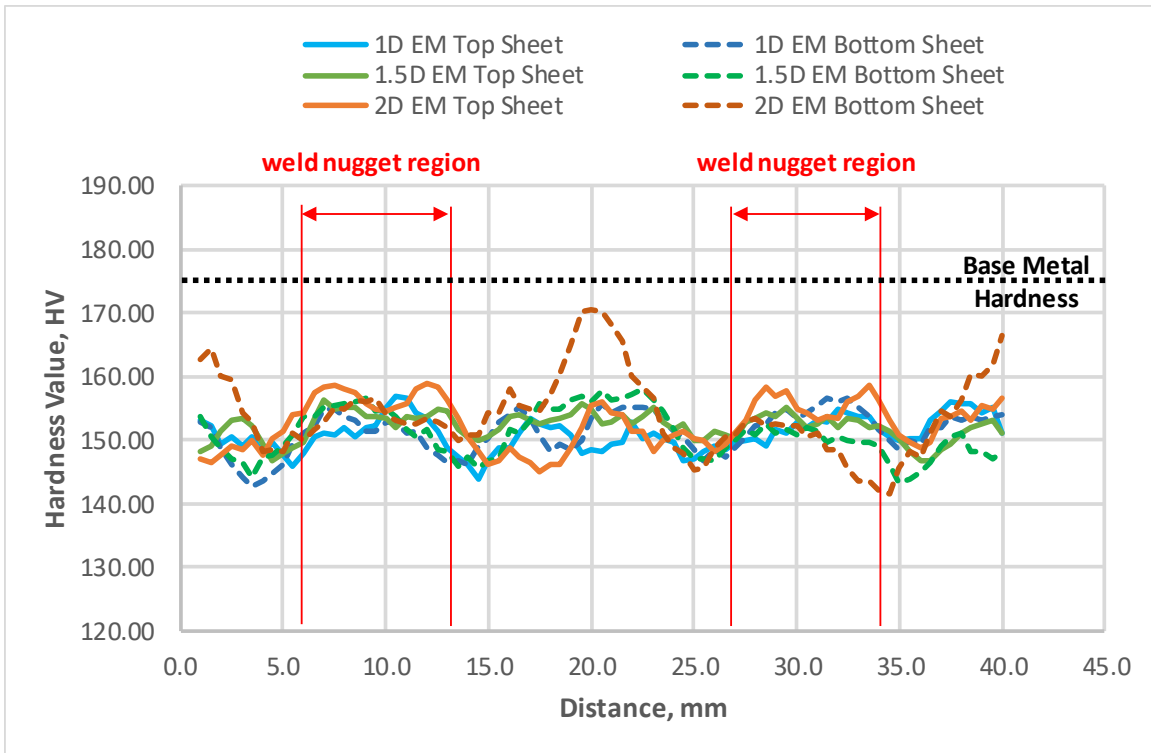


**Fig. 2.15: Microhardness values of 3D pitch cross-section specimens. D = 7mm; EM = Edge Margin.**

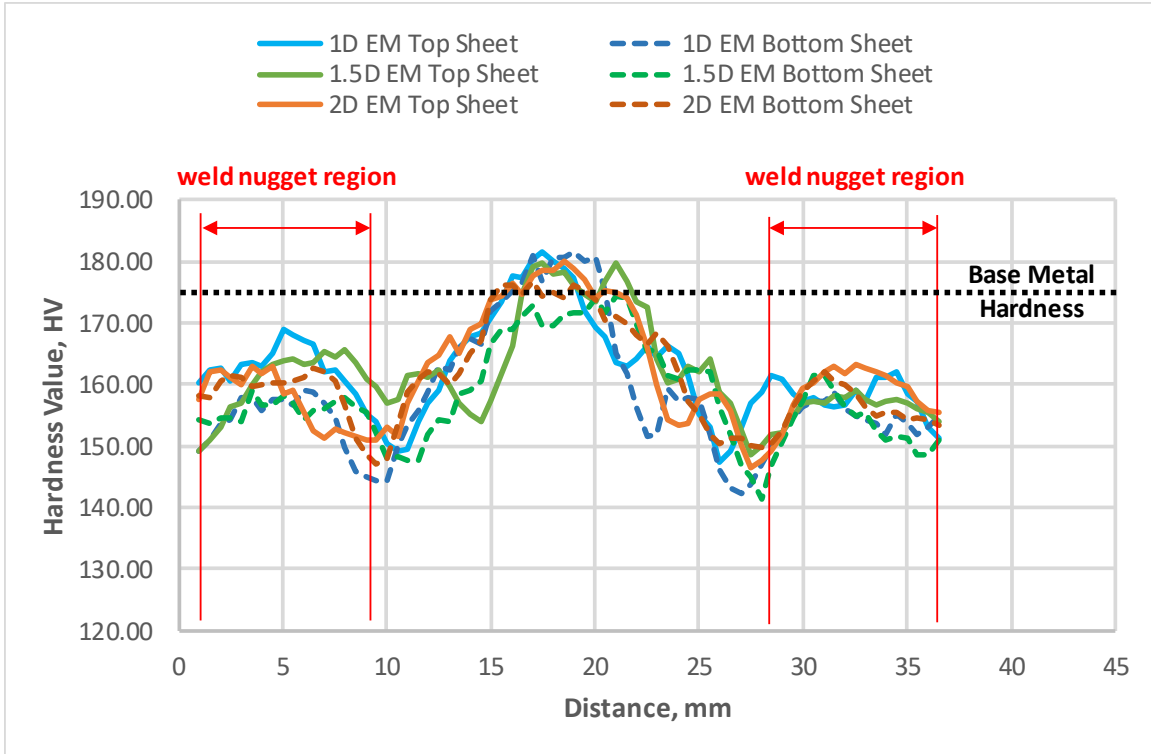


**Fig. 2.16: Microhardness values of 4D pitch cross-section specimens. D = 7mm; EM = Edge Margin.**

Fig. 2.13 exhibits a few images of two-spot cross-section specimens extracted from the DoE panels in accordance with the cut plan depicted in Fig. 2.3 and Fig. 2.6. The cross-section specimens were polished and then etched with Keller’s reagent. The hardness values of a cross-section specimen were identified through applying micro-indentations along the midplane lines of the top sheet and the bottom sheet with the use of a diamond indenter and a 0.5kg load. The spacing between two adjacent micro-indentations was 0.5 mm. Microhardness maps of the cross-section specimens are depicted in Fig. 2.14, Fig. 2.15, and Fig. 2.16. According to the microhardness maps, the hardness values of the 2D-pitch specimens and the-3D pitch specimens are between 145 HV and 165 HV, which are about 30 HV below the base metal hardness value. However, the bottom sheet hardness values of the 3D-pitch 2D-EM specimen in Fig. 2.15 get

closer to the base metal hardness value at the midpoint between the two spot welds. Also, the hardness values of the 4D-pitch specimens reached the base metal hardness value at the midpoint between the two spot welds. These results verify that the 4D pitch causes no HAZ overlap between two adjacent spot welds in the top sheet and the bottom sheet and also indicates that the 4D-pitch DoE panels tend to retain the base metal properties more than the 2D-pitch panels and the 3D-pitch panels do. The microhardness test results also support the DoE results of single-spot lap-shear coupons as higher hardness values translate into higher mechanical strengths.

The research findings suggest that the best possible design parameters to achieve the best possible refill-friction-stir-spot-welded structure can be the 4D pitch and the 1.5D edge margin based on the visual inspections, the DoE results, and the microhardness test results. In general, many factors like the material type, the material thickness, the joint configuration, the process parameters, and the way in which the assembly will be stressed play important roles in defining the design parameters. In riveted structures, a spacing between two rivet joints should be at least three times the rivet shaft diameter [24]. In contrast, there is no lower limit for the refill-spot-weld spacing as refill spot joints can be made right next to each other. However, a narrow spot weld spacing causes HAZ overlaps and may weaken the material strength. In addition, the edge margin should not be less than 1.5D as a narrow edge margin could bulge and deform during the RFSSW process.

## SUMMARY

The major goal of the research is to identify design requirements of RFSSW that would offer better mechanical properties of multi-refill-spot-weld structures. The design requirements encompass design parameters of the spot weld spacing (pitch) and the edge margin. An edge margin defines a center-to-edge distance between a spot weld and the material edge. A spot spacing or pitch defines a center-to-center distance between two adjacent spot joints in the same row.

RFSSW imposes three distinct weld zones on heat-treatable aluminum alloys, which are a Heat Affected Zone (HAZ), a Thermo-Mechanically Affected Zone (TMAZ), and a weld nugget. Under an extreme external load, a refill spot weld usually starts to fail in TMAZ / HAZ, where the metal grains are coarser. Therefore, the extent of HAZ / TMAZ of a refill spot weld is critical to defining a spot weld spacing and an edge margin for multi-spot-weld structures.

The research implemented a Design-of-Experiment (DoE) method in characterizing failure loads of multi-spot-weld panels with different spot spacings and edge margins. The arrangements of the spot spacings and the edge margins were based upon the HAZ size of RFSSW. The research employed mechanical tests of actual multi-spot-weld panels with different spot spacings and edge margins to study the effects of the design parameters on the mechanical properties of the multi-spot-weld panels.

According to the DoE results, the spot spacing had a strong positive effect on the lap-shear failure load of refill spot joints. Larger spot spacings with no HAZ overlaps produced stronger multi-spot-joint panels. The edge margin factor did not demonstrate a considerable effect on the failure load. However, narrow edge margins caused bulging issues during the welding process, which had to be considered. The refill spot welds exhibited two types of failures, which are nugget

pullouts and parent metal breakdowns (top sheet breakdowns). These failures usually originate in HAZ/TMAZ of refill spot joints under extreme external loads. Microhardness tests conducted later revealed microhardness patterns of refill spot joints, which helped identify whether HAZs of adjacent refill spot joints overlap with each other. The microhardness test results supported the fact that larger spot spacings with no HAZ overlaps produced stronger multi-spot-joint panels.

## **CHAPTER 3: COMPARISON OF REFILL FRICTION STIR SPOT WELDING VERSUS RIVETING IN AIRCRAFT APPLICATIONS**

### **OBJECTIVE**

The presented study aimed to evaluate the mechanical properties of refill spot welds and their failure mechanisms with the use of industrial test standards. The mechanical properties of refill spot welds were compared with those of rivet joints with comparable joint sizes. All refill spot welds were produced by a robotic RFSSW system developed by Kawasaki Heavy Industries (KHI). The failure mechanisms of refill spot welds were characterized in terms of external loading, parent metal properties, and weld properties. Preliminary test results of this study were documented in academic theses [26, 27]. This paper presents thorough experimental results and failure analysis of refill spot welds

### **MATERIALS AND METHODS**

Industrial standards that are typically used for testing rivet joints were implemented in this study to evaluate the mechanical properties of refill spot welds. Therefore, the presented study involved a comparison between the mechanical properties of refill spot welds and the mechanical properties of rivet joints. With that being said, the experiments used an RFSSW tool and a solid rivet of comparable sizes for producing refill spot weld coupons and rivet coupons. The RFSSW weld tool consists of a retractable probe with a diameter of 4 mm and a shoulder with a diameter of 7 mm. In contrast, there is a solid rivet of MS20426-AD5 that has a shaft with a diameter of 3.9 mm (5/32 inches) and a 100-degree countersunk flush head with a diameter of 7.1 mm (9/32 inches).

The workpieces consist of bare 1.27-mm-thick (0.050 inch) AA7075-T6 and bare 1.6-mm-thick (0.063 inch) AA2024-T3. They are high-strength aluminum alloys mostly used for making

metallic structures of aircraft. AA7075-T6 is a baseline aerospace aluminum alloy mostly used for making stiffeners, and AA2024-T3 is another baseline aerospace aluminum alloy mostly used for making aircraft skins [28]. The MS20426-AD5 rivet is made of AA2117-T4, which is malleable and ductile. The properties of AA7075-T6, AA2021-T3, and AA2117-T4 can be obtained from online sources [29].

The workpieces were refill-friction-stir-spot-welded from the stiffener side, which is AA7075-T6. The refill spot weld configuration is shown in Figure 3.1a. Refill spot welds were made by the robotic RFSSW system developed by Kawasaki Heavy Industries. The shoulder-plunging method was employed in the RFSSW process. The robotic system was preprogrammed for making multiple welds in the coupon pieces. The RFSSW process parameters are as follows: The plunge depth of the welding process was 1.57 mm, which is slightly greater than the stiffener thickness 1.27 mm. The tool spindle speed was 1400 rpm. The probe speed was 12 mm/s. The process force was 13 kN. These process parameters were obtained from a design-of-experiments (DoE) study documented by Boldsaikhan et al. [30]. The same process parameters were used for producing every refill spot weld in this study.

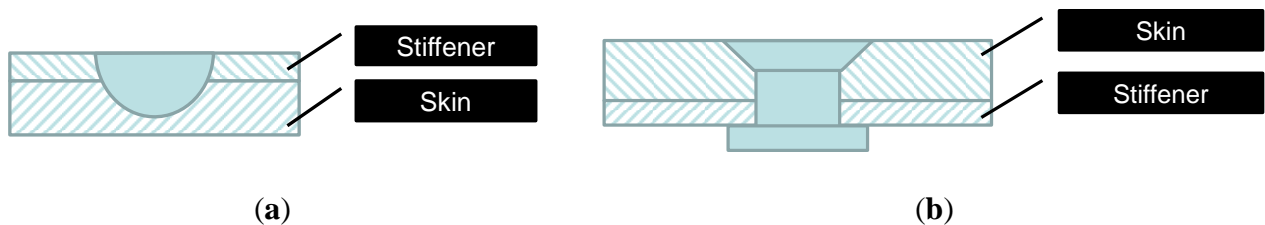


**Figure 3.1 Lap joint configurations: (a) refill spot weld configuration and (b) rivet joint configuration.**

In contrast, riveting was done from the skin side, which is AA2024-T3, as shown in Figure 3.1b. A #21 drill bit was used for drilling holes. Drilling was performed by a KUKA robot with a payload capacity of 60 kg. The spindle speed for drilling was 6000 rpm. Rivets were installed in

the drilled holes by a trained technician. A go-no-go gauge was used to make sure whether the rivet had been clenched properly.

As mentioned earlier, AA7075-T6 is a baseline stiffener metal and AA2024-T3 is a baseline skin metal used in aircraft structures [28]. Although RFSSW does not leave behind an exit hole in the workpieces, it may leave behind a thin indentation of up to 0.2 mm on the workpiece surface as a weld tool footprint. Such surface indentations may cause not only air turbulence but also aesthetic issues if they are exposed to the exterior of the aircraft skin. Therefore, RFSSW is usually done from the stiffener side, as shown in Figure 3.1a, so that the exterior skin surface remains flush and smooth.

In contrast, riveting should be done in a way that the flush head of the rivet is on the skin side, as shown in Figure 3.1b, so that there is no protruding clenched end exposed to the exterior of the aircraft skin, as such protruding ends may cause not only air turbulence but also aesthetic issues.

The coupon configurations and testing methods, for both RFSSW and riveting, were implemented in accordance with the following industrial standards and specifications:

- The NASM-1312-4 method applies to sheet metal lap joints fastened with rivets, bolts, screws, or comparable fastening methods [--]. It outlines a standard procedure for determining the room-temperature strength properties of mechanically fastened sheet metal lap joints statically loaded to produce shear on the joint. The significant strength properties include the ultimate strength and yield strength of the joint. No guide fixture is required. The NASM 1312-4 coupon configurations for RFSSW and riveting are depicted in Figure 3.2.
- The ISO-14272 method outlines a standard procedure for testing the tension joint ultimate strength of lap joints at room temperature [31]. The standard specifies the

specimen dimensions and a testing procedure for the spot and projection welds in overlapping sheets. In any metallic material of thickness 0.5 mm to 3 mm, the welds have a maximum diameter of  $7\sqrt{t}$ , where  $t$  is the thickness of the metallic sheet. A specific guide fixture is required for cross-tension testing. The ISO 14272 coupon configurations for RFSSW and riveting are depicted in Figure 3.3.

- The NASM-1312-21 method covers the procedure and apparatus required for testing the shear joint fatigue of fasteners at room temperature [32]. In this study, the fatigue load levels were 75%, 50%, and 25% of the ultimate shear load. Three RFSSW coupons and three rivet coupons were tested for each load level. The ratio between the minimum and maximum loads in each loading cycle was 0.1. The loading cycle frequency was 30 Hz. A specific guide fixture was used for keeping the coupon pieces straight during the fatigue test. The NASM 1312-21 coupon configurations for RFSSW and riveting are depicted in Figure 3.4.

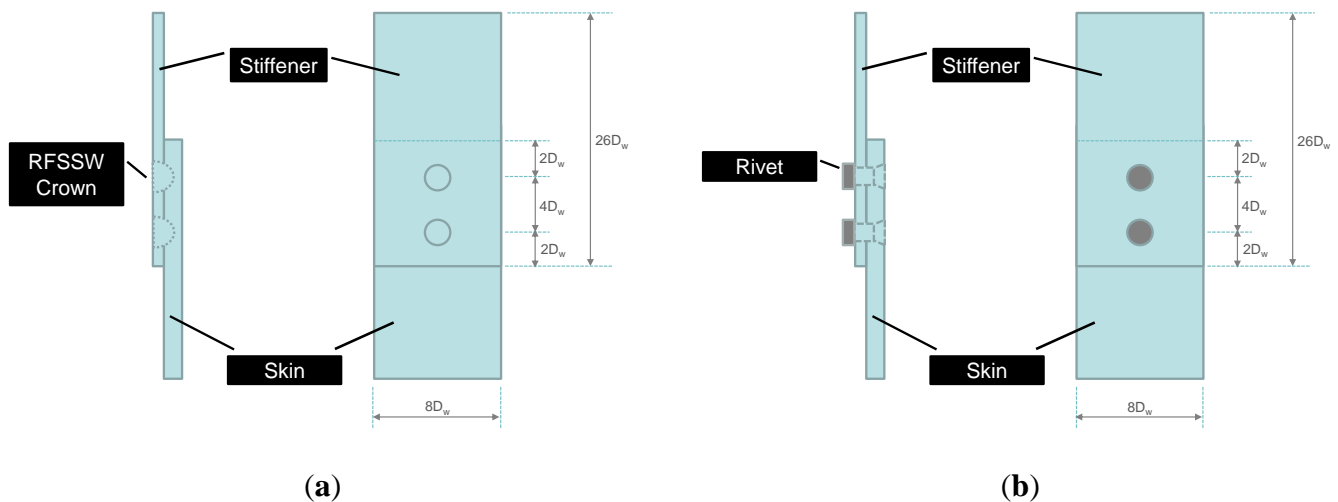


**Figure 3.2. Two-spot coupon configurations in accordance with NASM-1312-4: (a) 2-refill-spot-weld coupon configuration and (b) 2-rivet-joint coupon configuration.  $D_w$  is the refill spot weld diameter, which is 7 mm.**

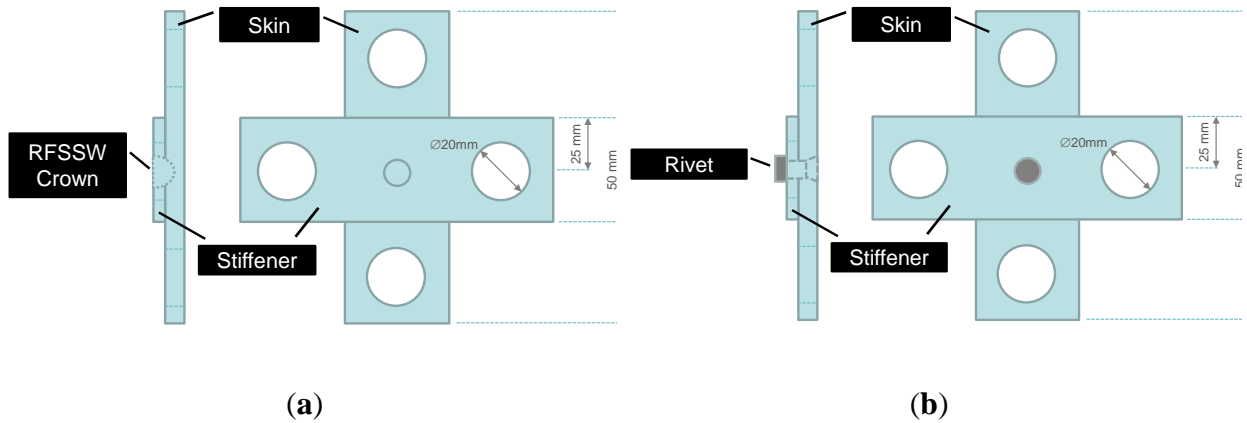


**Figure 3.3. Cross-coupon configurations in accordance with ISO-14272: (a) RFSSW cross-coupon configuration and (b) rivet cross-coupon configuration.**

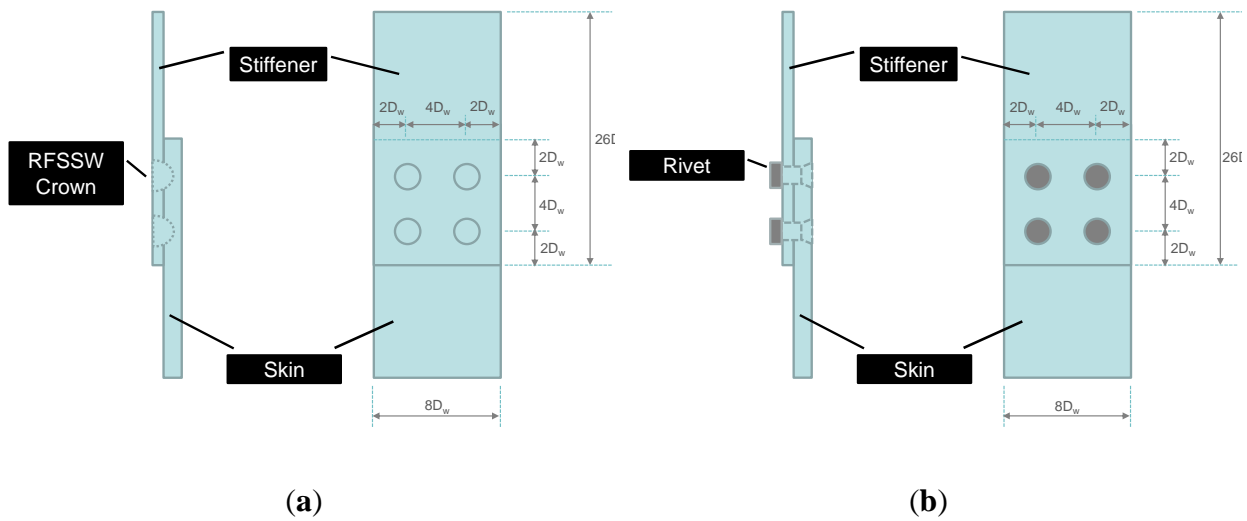


**Figure 3.4. Four-spot coupon configurations in accordance with NASM-1312-21: (a) 4-refill-spot-weld coupon configuration and (b) 4-rivet-joint coupon configuration.  $D_w$  is the refill spot weld diameter, which is 7 mm.**

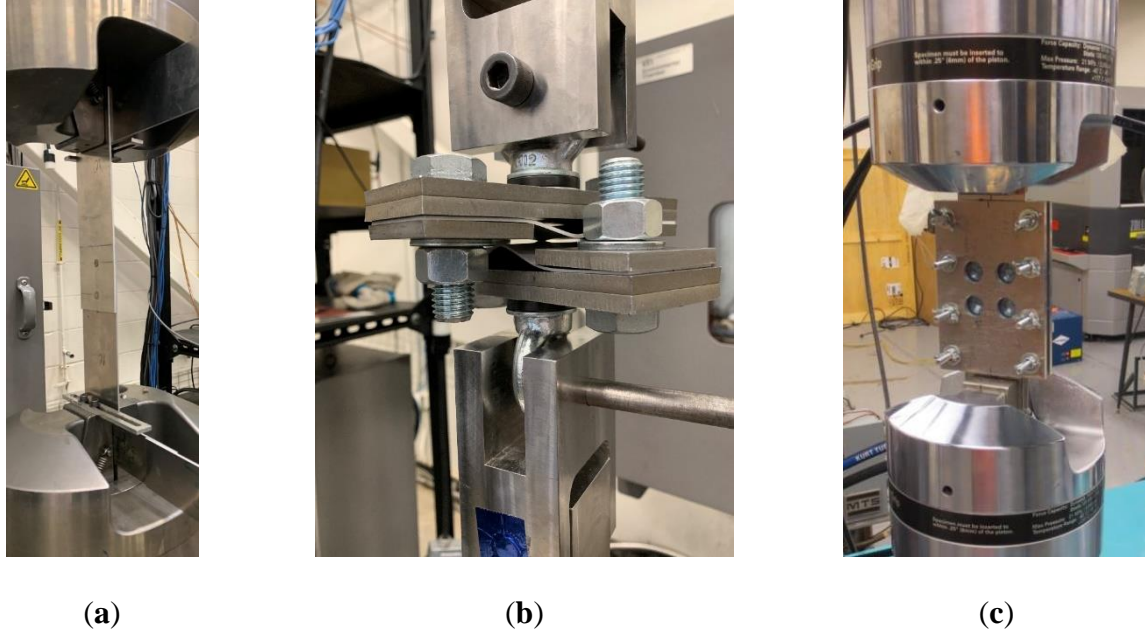


**Figure 3.5. Mechanical test setups: (a) NASM-1312-4 test setup, (b) ISO-14272 test setup, and (c) NASM-1312-21 test setup.**

The mechanical test setups for NASM-1312-4, ISO-14272, and NASM-1312-21 are depicted in Figure 3.5a, Figure 3.5b, and Figure 3.5c, respectively. These industrial test standards were used according to the Metallic Materials Properties Development and Standardization (MMPDS) Handbook [28], which contains design information on the mechanical and physical properties of metallic materials and joints commonly used in aircraft and aerospace vehicle structures. The MMPDS Handbook has been reviewed and approved using a standardized process that involves certifying agencies, including major government organizations, material suppliers, and material users worldwide [28].

## **RESULTS**

No specific standard is available for mechanically testing refill spot welds thus far. Therefore, to test refill spot welds, this study used conventional test standards that are typically used to test rivet joints. The presented study involved a comparison between the mechanical properties of refill

spot welds and the mechanical properties of rivet joints. By considering this insight, the experiments used an RFSSW tool and a solid rivet of comparable sizes for producing refill spot weld coupons and rivet coupons in accordance with NASM-1312-4 [52], ISO-14272 [31], and NASM-1312-21 [32]. Table 3.1 presents the coupon quantities.

**Table 3.1. Coupon quantities.**

<b>Mechanical Tests</b>	<b># of RFSSW Coupons</b>	<b># of Rivet Coupons</b>
NASM-1312-4 static load lap shear test	10	10
ISO-14272 static load cross-tension test	10	10
NASM-1312-21 fatigue lap shear pull test	9 *	9 *

\* 3 coupons for each fatigue load level.

**Table 3.3 (continued)**

There is a daunting challenge in drawing a viable comparison between RFSSW and riveting as they are two completely different joining methods in terms of their joint configurations, their joint compositions, and their joining processes. A refill spot weld is purely made from the base/parent metals without consuming any filler or foreign materials. In contrast, riveted joints consume solid rivets that are made of malleable, ductile metals for fastening. Riveting requires labor-intensive installation steps that require at least 8-10 s to be completed by a trained technician.

In contrast, RFSSW takes about 2 s, from tool touch-down to tool removal, to be made by an RFSSW system. Refill spot welds exhibit a near-flush surface finish on the workpiece surfaces. In contrast, the solid rivets may exhibit a protruding rivet end that makes the surface uneven and aesthetically unpleasant. In addition, a refill spot weld does not have a head and a clenched end to mechanically grip the workpieces together like solid rivets do. So, the strength of a refill spot weld purely depends on the strengths of the weld zones thermomechanically created in the workpieces.

After producing refill spot weld coupons and rivet coupons, the coupons were mechanically tested in accordance with their associated test standards. The NASM 1312-4 static load lap shear test results are provided in Figures 3.6a and 3.7. The ISO-14272 static load cross-tension test results are provided in Figures 3.6b and 3.8. The NASM-1312-21 fatigue lap shear pull test results are presented in Figures 3.9 and 3.10.

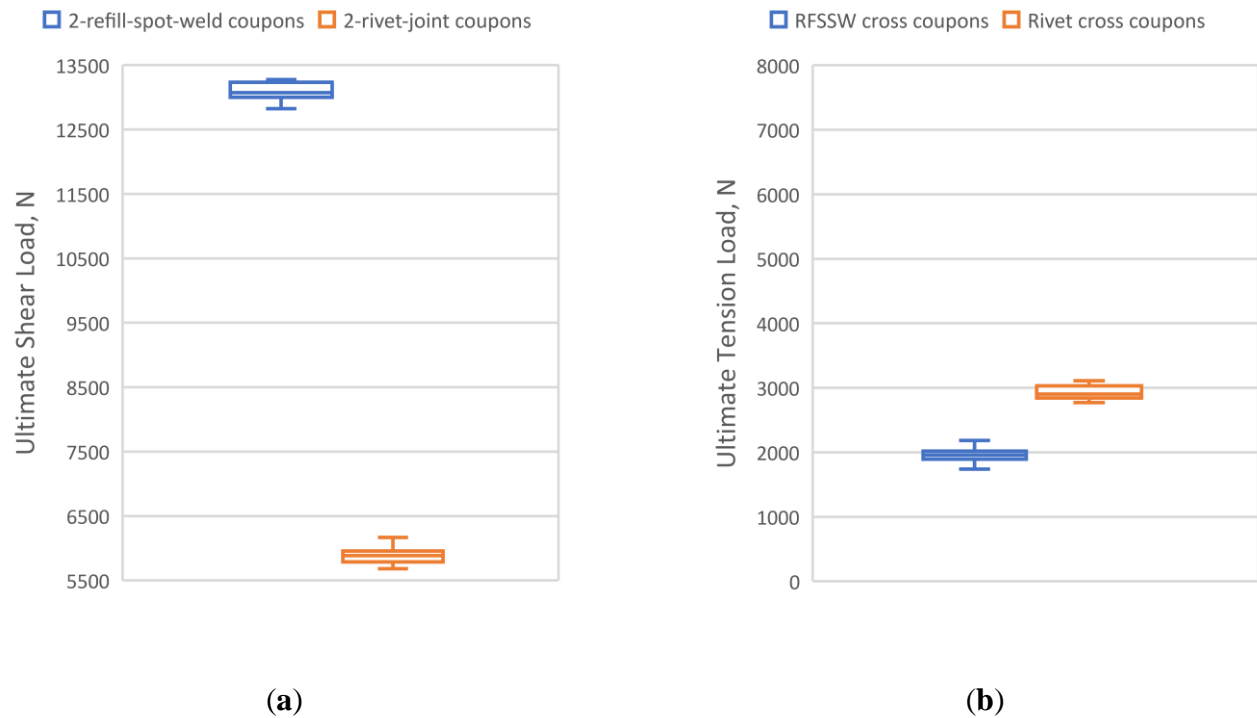


**Figure 3.6. Box-whisker plots of static load test results: (a) ultimate shear loads of 2-spot coupons and (b) ultimate tension loads of cross coupons. The 2-spot coupons were tested in accordance with NASM-1312-4, and the cross coupons were tested in accordance with ISO-14272.**

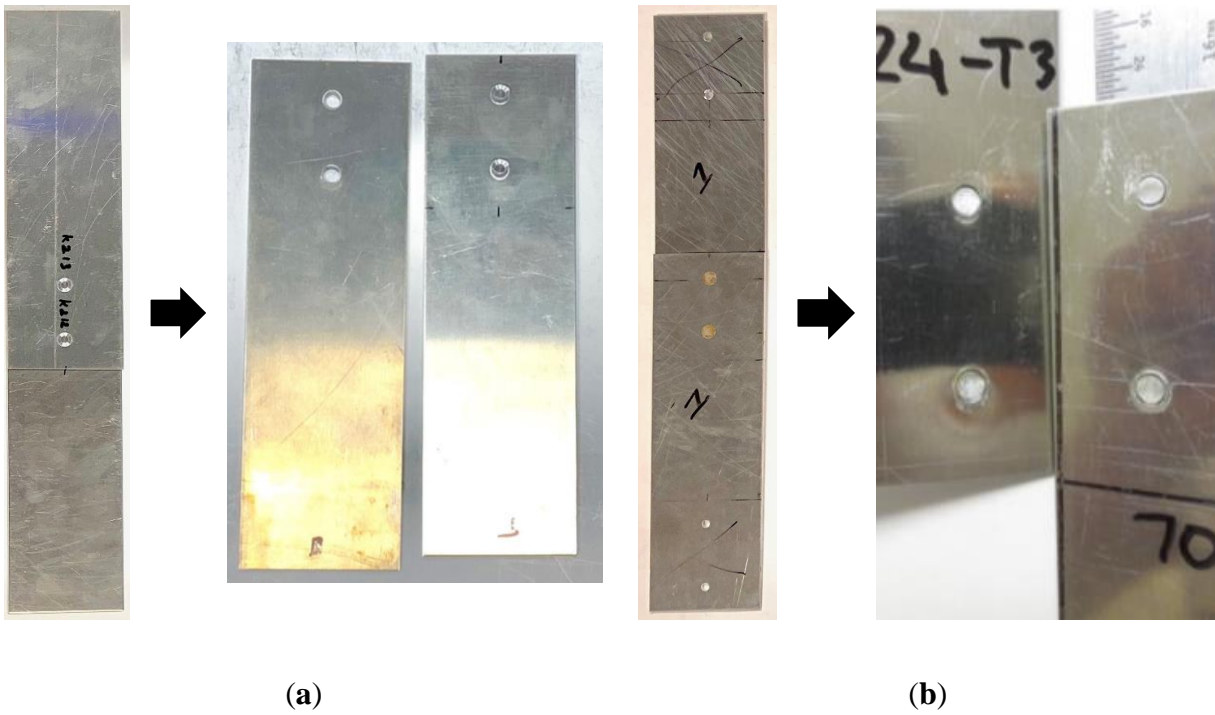


**Figure 3.7. Two-spot coupons before and after static load lap shear tests: (a) 2-refill-spot-weld coupon (left) and nugget pullout failures (right); (b) 2-rivet-joint coupon (left) and rivet shear failures (right). The image of the nugget pullout failures shows the faying surfaces of the stiffener and skin pieces. The image of the rivet shear failures also shows the faying surfaces of the skin and stiffener pieces. The images may have different scaling for clarity.**

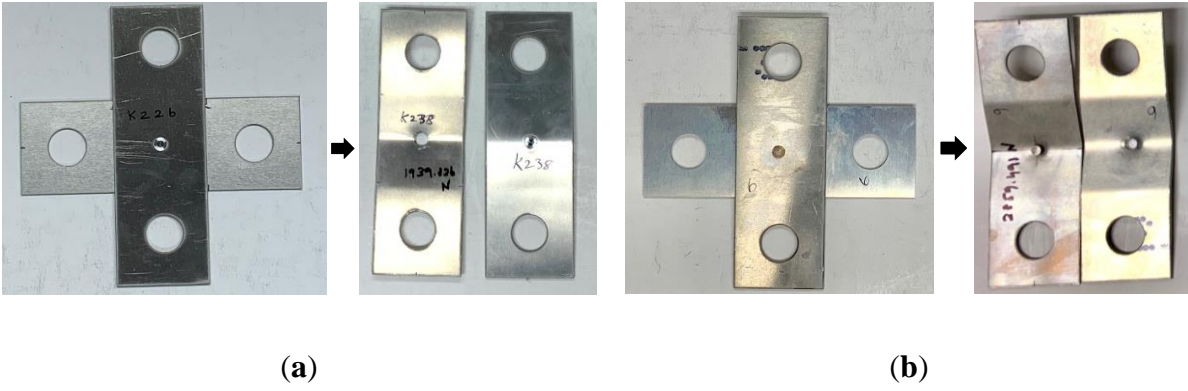


**Figure 3.8. Cross coupons before and after static cross-tension load tests: (a) RFSSW cross coupon (left) and nugget pullout failure (right); (b) rivet cross coupon (left) and rivet pullout failure (right). The image of the nugget pullout failure shows the external surface of the stiffener piece and the faying surface of the skin piece. The image of the rivet pullout failure shows the external surface of the skin piece and the external surface of the stiffener pieces.**

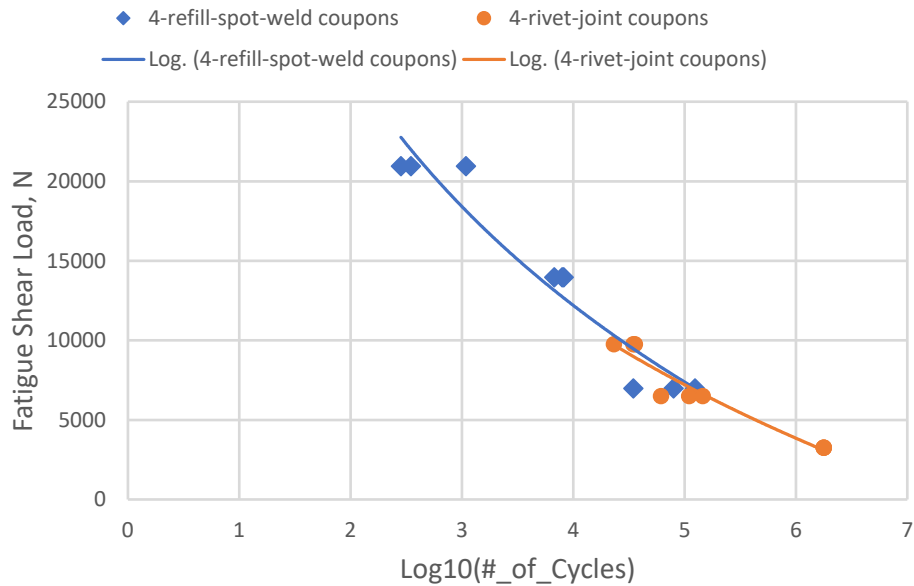


**Figure 3.9. Fatigue test results: fatigue tests were carried out in accordance with NASM-1312-21.**

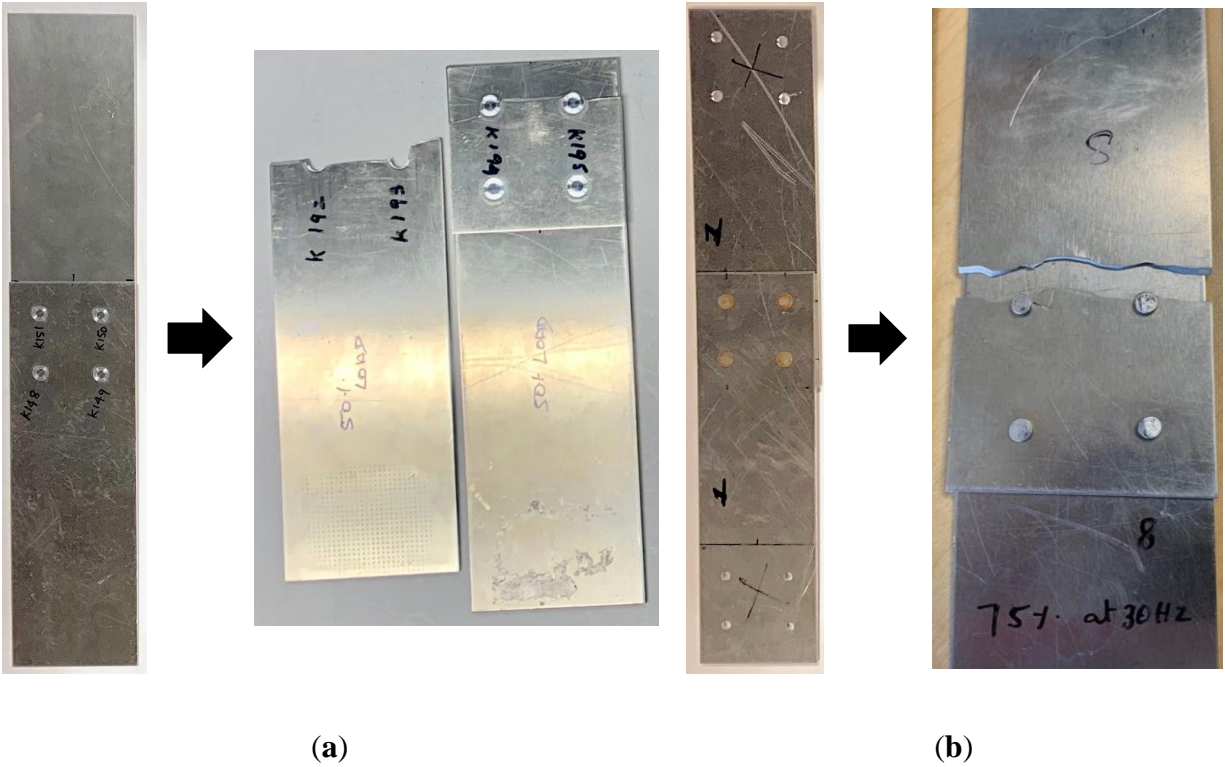


**Figure 3.10. Four-spot coupons before and after fatigue lap shear pull tests: (a) 4-refill-spot-weld coupon (left) and tensile failure of stiffener piece (right); (b) 4-rivet-joint coupon (left) and tensile failure of stiffener piece (right). The images may have different scaling for clarity.**

Overall, the RFSSW coupons demonstrated significantly higher ultimate lap shear strengths but slightly lower ultimate cross-tension strengths than those of the rivet coupons, as suggested by Figure 3.6. As suggested earlier, a refill spot weld is made of the workpiece metals via thermomechanical processing, but a rivet joint is made by fastening a solid rivet. The workpieces used in this study are high-strength aerospace aluminum alloys that have much higher strengths than the solid rivet metal. Therefore, having a refill spot weld that has stronger lap shear strength than that of a comparable rivet joint is intuitive. However, a refill spot weld does not have a head and a clenched end to mechanically grip the workpieces together like solid rivets do, which perhaps

explains why the ultimate tension loads of refill spot welds were slightly lower than the ultimate tension loads of rivet joints.

The fatigue test results in Figures 3.9 and 3.10 indicate that both RFSSW coupons and rivet coupons demonstrated comparable performances during low-load-level fatigue lap shear tests. However, RFSSW coupons outperformed rivet coupons during high-load-level fatigue lap shear tests as the 75% and 50% load levels of the 4-refill-spot-weld coupons were higher than the ultimate loads of the 4-rivet-joint coupons. The 75%, 50%, and 25% load levels for RFSSW coupons were 20,952.9 N, 13,968.6 N, and 6984.3 N, respectively. The 75%, 50%, and 25% load levels for rivet coupons were 9770.9 N, 6514.0 N, and 3257.0 N, respectively. These load levels were based on the average ultimate shear load of 4-refill-spot-weld coupons and the average ultimate shear load of 4-rivet-joint coupons, which were 27,937.2 N and 13,027.9 N, respectively.

RFSSW coupons exclusively exhibited nugget pullout failures during static lap shear load tests and static cross-tension load tests, as shown in Figures 3.7a and 3.8a. Riveted coupons exhibited rivet shear failures during static lap shear load tests, as shown Figure 3.7b, and rivet pullout failures during static cross-tension load tests, as shown in Figure 3.8b. All RFSSW coupons and rivet coupons demonstrated tensile failures in their stiffener pieces during the fatigue lap shear tests.

As a refill spot weld is an integral part of the workpieces, the refill spot weld strength purely depends on the strengths of the weld zones created by the welding process. Hovanski et al. [33] studied the effects of the RFSSW process cycle time on the refill spot weld lap shear strength. The next section will discuss failure mechanisms demonstrated by refill spot welds.

## DISCUSSION

RFSSW produces different weld regions with different microstructures and mechanical properties. The heat-affected zone (HAZ) is a region that spans around the weld as its outermost shell in the heat-treatable base metal. It is affected by the process heat but not the mechanical stirring. Metal grain growth may occur in the HAZ of heat-treatable aluminum alloys due the process heat. The thermomechanically affected zone (TMAZ) is an interlayer shell between the HAZ and the weld nugget. It is affected by the process heat as well as the mechanical stirring of the welding process. The weld nugget is the core of the weld, where the tool forges and stirs the plasticized material together during the welding process. It experiences the greatest heat and plastic deformation followed by significant grain refinement and re-precipitation.

A refill spot weld cross-section image and its microhardness map are depicted in Figure 3.11. The microhardness measurements in Figure 3.11b are the Vickers hardness values sampled along the midplane lines of the stiffener sheet and the skin sheet of the weld cross-section specimen in Figure 3.11a. Overall, the TMAZ and HAZ exhibit lower hardness values than the parent metal and the weld nugget, which perhaps means they have weaker mechanical strengths than the parent metal and the weld nugget. The effects of the TMAZ and HAZ on the mechanical properties of friction stir welds have been documented by many researchers [34-36, 37].

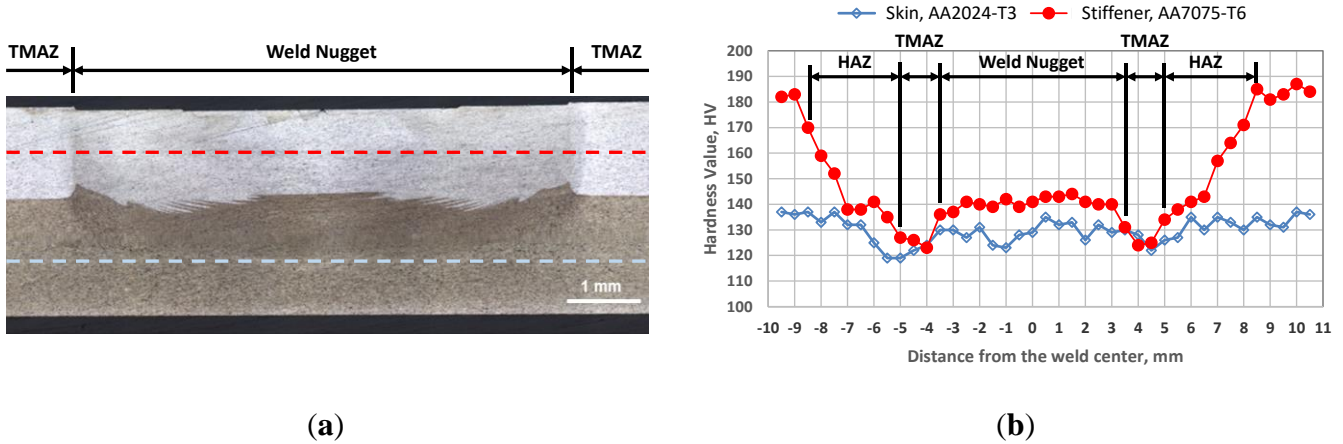


**Figure 3.11. Refill spot weld regions: (a) refill spot weld cross-section image and (b) refill spot weld cross-section microhardness map. The stiffener piece is a 1.27-mm-thick AA7075-T6 sheet, which has a lighter color in the weld cross-section image. The skin piece is a 1.6-mm-thick AA2024-T3 sheet, which has a darker color in the weld cross-section image. The welding process was performed on the stiffener side. The microhardness measurements are the Vickers hardness values sampled along the midplane lines of the stiffener sheet and the skin sheet of the weld cross-section specimen. The hardness measurement lines are indicated by the perforated lines in the weld cross-section image (a). The nominal Vickers hardness values of AA7075-T6 and AA2024-T3 are ~183 HV and ~135 HV, respectively.**

The microstructure of RFSSW exhibits different grain sizes, precipitates, and substructures in different weld zones [38]. A softened region consisted of the weld nugget and the TMAZ. The formation of the softened region can be attributed to coarsening and dissolution of the S-phase precipitates. With the increase in the RFSSW tool spindle speed, the hardness of the weld nugget decreases and the hardness profile of the weld changes from the W-shaped pattern to the U-shaped pattern along the mid-plane lines of the weld cross section [38].

A refill spot weld usually starts to break in the weakest region of the weld under external loading. Figures 3.7a and 3.8a show nugget pullout failures resulting from the static load tests. The rupture of the nugget pullouts exclusively occurred within the TMAZ or HAZ of the refill spot welds as the TMAZ and HAZ are considered the weakest regions of the coupon. During the fatigue

tests, tensile failures were also initiated in the TMAZs of the 4-refill-spot-weld coupon and propagated into the parent metal, as shown in Figure 3.10a.

In general, refill spot weld mechanical failures include nugget pullouts, interfacial failures, and parent metal tensile failures, as documented by Boldsaikhan et al. [30].

- A parent metal tensile failure is a transverse crack across the parent metal sheet, which is caused by the spot weld shear loading—in other words, the parent metal tensile loading. The crack usually originates in the TMAZ and/or HAZ of a refill spot weld and propagates into the parent metal.
- A nugget pullout (NP) involves the weld nugget that is pulled out of the workpieces because of the rupture occurring in the TMAZ and/or HAZ around the outer edge of the spot weld.
- An interfacial failure is a failure at the faying interface between the workpieces so that the interfacial bond fails to hold the workpieces together. It usually occurs within the bottom portion of the spot weld TMAZ if the weld nugget is defect free. An insufficient tool plunge depth or volumetric defect in the weld nugget may lead to an interfacial failure.

A refill spot weld may demonstrate one or a combination of these mechanical failures depending on external loading, parent metal properties, and weld properties. As discussed earlier, the RFSSW process produces different weld regions with different microstructures and mechanical properties. Assuming that the weld nugget is defect free, the TMAZ and HAZ in heat-treatable aluminum alloys are the weakest regions as they exhibit lower hardness values than the parent metal and the weld nugget. Therefore, a mechanical failure usually initiates in the TMAZ and/or HAZ and propagates into new evolving weakest regions of the workpieces under external loading.

The two-spot-weld coupons exclusively demonstrated nugget pullouts during the NASM-1213-4 static load test. The NASM-1312-4 test imposes shear loading on the spot joints. As the two-spot-weld coupon is unguided, it may deform during the shear loading, which, in turn, creates minor tension loading on the joints. Both shear and tension forces can contribute to the formation of nugget pullouts, as described in Figure 3.12 for NASM-1312-4. The cross coupons also exclusively demonstrated nugget pullouts during the ISO-14272 static load test. During the ISO-14272 test, the spot weld experiences tension loading that caused the weld nugget to be pulled out of the parent metal, as depicted in Figure 3.12 for ISO-14272. The four-spot-weld coupons exclusively demonstrated stiffener sheet tensile failures during the NASM-1312-21 fatigue test, as described in Figure 3.12. The NASM-1312-21 fatigue test uses a guide fixture to make sure that pure shear loading is applied to the spot welds. No coupons demonstrated interfacial failures in this study.

Mechanical Tests	Refill Spot Weld Failures	Stiffener		Skin	
		Exterior	Interface	Interface	Exterior
NASM-1312-4 Static Load Lap Shear Test	Stiffener Sheet Nugget Pullout				
ISO-12474 Static Load Cross Tension Test	Stiffener Sheet Nugget Pullout				
NASM-1312-21 Fatigue Lap Shear Test	Stiffener Sheet Tensile Failure				

**Figure 3.12. Mechanical failures of refill spot welds.**

In this study, the mechanical tests examined the shear and tension strengths of refill spot welds through applying shear loading and/or tension loading, as explained earlier. Generally, external loading may impose pure shear loading, pure tension loading, or coupled shear-and-tension loading on a refill spot weld, as illustrated in Figure 3.13. When external loading exceeds a tipping point, a refill spot weld exhibits mechanical failures in its weakest region, as illustrated in Figures 3.14 and 3.15.

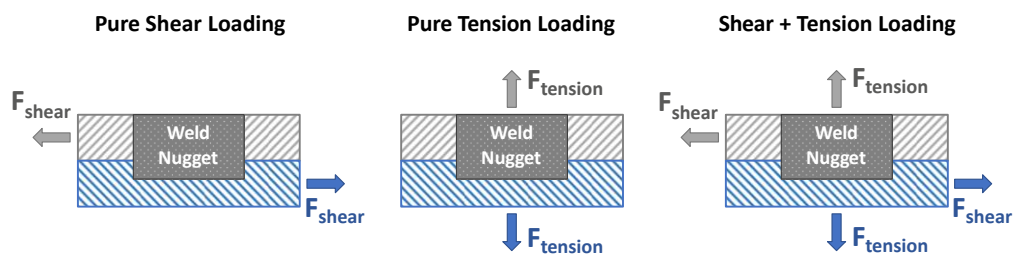
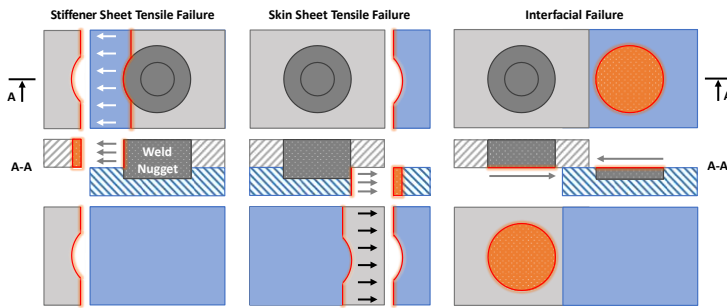


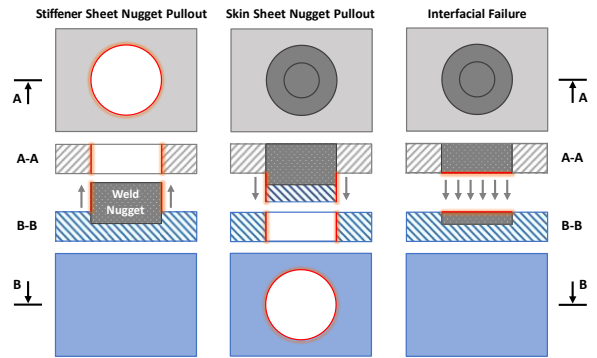
**Figure 3.13. Refill spot weld cross-section schematics with external loading conditions, including pure shear loading, pure tension loading, and shear-and-tension loading.**

### Pure Shear Loading



(a)

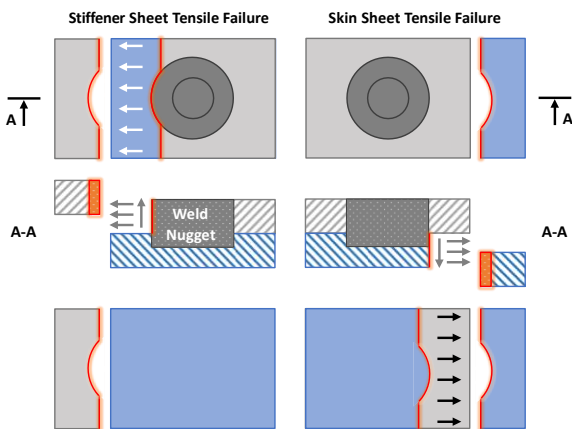
### Pure Tension Loading



(b)

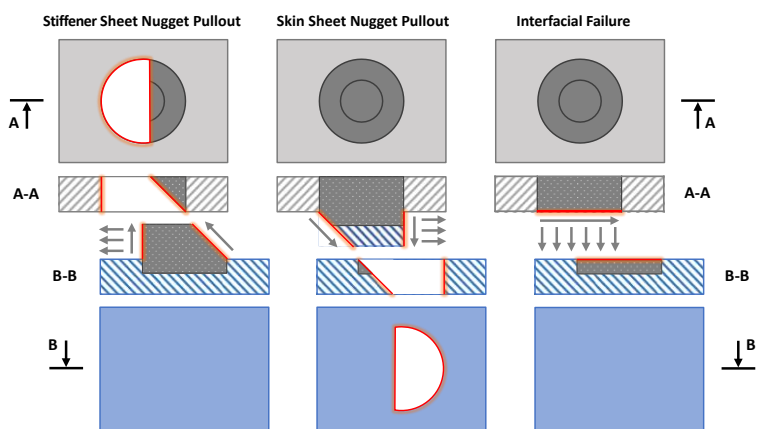
**Figure 3.14. Schematics of refill spot weld failures: (a) parent metal tensile failures and an interfacial shear failure caused by pure shear loading and (b) nugget pullouts and an interfacial tension failure caused by pure tension loading. The graphics of each failure include the top view, the cross-section view, and the bottom view. The failure surfaces are highlighted in orange and red.**

### Shear + Tension Loading



(a)

### Shear + Tension Loading



(b)

**Figure 3.15. Schematics of refill spot weld failures caused by coupled shear-and-tension loading: (a) parent metal tensile failures and (b) nugget pullout failures and an interfacial failure. The graphics of each failure include the top view, the cross-section view, and the bottom view. The failure surfaces are highlighted in orange and red.**

Under pure shear loading, a refill spot weld may demonstrate a stiffener sheet tensile failure, a skin sheet tensile failure, or an interfacial shear failure, as illustrated in Figure 3.14a. The failure mechanism chooses the weakest region to fail first. A refill spot weld demonstrates a stiffener or skin sheet tensile failure if the stiffener or skin sheet is the weakest region. Pure shear loading on the refill spot weld imposes pure tension loading on the parent sheet metals. Therefore, the parent metals may exhibit tensile failures under pure shear loading. In addition, a refill spot weld demonstrates an interfacial shear failure, as illustrated in Figure 3.14a, if the interfacial bond is the weakest region. Factors that make a particular region the weakest region include any possible defects, the properties of the parent metals, and the properties of the weld regions. The properties can be geometric, metallurgical, and/or mechanical.

Under pure tension loading, a refill spot weld may exhibit a stiffener sheet nugget pullout, a skin sheet nugget pullout, or an interfacial tension failure, as illustrated in Figure 3.14b. The failure mechanism chooses the weakest region to fail first. A refill spot weld demonstrates a nugget pullout if the TMAZ or HAZ in the stiffener or skin sheet is the weakest region. A nugget pullout is a shear failure within the TMAZ or HAZ. Pure tension loading on the refill spot weld imposes pure shear loading on the parent sheet metals. In addition, a refill spot weld demonstrates an interfacial tension failure, as illustrated in Figure 3.14b, if the interfacial bond is the weakest region.

Under coupled shear-and-tension loading, a refill spot weld may demonstrate a combination of failures associated with the pure shear loading and the pure tension loading, as illustrated in Figure 3.15. Again, the failure mechanism chooses the weakest region to fail first. Factors that make a particular region the weakest region include any possible defects, the properties of the

parent metals, and the properties of the weld regions. The properties can be geometric, metallurgical, and/or mechanical.

Figures 3.13–3.15 illustrate external loading conditions of a refill spot weld and its failure mechanisms. A refill spot weld may demonstrate one or a combination of mechanical failures, depending on external loading, parent metal properties, and weld properties. As the TMAZ and HAZ exhibit weaker strengths than the parent metal and the weld nugget, a mechanical failure of a refill spot weld usually initiates in the TMAZ and/or HAZ and propagates into new, evolving weakest regions of the workpieces. Understanding these phenomena is necessary to design damage-tolerant refill-spot-welded structures.

## **SUMMARY**

Industrial standards that are typically used for testing rivet joints were implemented in this study to evaluate the mechanical properties of refill spot welds. Therefore, the presented study involved a comparison between the mechanical properties of refill spot welds and the mechanical properties of rivet joints. With that being said, the presented study used an RFSSW tool and a solid rivet of comparable sizes for producing refill spot weld coupons and rivet coupons. The RFSSW coupons demonstrated significantly higher ultimate lap shear strengths but slightly lower ultimate cross-tension strengths than those of the rivet coupons. As suggested earlier, a refill spot weld is made of the workpiece metals via thermomechanical processing, but a rivet joint is made by fastening a solid rivet. The workpieces used in this study are high-strength aerospace aluminum alloys that have much higher strengths than the solid rivet metal. Therefore, having a refill spot weld that has stronger lap shear strength than that of a comparable rivet joint is intuitive. However, a refill spot weld does not have a head and a clenched end to mechanically grip the workpieces

together like solid rivets do, which perhaps explains why the ultimate tension loads of refill spot welds were slightly lower than the ultimate tension loads of rivet joints. The fatigue test results indicate that both RFSSW coupons and rivet coupons demonstrate comparable performances during low-load-level fatigue lap shear tests. However, RFSSW coupons outperformed rivet coupons during high-load-level fatigue lap shear tests as the 75% and 50% load levels of the four-refill-spot-weld coupons were higher than the ultimate loads of the four-rivet-joint coupons.

Refill spot weld mechanical failures include parent metal tensile failures, nugget pullouts, and interfacial failures. A refill spot weld may demonstrate one or a combination of these mechanical failures, depending on external loading, parent metal properties, and weld properties. The RFSSW process produces different weld regions with different microstructures and mechanical properties. Assuming that the weld nugget is defect free, the TMAZ and HAZ of heat-treatable aluminum alloys are the weakest regions as they exhibit lower hardness values than the parent metal and the weld nugget. Therefore, a mechanical failure usually initiates in the TMAZ and/or HAZ and propagates into new, evolving weakest regions of the workpieces under external loading. In general, the failure mechanism chooses the weakest region to fail first. Factors that make a particular region the weakest region include any possible defects, the properties of the parent metals, and the properties of the weld regions. The properties can be geometric, metallurgical, and/or mechanical.

Although the mechanical tests of refill spot welds demonstrated promising results with predictable failure mechanisms, the metallurgical evolution involved in RFSSW remains a subject to study. In addition, RFSSW will need thorough standards and specifications to implement in aerospace applications.

## **CHAPTER 4: PROCESS PARAMETER DEVELOPMENT USING DESIGN OF EXPERIMENTS**

### **OBJECTIVE**

The objective of this study is to develop the process parameters for RFSSW using the Design of Experiments (DOE) method. The optimized weld parameters will be used to produce the fatigue test coupons and the crack growth test coupons.

The main goal of this study is to investigate whether RFSSW is capable of replacing solid rivets in joining the primary aluminum structures of the aircraft. The presented results in this study demonstrate the optimization of process parameters with respect to static strength of the single spot RFSSW coupons by using the Design of Experiments (DOE) method

### **MATERIALS AND METHODOLOGY**

For this study, the RFSSW system shown in **Figure 1.1** was used to weld the coupons. A 9mm tool was used for making welds. The tool consists of a 9mm-diameter shoulder and 5mm-diameter probe that are retractable pieces. The robotic RFSSW system and the tooling were provided by Kawasaki Heavy Industries to support the WSU pillar activities.

Boeing provided sheet metals to the university sites to support the pillar activities of the multisite project. The sheet metals selected by Boeing for their specific application were 0.100"-thick 6013-T6 and 0.125"-thick 2029-T8 panels. In this study, AA6013-T6 panel was used as the Top Sheet (Aircraft Stiffener) and the AA2029-T8 panel was used as the Bottom Sheet (Aircraft Skin). The chemical compositions and the mechanical properties of the sheet metals are provided in Tables 4.1 and 4.2.

**Table 4.1: Chemical composition of AA6013-T6 [28] and AA2029-T8 [29]**

	<b>AA6013-T6, Wt. %</b>	<b>AA2029-T8, Wt. %</b>
<b>Aluminum</b>	Balance	Balance
<b>Silicon</b>	0.6-1.0	0.12 max
<b>Iron</b>	0.5	0.15 max
<b>Copper</b>	0.6-1.1	3.2 – 4.0
<b>Manganese</b>	0.2-0.8	0.20 – 0.40
<b>Magnesium</b>	0.8-1.2	0.8 – 1.1
<b>Chromium</b>	0.1	-
<b>Zinc</b>	0.25	-
<b>Silver</b>	-	0.3 – 0.5
<b>Zirconium</b>	-	0.08 – 0.15
<b>Titanium</b>	0.1	0.10 max
<b>Others, each</b>	0.05	0.05
<b>Others, total</b>	0.15	0.15

**Table 4.2: Mechanical properties of AA6013-T6 and AA2029-T8 [30].**

	<b>AA6013-T6</b>	<b>AA2029-T8</b>
<b>Ultimate Strength (Roll Direction)</b>	378 MPa	439 MPa
<b>Ultimate Strength (Transverse Direction)</b>	369 MPa	435 MPa
<b>Yield Strength (Roll Direction)</b>	299.5 MPa	410 MPa
<b>Yield Strength (Transverse Direction)</b>	284 MPa	378 MPa
<b>Elongation</b>	8%	8%

The weld locations on the skin and the stiffener materials were machined to remove the cladding to allow for bare-to-bare condition to be present at the faying surface. The 0.100”-thick 6013-T6 panel was machined to a thickness of 0.080” and 0.125”-thick 2029-T8 panel was reduced to a thickness of 0.120” through CNC machining. After machining, the sheet metal panels were polished with a 300-grit sandpaper followed by a 1200-grit sandpaper. The machining setup and

the orbital sander that was used for sanding is shown in Figure 3.1. The final sheet metal thicknesses are as follows:

- Top Sheet (**Aircraft Stiffener**):
  - AA6013-T6 with a nominal thickness of 0.080” (2 mm)
- Bottom Sheet (**Aircraft Skin**):
  - AA2029-T8 with a nominal thickness of 0.120” (3 mm)
- Total Workpiece Thickness:
  - 0.200” (5 mm)



**Fig. 4.1: Material preparation: Machining setup (left) and orbital sander (right).**

The initial experimental task was to develop RFSSW process for the given tool material combination. A face-centered central composite design with 16 runs was used for the DoE study. This is a design in which only three levels are required for each factor. It is obtained by essentially setting  $\alpha = 1$  in a Central Composite Design (CCD). The face-centered central composite design is shown in **Figure 3.2**. The DoE method considered three weld parameters, which are the plunge depth, probe speed, and spindle speed. The response variables of the DoE method was the ultimate lap-shear load (failure load) of a single-spot straight coupon. The pull rate of lap shear testing was 1.27 mm/min (.05 inch/min). The DoE results were analyzed with Statgraphics Software.

The factors that were considered for the DoE study are the plunge depth, probe speed and spindle speed. The 3 levels of the DoE factors are as follows:

**Table 4.3: DOE factors and their three levels**

<b>Factors</b>	<b>Low</b>	<b>Medium</b>	<b>High</b>
Plunge Depth	2.1 mm	2.25 mm	2.4 mm
Spindle Speed	1400 rev/min	1600 rev/min	1800 rev/min
Probe Speed	2 mm/s	4 mm/s	6 mm/s

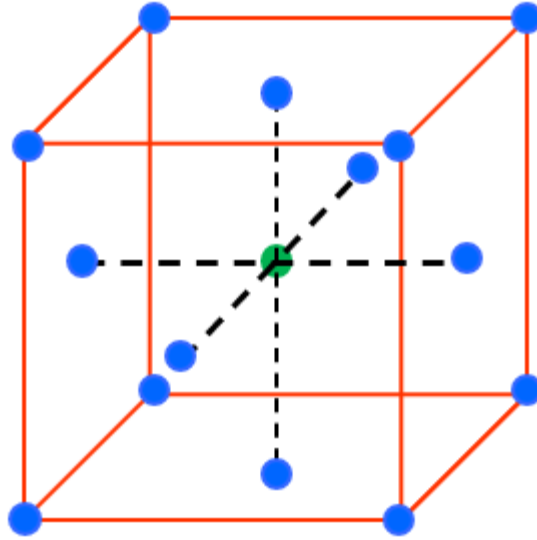


**Fig. 4.2: Face centered central composite design (15+1 runs)**

A single-spot straight coupon is used for identifying the response variable, which is the ultimate lap-shear load (failure load) of a refill spot weld, through the unguided static lap-shear pull testing. The single-spot straight coupon configuration and the weld clamp setup is shown in Figure 4.3. The test setup of the unguided static lap-shear pull testing is depicted in Figure 4.4. No industrial specification was used for testing the single spot straight coupons. The optimized process parameter from this process development experiment was used to produce fatigue test coupons and crack growth test coupons.

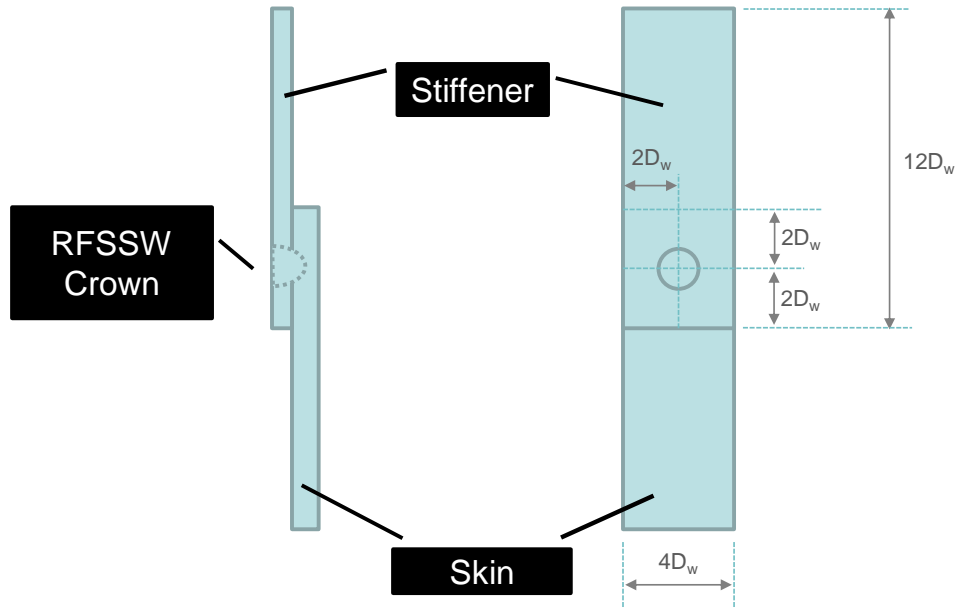


**Fig. 4.3: A single spot straight coupon configuration (top) and weld fixture setup (bottom)**



**Fig. 4.4: Unguided static lap-shear pull test setup.  $D_w$  is the spot weld diameter, which is 9mm.**

## **RESULTS AND DISCUSSION**

Face Centered Central Composite Design was used for the process development, where 16 runs were conducted with 3 repetitions per run and produced 48 single-spot coupons. 13 additional single-spot coupons were produced for further validation. The factors of the Design of Experiments (DoE) were the plunge depth, spindle speed and probe speed of the RFSSW tool.

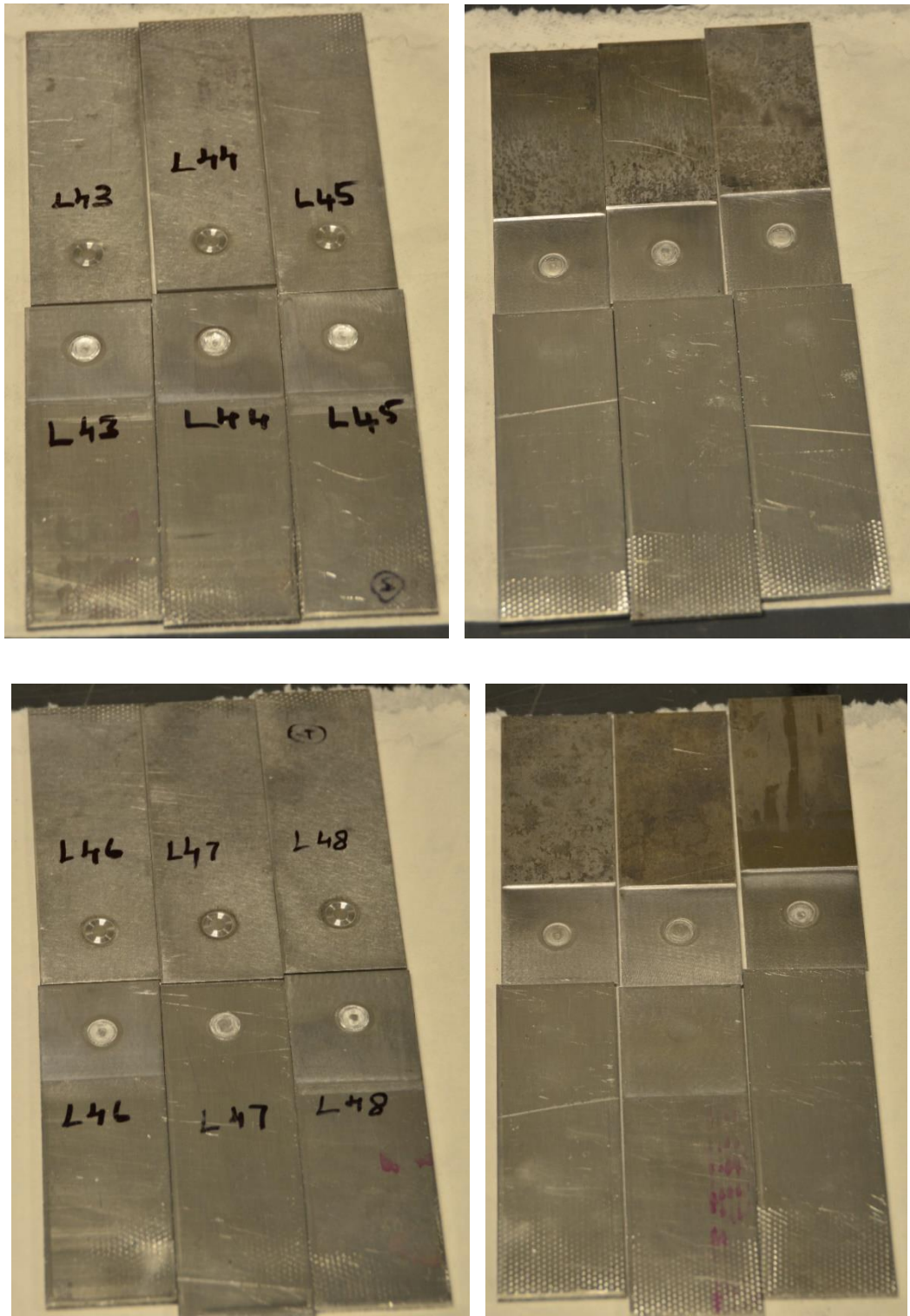
The response variable values were identified after performing the unguided static lap-shear tests on those 48 single-spot coupons. The results were analyzed using the Statgraphics software. The unguided static lap-shear pull testing is shown in Figure 4.3. During the mechanical test, a refill spot joint demonstrated one or a combination of the following types of mechanical failures:

- **Nugget Pullout (NP)** – NP involves a nugget that is pulled out of the base metal, where the failure occurs within the thermo-mechanically affected zone (TMAZ), or heat affected zone (HAZ)
- **Interfacial Failure (IF)** – IF involves an interfacial bond failure so that the workpieces simply separate or “delaminate” from each other through the interfacial bond

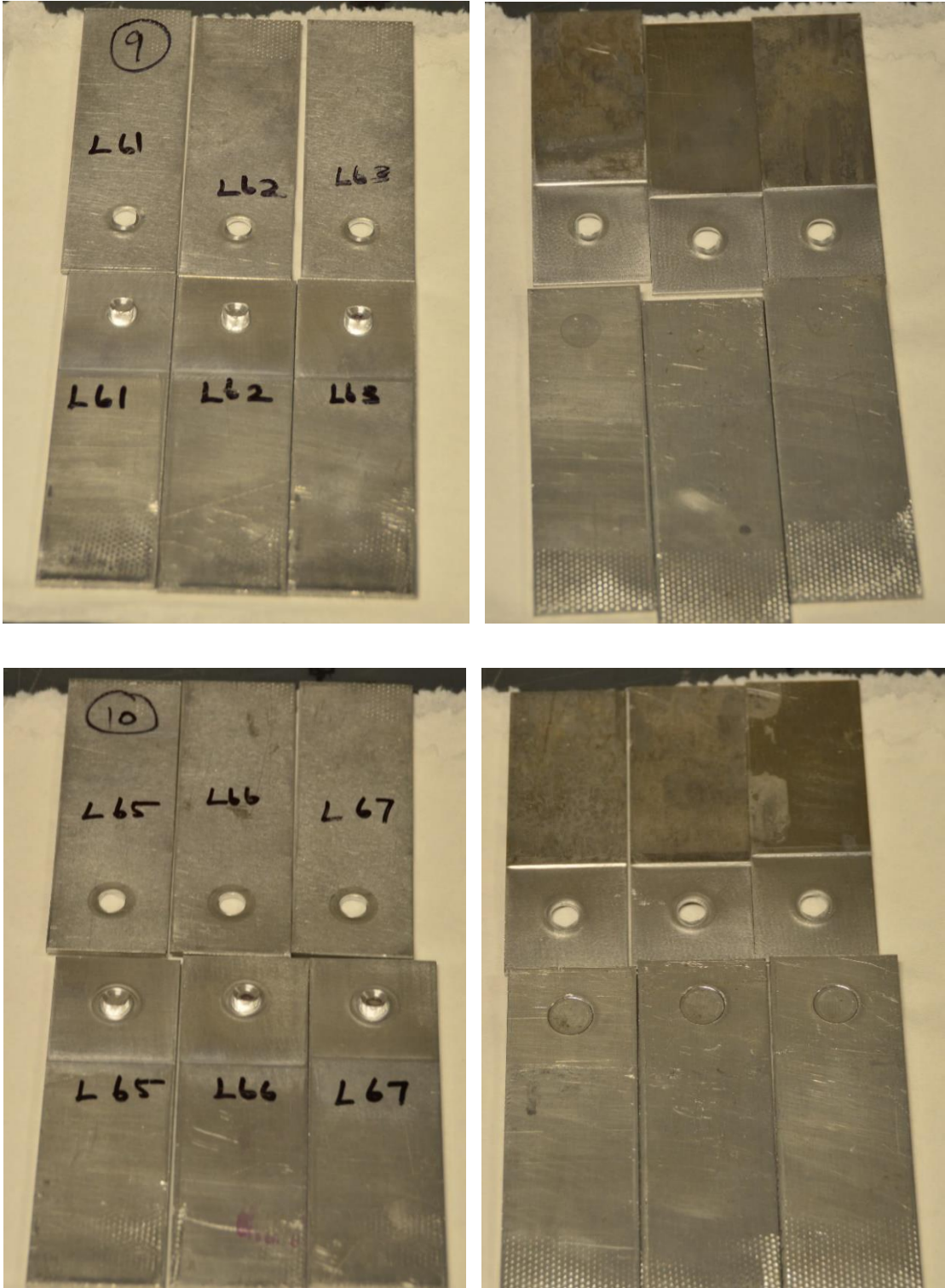
Further details of the DoE test results are provided in Table 4.4. The images of some tested coupons are in Figures 4.5-4.7. Figure 4.5 exhibits interfacial failures and Figure 4.6 exhibits nugget pullouts. In Figure 4.7, Run-10 coupons demonstrate significant dimples on the back side as their weld parameters caused excess heat input during the welding process so that the anvil imprints were formed on the back side of the coupons. The Run-9 coupons do not demonstrate such dimples.

Table 4.4: DoE test results. (NP-Nugget Pullout; IF – Interfacial Failure)

Run	Coupon #	Plunge Depth, mm	Probe Speed, mm/s	RPM	Test 1, lbf	Test 2, lbf	Test 3, lbf	Failure Type
1	L36 - L39	2.4	6	1400	2380.55	2368.87	2396.84	NP (L36, L37) and IF (L39)
2	L40 - L42	2.25	4	1800	2511.44	2168.28	2473.46	IF
3	L43 - L45	2.25	4	1400	2162.75	2270.61	2335.31	IF
4	L46 - L48	2.1	6	1400	2116.94	1572.42	1598.10	IF
5	L49 - L51	2.4	2	1800	2149.64	2038.03	1834.74	NP
6	L52 - L54	2.4	2	1400	2175.32	2149.56	2361.91	NP (L52, L54) and IF (L53)
7	L55 - L57	2.1	4	1600	2155.90	2308.89	1978.33	IF
8	L58 - L60	2.25	2	1600	2111.21	2222.25	1966.33	NP
9	L61 - L63	2.4	6	1800	2435.35	2480.88	2515.01	NP
10	L64 - L67	2.1	2	1400	2098.86	2005.62	2056.51	NP
11	L68 - L70	2.25	4	1600	2516.16	2488.56	2235.53	IF
12	L71 - L73	2.1	6	1800	2176.64	2276.05	2233.71	IF
13	L74 - L76	2.25	6	1600	2392.79	2425.93	2427.28	IF
14	L77 - L79	2.25	4	1600	2457.90	2511.92	2422.47	IF
15	L80 - L82	2.1	2	1800	1902.69	2068.65	1938.11	NP
16	L83 - L85	2.4	4	1600	2449.66	2299.41	2251.46	NP (L84, L85) and IF (L83)



**Fig. 4.5: Front and Back of Run-3 Coupons (Top) and Run-4 Coupons (Bottom). Run-3 and Run-4 Coupons exhibited Interfacial failures.**



**Fig. 4.6: Front and Back of Run-9 Coupons (Top) and Run-10 Coupons (Bottom). Run-9 and Run-10 Coupons exhibited nugget pullout failures.**

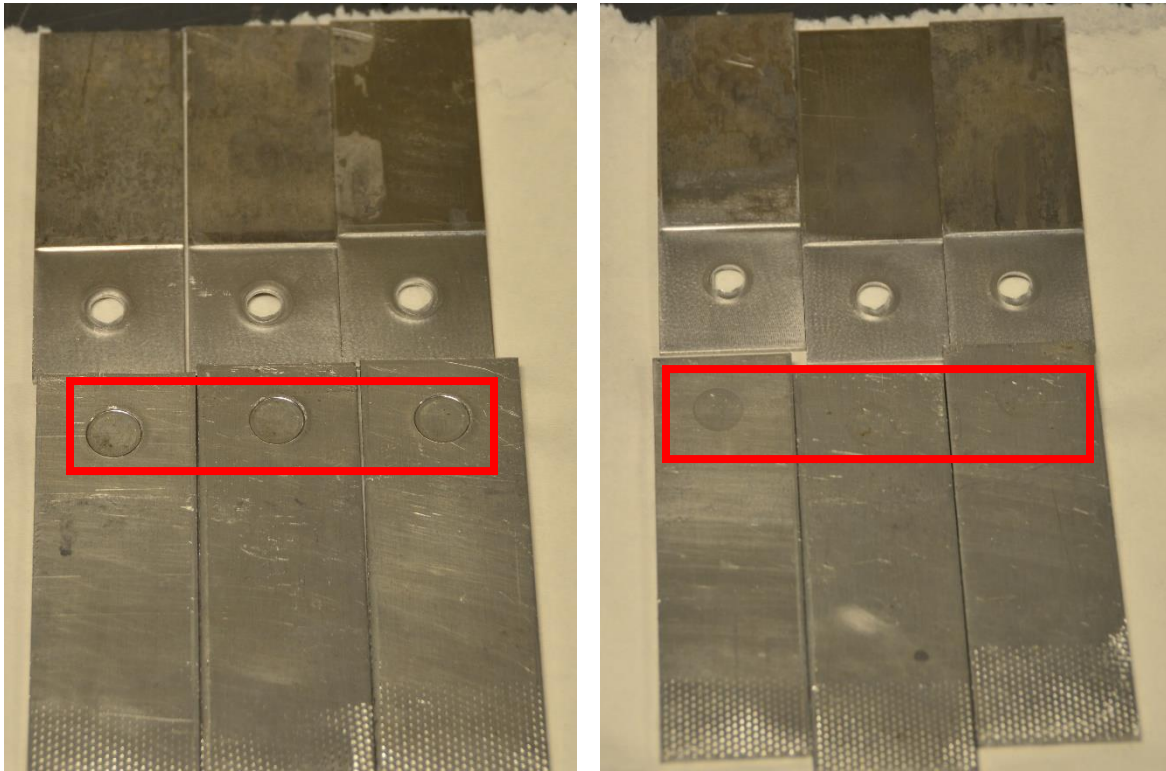


**Fig. 4.7: Run-10 Coupons (Left) and Run-9 Coupons (Right). Run-10 coupons demonstrated significant dimples compared to Run-9 Coupons.**

The main effects plot , the normal probability plot , the residual plot for the failure load is shown in Fig 4.8 and the standardized Pareto chart is shown in Figure 4.9. Each DoE run had 3 repetitions. The failure loads of the DoE coupons were used for estimating a second order response surface. A response surface analysis was performed with the use of the Statgraphic<sup>®</sup> software. The statistics of the response surface analysis are as follows.

- R-squared = 94.5291 %
- Standard Error of Estimation = 77.998 lbf
- Mean absolute error = 38.598 lbf

The R-squared statistic of 94.5291 % indicates that the response surface as fitted explains 94.5595% of the variability in the failure load. The standard error of the estimate shows the standard deviation of the residuals to be 77.998 lbf. The mean absolute error (MAE) of 38.598 lbf is the average value of the residuals. The Analysis of Variance (ANOVA) for the failure load is given in Table 4.5. In this case, 5 effects had significant effect on the failure load since all these effects have a p-value less than .05.

**Table 4.5: Analysis of Variance for Failure Load**

Source	Sum of Squares	Df	Mean Square	F-Ratio	P-Value
A:PlungeDepth	160428	1	160428	27.78	0.0019
B:Probe Speed	82080	1	82080	14.21	0.0093
C:Spindle Speed	14758.7	1	14758.7	2.56	0.161
AA	35667.9	1	35667.9	6.18	0.0475
AB	53621.6	1	53621.6	9.28	0.0226
AC	32377.5	1	32377.5	5.61	0.0557
BB	25993.3	1	25993.3	4.5	0.0781
BC	93874.4	1	93874.4	16.25	0.0069

According to the main effects plot, the plunge depth and probe speed had the strongest positive effect on the ultimate shear strength. Deeper plunge depths produced stronger bonds. However, the tool plunging beyond a certain depth will result in degradation of the material properties of the coupon. Hence, the plunge depth was maintained between 2.1 mm and 2.4 mm, which is 10% of the bottom sheet thickness. Figure 4.7.1 illustrates the optimum plunge depth of the tool.

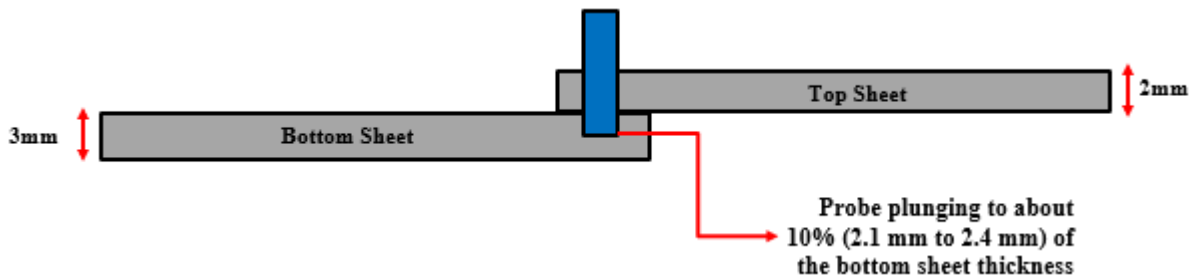


**Figure 4.7.1: Illustrates the optimum plunge depth of the tool.**

Similarly, faster probe speeds produced stronger bonds, but increased probe travel speeds will lead to weaker bonds since the low thermal energy produced during the process would be insufficient to plasticize the material. Likewise, slower travel speed can induce very high heat input which might degrade the material properties of the coupon. Hence, an optimum range between 2 mm/sec to 6 mm/sec was maintained.

The spindle speed had less significant effect on the ultimate shear load compared to plunge depth and probe speed. Higher spindle speed produced higher ultimate shear load. However, very high spindle speeds may introduce excess heat input to the workpiece and may degrade the microstructural and mechanical properties of the joint. On the other hand, very low spindle speeds may not be able to produce the required heat to plasticize the workpiece material and this might lead to volumetric defects in the joints. In worst case scenario, low spindle speed might even result in RFSSW tool failure. Hence the spindle speed was always maintained between 1400 rev/min to

1800 rev/min to prevent any failures and defects. The normal probability plot in Figure 4.8b shows that there is very little deviation in the observation. This shows that the data is a good fit and is normally distributed. The residual plot shows very little variability. In the residual plot the residuals are plotted against the predicted values. Also, there are other indications showing that the assumption of our model is false. According to the Pareto chart in Figure 4.9, the plunge depth and the probe speed have statistically significant effects on the failure load. And the spindle speed had less significant effect on the ultimate shear load compared to plunge depth and probe speed.

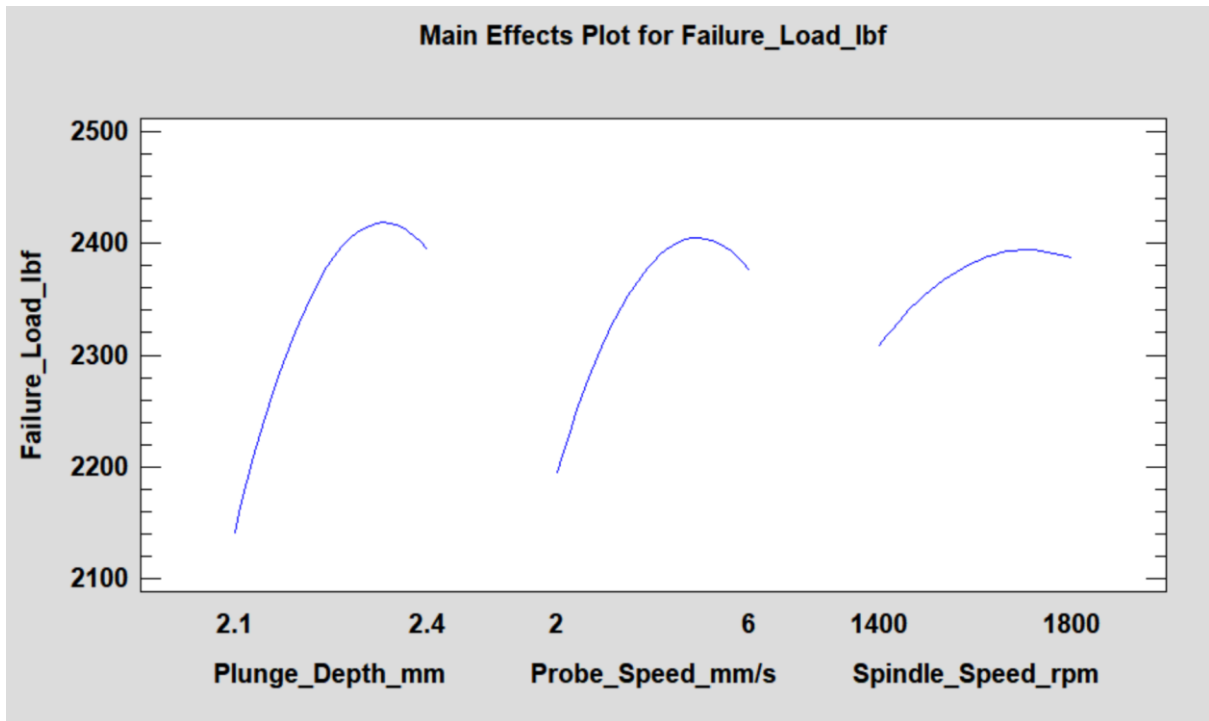


**Fig. 4.8: Main effects plot (a). Normal probability plot (b). Residual plot (c)**

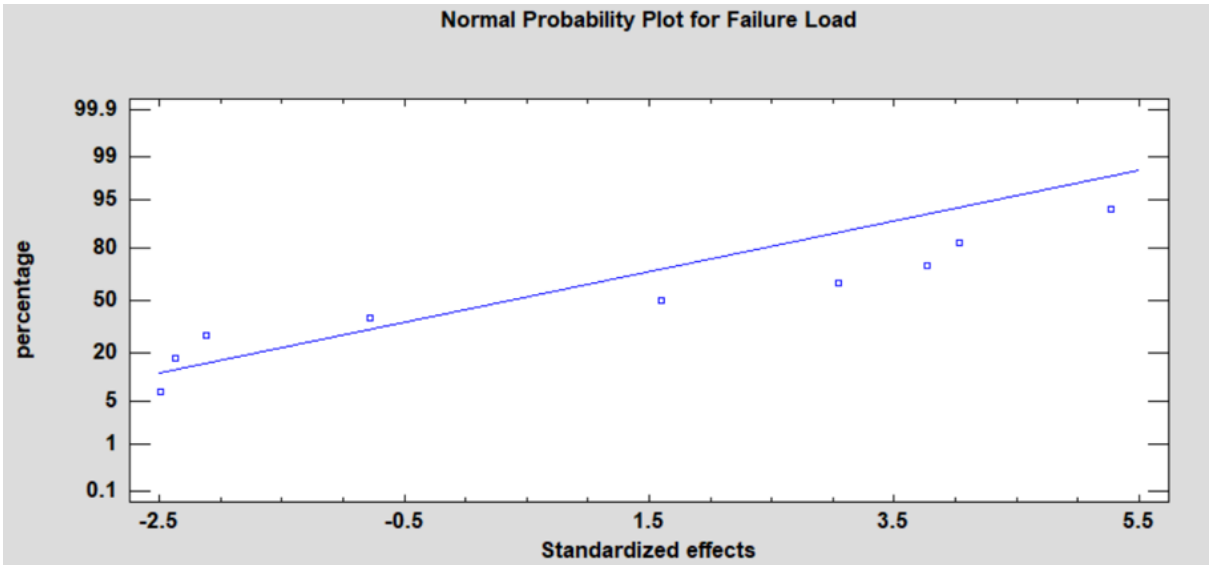


Fig. 4.8 (continued)

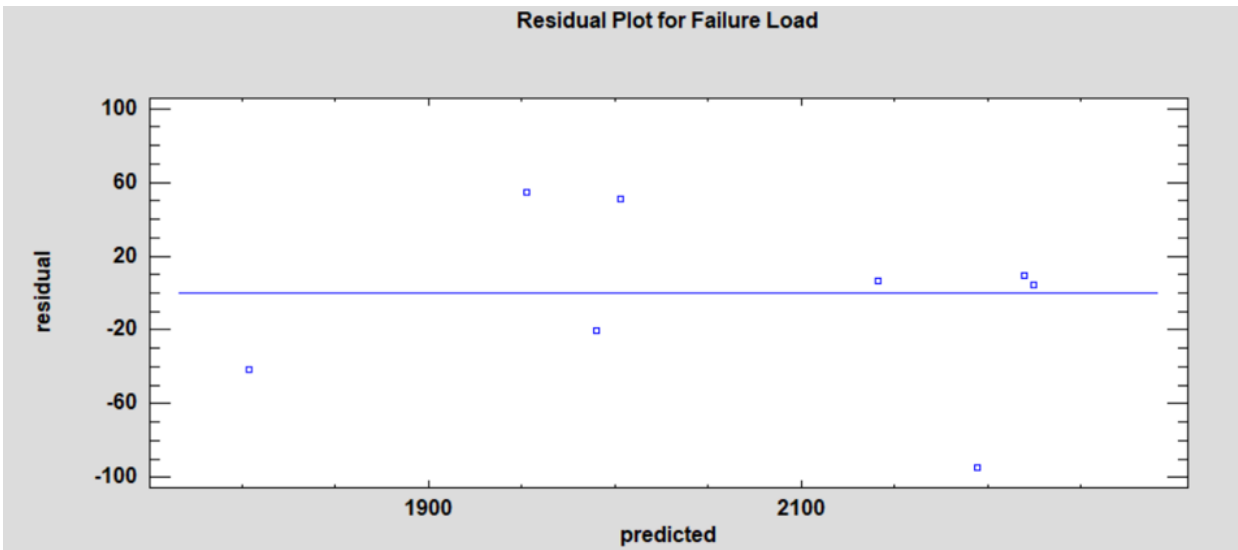
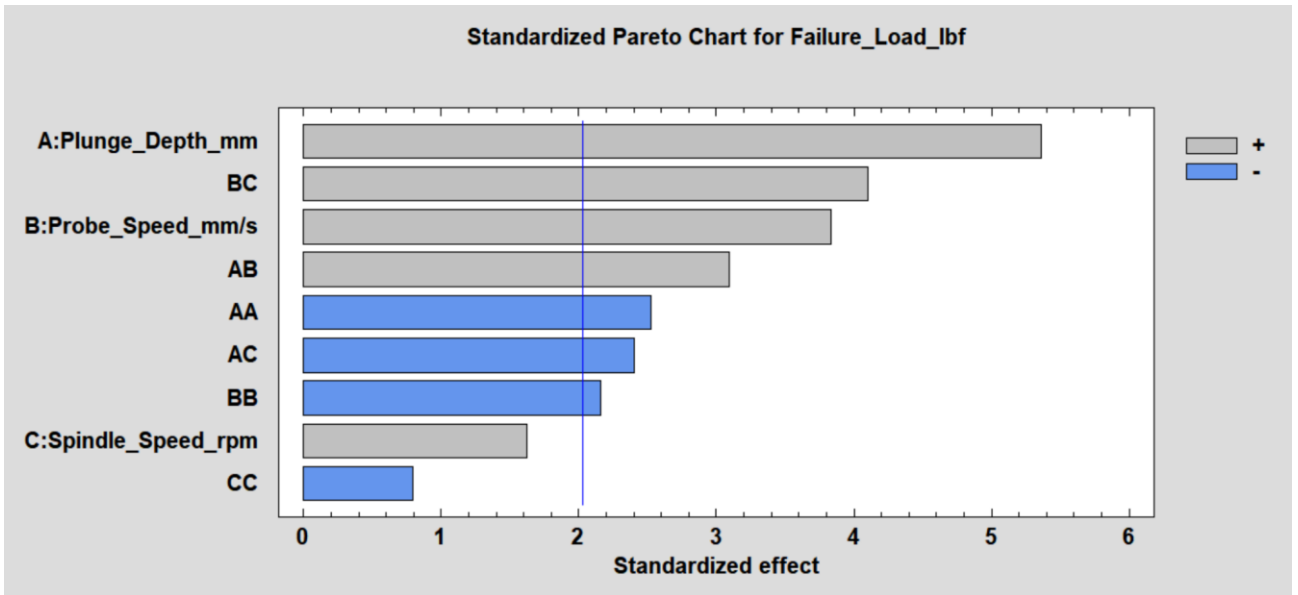


Fig. 4.8 (continued)



**Fig. 4.9: Standardized Pareto chart for failure load.**

According to the DoE results, the Run-9 weld parameters produced acceptable results. The Run-9 coupons produced nugget pullout failures. This indicates stronger bonds were produced with the Run-9 parameters. Unlike IF failures, NP failures occur when the bond is stronger than the parent metal. In interfacial failures, the workpieces simply separate or “delaminate” due to weak bond. The weaker bonding is a result of a lack of plunge depth during the welding process. To further explore the validity of Run 9, additional coupons were produced with the weld parameters of Run 1, Run 9, and Run 17 as specified in Table 4.6. The static test results of the additional coupons are provided in Table 4.5 as well. Figure 4.10 exhibits additional Run-1 coupons. Figure 4.11 and Figure 4.12 exhibit post-test Run-9 coupons and Run-17 coupons, respectively. All Run-1 coupons demonstrated interfacial failures. All Run-9 coupons demonstrated nugget pullouts, except L91 and L93. All Run-17 coupons demonstrated interfacial failures, except L89. The bar chart in Figure 4.13 encompasses the overall results of Run 1, Run 9, and Run 17 involved in both DoE and its validation experiments. According to Figure 4.13, the Run-9 weld parameters

demonstrate the best strength. Therefore, the Run-9 weld parameters were selected for producing four-spot coupons for the fatigue study.

**Table 4.6: DoE validation experiment results (13 coupons).**

Coupon #	Plunge Depth, mm	Probe Speed, mm/s	RPM	Test 1, lbf	Test 2, lbf	Test 3, lbf	Test 4, lbf	Test 5, lbf	Failure Type
L95 - L98 (Run 1)	2.4	6	1400	2231.11	2356.41	2291.27	2395.85		IF (all)
<u>L91 - L94</u> (Run 9)	<u>2.4</u>	<u>6</u>	<u>1800</u>	<u>2385.87</u>	<u>2416.05</u>	<u>2486.37</u>	<u>2461.15</u>		<u>L91, L93</u> <u>(IF)</u> <u>L92, L94</u> <u>(NP)</u>
L86 - L90 (Run 17)	2.4	6	1600	2364.27	2433.87	2382.83	2494.20	2415.81	all IF except L89 (NP)

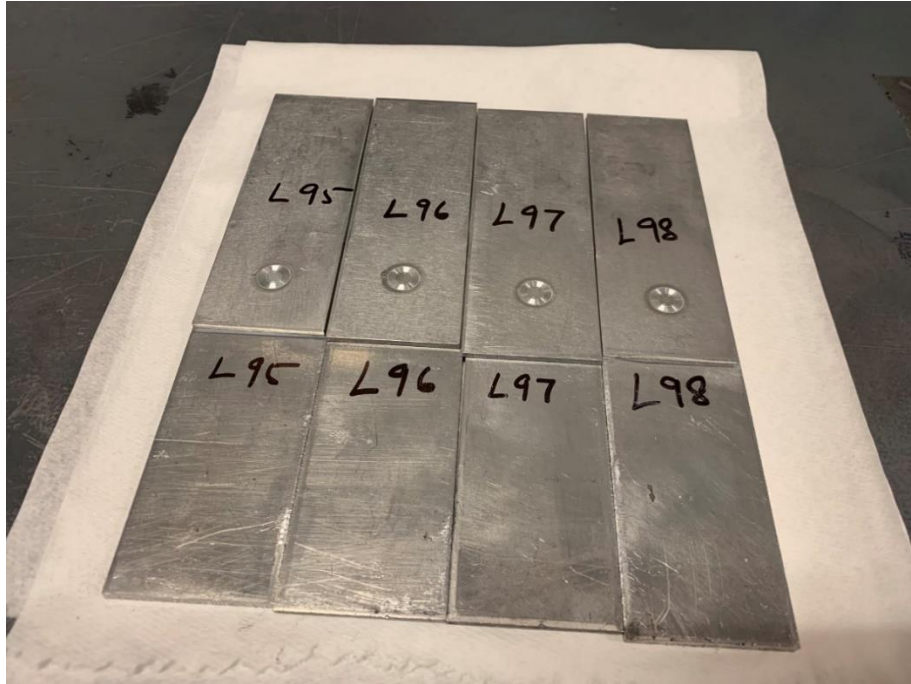


**Fig. 4.10: Front and back of additional Run-1 coupons. All Run-1 coupons demonstrated interfacial failures**

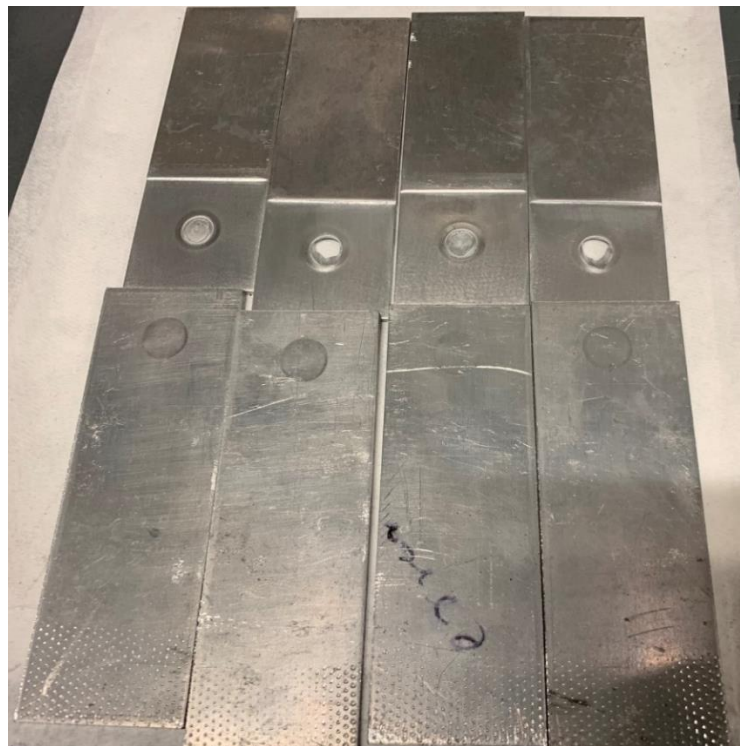
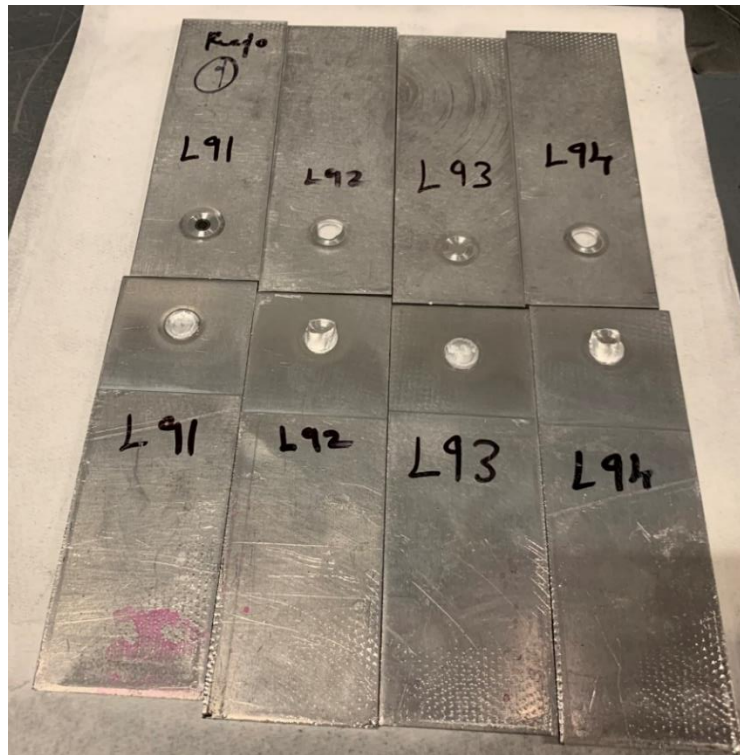


**Fig. 4.11: Front and back of additional Run-9 coupons after unguided static lap-shear pull tests. All Run-9 coupons demonstrated nugget pullouts, except L91 and L93.**

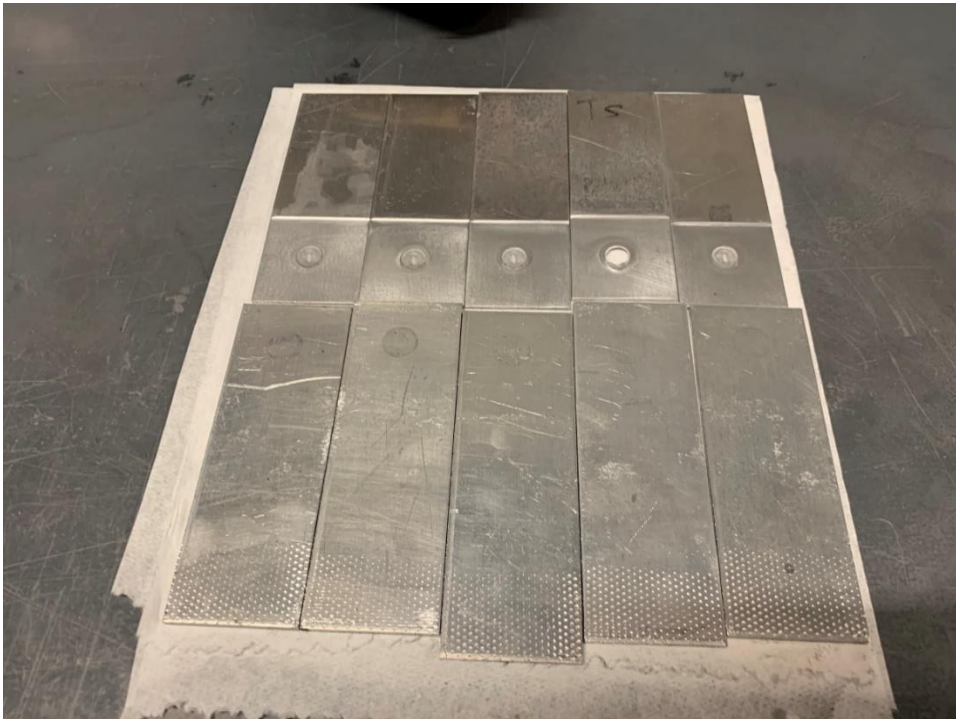
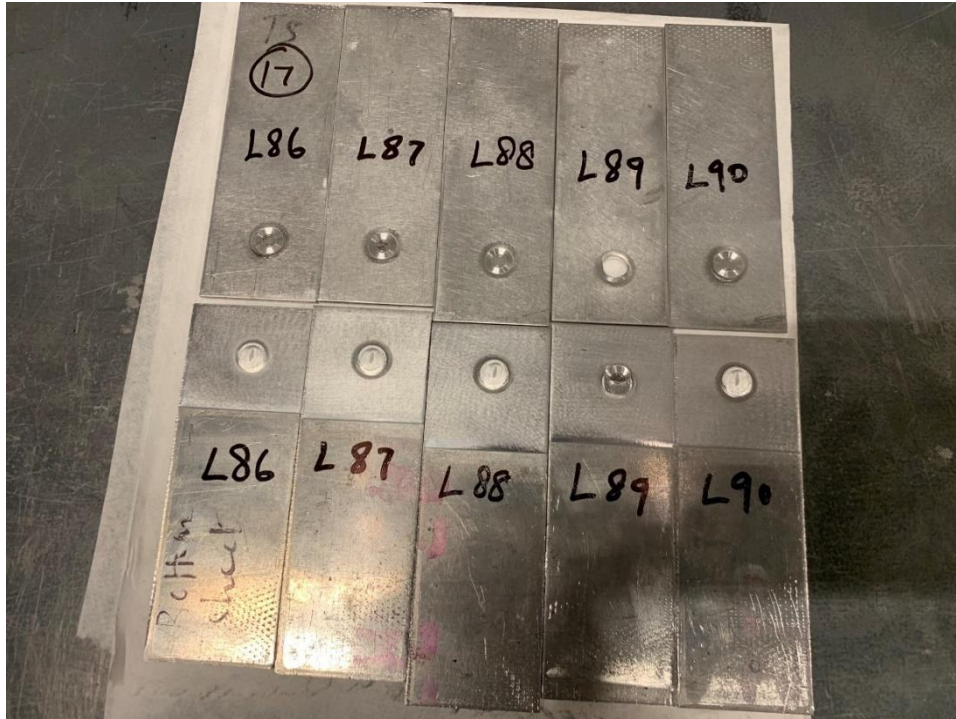


**Fig. 4.12: Front and back of Run-17 coupons after unguided static lap-shear pull tests. All Run-17 coupons demonstrated interfacial failures, except L89**

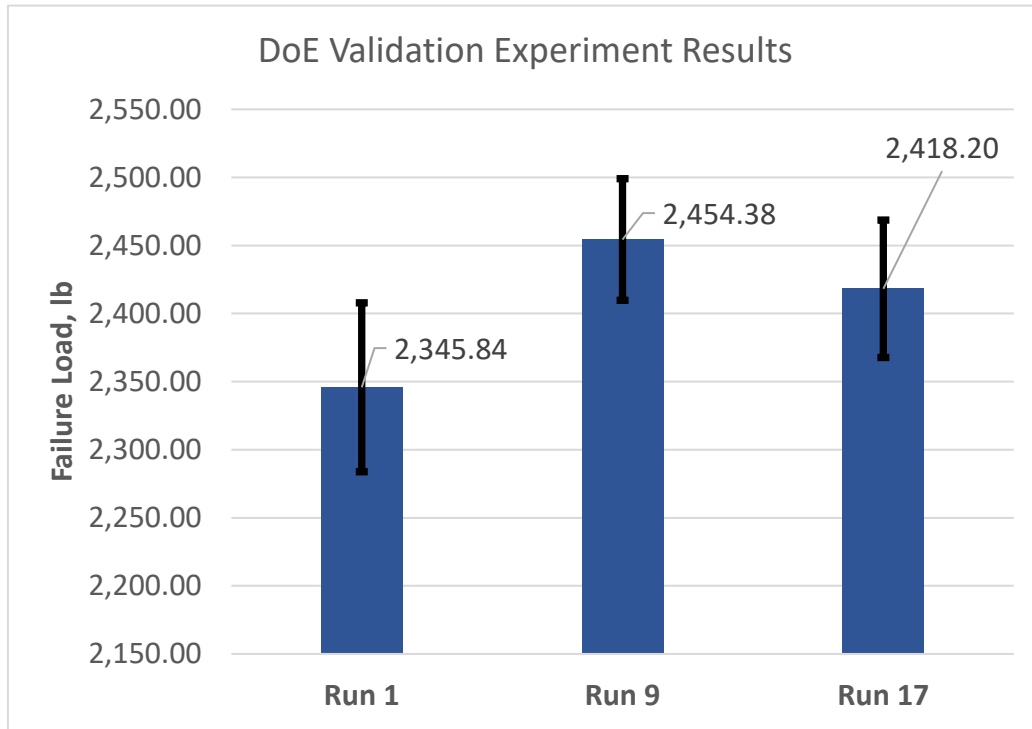


**Fig. 4.13: Unguided static lap-shear pull test results of DoE validation experiment.**

## SUMMARY

The objective of this study is to develop the process parameters for RFSSW using the Design of Experiments (DOE) method. The optimized weld parameters will be used to produce the fatigue test coupons and the crack growth test coupons.

The RFSSW process was developed with the use of a Design-of-Experiments (DoE) method. A face-centered central composite design with 16 runs was used for the DoE study. This is a design in which only three levels are required for each factor. It is obtained by essentially setting  $\alpha = 1$  in a central Composite Design (CCD). The DoE method considered three weld parameters, which are the plunge depth, probe speed, and spindle speed of the weld tool, as the DoE factors. The response

variable of the DoE method was the ultimate lap-shear load (failure load) of a single spot straight coupon.

In total 16 runs with different combinations of weld parameters were used. According to the DoE results, out of the 16 runs, the Run-9 and Run-1 weld parameters produced acceptable results. The Run-9 coupons produced nugget pullout failures and Run-1 produced interfacial failures. NP failures occur when the bond is stronger than the parent metal. Interfacial failures occur when there is a lack of plunge depth, and the weld fails at the interface due to lack of stronger bonds. This indicates that the coupons produced with Run 9 weld parameters produced stronger bonds compared to coupons produced with Run 1 parameters. To further explore the validity of Run 9, additional coupons were produced with the weld parameters of Run 1, Run 9, and Run 17. According to the results, the Run-9 weld parameters demonstrated the best strength compared to Run 1 and Run 17. Therefore, the Run-9 weld parameters were selected for producing four-spot coupons and crack growth test coupons for the fatigue and crack growth analysis study.

## CHAPTER 5: FATIGUE CHARACTERIZATION AND CRACK GROWTH ANALYSIS OF REFILL FRICTION STIR SPOT WELDED COUPONS

### INTRODUCTION

Fatigue is a process of damage accumulation in a material undergoing fluctuating loading. To describe the mechanical fatigue process, different parameters are used, like cyclic load, stress intensity, and crack growth rate.  $P_{max}$  is the maximum load,  $P_{min}$  [kN] is the minimum load and the ratio between the minimum and maximum load ( $P_{min}/P_{max}$ ) is used to measure the mean stress, called the load ratio  $R$ . Crack growth rate is given by  $da/dN$ , where  $da$  is the crack increment and  $dN$  is the loading cycle increment. The stress intensity factor  $K$  [ $MPa\sqrt{m}$ ], is calculated from the applied load  $P$ . The maximum stress intensity is  $K_{max}$ , the minimum  $K_{min}$  and the difference between  $K_{max}$  and  $K_{min}$  is given by  $\Delta K$ . As the material is exposed to repeated stress or load cycles, microscopic cracks may open. This happens when the stress intensity factor reaches the critical value that is needed to pen the crack ( $K_{max} = K_{opening}$ ). The cracks that open tend to grow when they are exposed to cyclic loading. Once the crack starts growing, even if the maximum load ( $P_{max}$ ) is below the elastic limit of the material, fatigue may cause the structure to fail.

Fatigue is a progressive process. In the early stages the crack starts to develop slowly and when it nears the end of a structure's life it starts to accelerate very quickly towards failure. This failure of structures by fracture is primarily due to the formation and propagation of cracks beyond a certain size. During load cycles, crack initiates and propagates and during unloading or compressive part of the cycles, re-sharpening of the crack tip takes place [49]

## **OBJECTIVE**

The objective of the fatigue study is to investigate fatigue performances of RFSSW with the use of an existing aerospace standard so that the fatigue performances of RFSSW can be compared with existing joining technologies, such as mechanical fastening, resistance spot welding, etc. The results of this study will also be instrumental to advance the RFSSW process to Technology Readiness Level (TRL) 6. The DoE method was used for optimizing the weld parameters. The optimized parameters were used for producing fatigue test coupons with the 9mm tool.

## **MATERIALS AND METHODOLOGY**

For this study, the RFSSW system shown in **Figure 1.1** was used to weld the coupons. A 9mm tool was used for making welds. The tool consists of a 9mm-diameter shoulder and 5mm-diameter probe that are retractable pieces. The robotic RFSSW system and the tooling were provided by Kawasaki Heavy Industries to support the WSU pillar activities.

Boeing provided sheet metals to the university sites to support the pillar activities of the multisite project. The sheet metals selected by Boeing for their specific application were 0.100"-thick 6013-T6 and 0.125"-thick 2029-T8 panels. In this study, AA6013-T6 panel was used as the Top Sheet (Aircraft Stiffener) and the AA2029-T8 panel was used as the Bottom Sheet (Aircraft Skin). The chemical compositions and the mechanical properties of the sheet metals are provided in Tables 5.1 and 5.2.

**Table 5.1: Chemical composition of AA6013-T6 [28] and AA2029-T8 [29]**

	<b>AA6013-T6, Wt. %</b>	<b>AA2029-T8, Wt. %</b>
<b>Aluminum</b>	Balance	Balance
<b>Silicon</b>	0.6-1.0	0.12 max
<b>Iron</b>	0.5	0.15 max
<b>Copper</b>	0.6-1.1	3.2 – 4.0
<b>Manganese</b>	0.2-0.8	0.20 – 0.40
<b>Magnesium</b>	0.8-1.2	0.8 – 1.1
<b>Chromium</b>	0.1	-
<b>Zinc</b>	0.25	-
<b>Silver</b>	-	0.3 – 0.5
<b>Zirconium</b>	-	0.08 – 0.15
<b>Titanium</b>	0.1	0.10 max
<b>Others, each</b>	0.05	0.05
<b>Others, total</b>	0.15	0.15

**Table 5.2: Mechanical properties of AA6013-T6 and AA2029-T8 [30].**

	<b>AA6013-T6</b>	<b>AA2029-T8</b>
<b>Ultimate Strength (Roll Direction)</b>	378 MPa	439 MPa
<b>Ultimate Strength (Transverse Direction)</b>	369 MPa	435 MPa
<b>Yield Strength (Roll Direction)</b>	299.5 MPa	410 MPa
<b>Yield Strength (Transverse Direction)</b>	284 MPa	378 MPa
<b>Elongation</b>	8%	8%

The weld locations on the skin and the stiffener materials were machined to remove the cladding to allow for bare-to-bare condition to be present at the faying surface. The 0.100”-thick 6013-T6 panel was machined to a thickness of 0.080” and 0.125”-thick 2029-T8 panel was reduced to a thickness of 0.120” using a CNC machine. After machining, the sheet metal panels were polished with a 300-grit sandpaper followed by a 1200-grit sandpaper. The machining setup and the orbital

sander that was used for sanding is shown in Figure 5.1. The final sheet metal thicknesses are as follows:

- Top Sheet (**Aircraft Stiffener**):
  - AA6013-T6 with a nominal thickness of 0.080" (2 mm)
- Bottom Sheet (**Aircraft Skin**):
  - AA2029-T8 with a nominal thickness of 0.120" (3 mm)
- Total Workpiece Thickness:
  - 0.200" (5 mm)



**Fig. 5.1: Material preparation: Machining setup (left) and orbital sander (right).**

The optimized process parameters from the previous study were used for producing 4 spot coupons and the crack growth analysis test coupons. The optimized weld parameters is shown in Table 5.3.

**Table 5.3: Optimized Weld Parameters**

Plunge Depth	Probe Speed	Spindle Speed
2.4 mm	6 mm/s	1800 rev/min

The 4-spot coupon configuration and the weld clamp setup is shown in Figure 5.2. The fatigue tests were carried out in accordance with NASM 1312-21 [32]. The NASM 1312-21 test method covers the testing procedure and apparatus required to test the shear joint fatigue of fasteners at room temperature. This test requires a guide fixture. The Guide fixture and the NASM 1312-21 test setup is shown in Figure 5.3. The welded 4 spot coupons is depicted in Figure 5.4.

The following load conditions were used for performing the fatigue tests of four-spot coupons according to NASM1312-21:

- Ultimate Load Identification (Failure Load Identification):
  - 5 static pull tests with a pull rate of 1.27 mm/min
- Fatigue Load Levels:
  - 35% of the ultimate load with 5 fatigue tests (5 coupons)
  - 25% of the ultimate load with 5 fatigue tests (5 coupons)

- 15% of the ultimate load with 5 fatigue tests (5 coupons)
- Minimum/Maximum Load Ratio:
  - $R = 0.1$
- Frequency:
  - 20 Hz

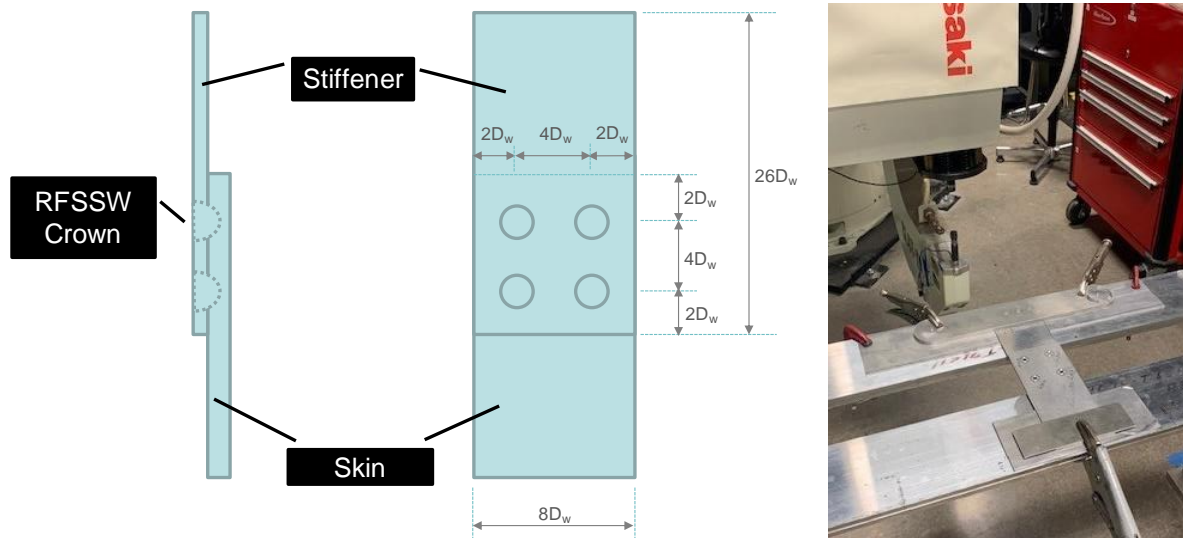


**Fig. 5.2: NASM-1312-21 coupon configuration (left) and weld clamp setup (right).  $D_w$  is the spot weld diameter, which is 9mm.**

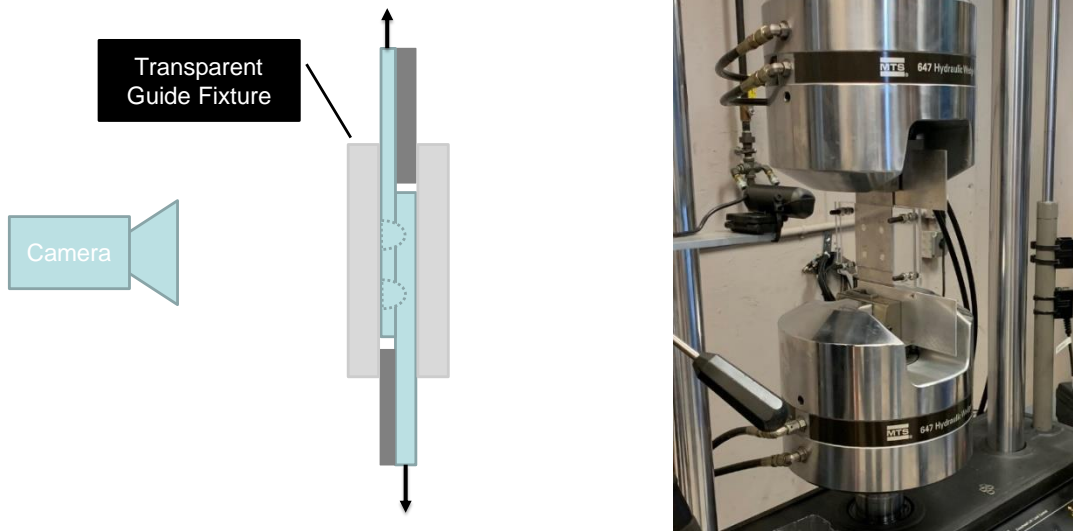


**Fig. 5.3: NASM-1312-21 guided lap-shear pull test setup.**



**Fig. 5.4: Welded 4 spot coupons**

The crack location on the crack growth analysis test coupons is based on the failures demonstrated by the 4 spot coupons. The circular notch geometry was selected due to its simplicity and similarity to the rivet hole. The notch was machined using a CNC machine with a 3/8-inch milling tool. The notch geometry that was used for the crack growth study is shown in Fig 5.5.

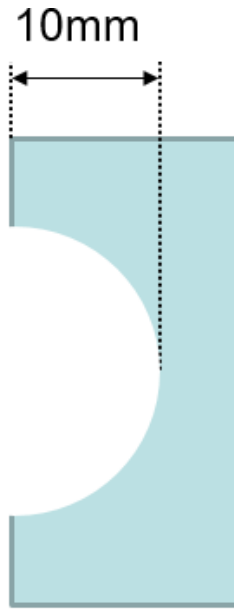


**Fig. 5.5: Notch geometry.**

In total 12 test coupons were prepared. Three top sheet parent metal coupons, three bottom sheet parent metal coupons, three top sheet welded coupons and three bottom sheet welded coupons were prepared. The welded coupons were produced with 4D pitch and 2D edge margin dimension (D is the spot Diameter).

The fatigue tests were carried out in accordance with NASM 1312-21 [32]. This test method covers the procedure and apparatus required for testing the shear joint fatigue of fasteners at room temperature.

The following fatigue test parameters were used for performing the fatigue tests of crack growth test coupons.

- Fatigue Load Levels for the top sheet coupons:
  - 35% of the ultimate load of the top sheet (439 Mpa) (3 coupons)

- 25 Hz
- $R = 0.1$
- Fatigue Load Levels for the bottom sheet coupons:
  - 35% of the ultimate load of the bottom sheet (439 Mpa) (3 coupons)
  - 25 Hz
  - $R = 0.1$

The coupon configuration for the crack growth analysis test and the weld clamp setup are shown in Figure 5.6 and Figure 5.7. The top sheet parent metal coupons are shown in Figure 5.8 and the welded top sheet welded is shown in Figure 5.9. The bottom sheet parent metal coupons are shown in Figure 5.10 and the welded bottom sheet coupons is shown in Figure 5.11.

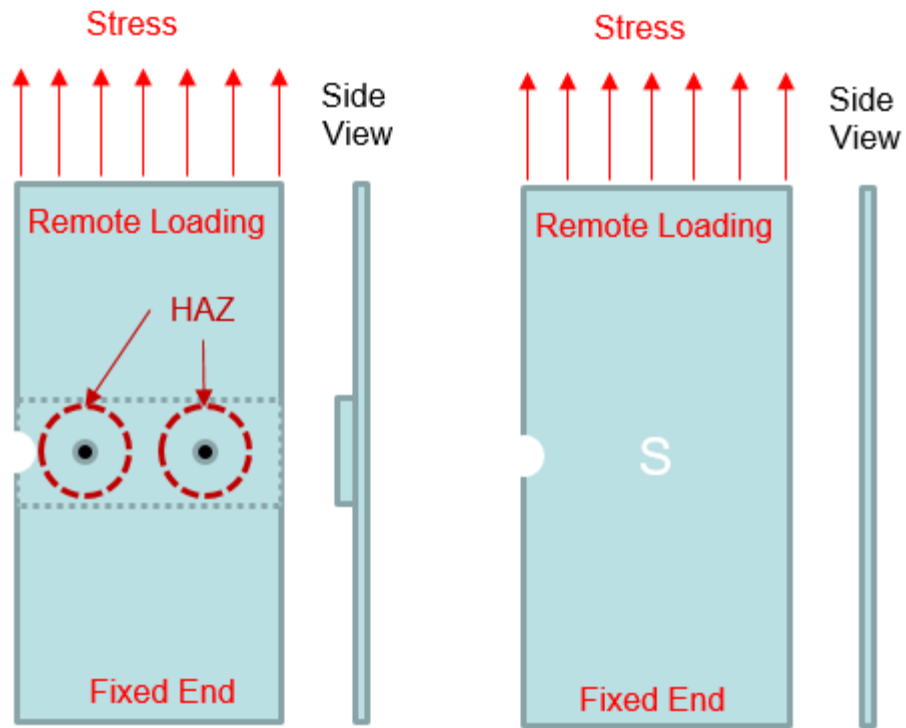


**Fig. 5.6: Coupon configuration for the crack growth analysis.**

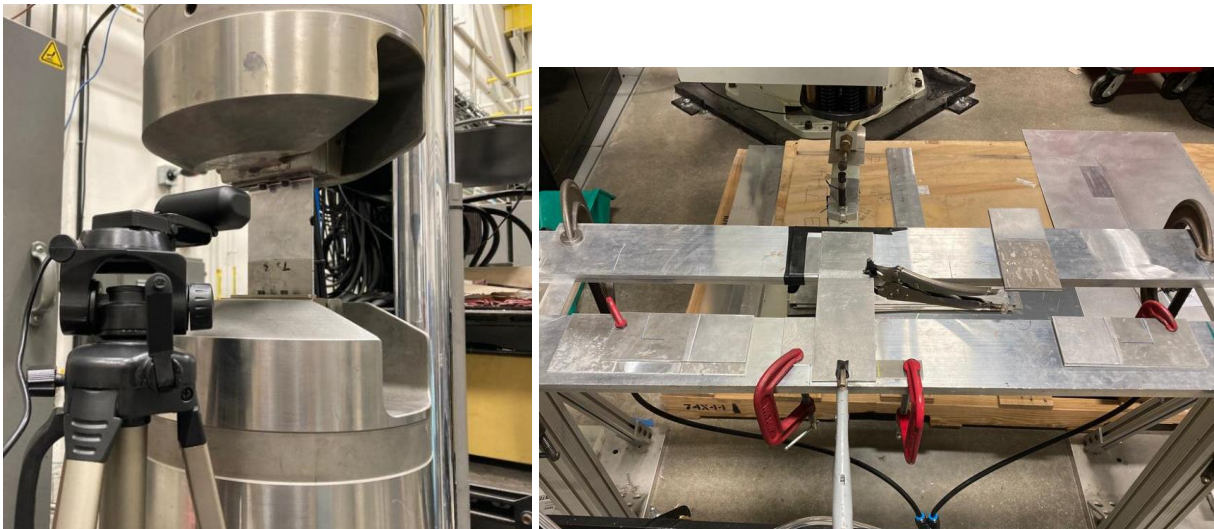


**Fig. 5.7: NASM-1312-21 lap-shear pull test setup (Left). Weld fixture setup for crack growth analysis test coupons (Right).**

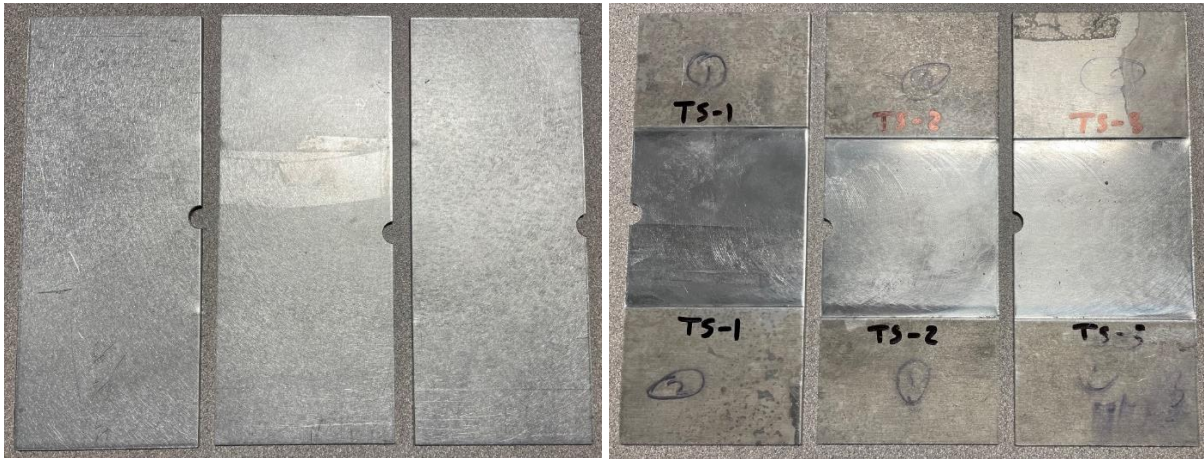


**Fig. 5.8: Front and back side of the top sheet parent metal coupons.**



**Fig. 5.9: Front and back side of the bottom sheet parent metal coupons.**



**Fig. 5.10: Front and back side of the top sheet welded coupons.**



**Fig. 5.11: Front and backside of the bottom sheet welded coupons.**

## RESULTS

### Fatigue Test

In total, 20 four-spot coupons were produced using the optimized Run-9 weld parameters. 5 four-spot coupons were used for identifying the ultimate load (the failure load) for the fatigue testing. The guided lap-shear pull test setup for four-spot coupons is shown in Figure 5.7. The

four-spot coupons exclusively demonstrated parent metal tensile failures during the guided static and fatigue tests. The cracks initiated in the HAZ/TMAZ and propagated into the parent metal in a direction that is orthogonal to the loading direction. The crack initiation and propagation in the 4 spot welded coupons is shown in Figure 5.13.

- **Top-Sheet Tensile Failure (TSTF)** – TSTF involves a crack initiate in TMAZ / HAZ and propagates into the top-sheet parent metal in a direction that is orthogonal to the loading direction as shown in Figure 5.12.
- **Bottom-Sheet Tensile Failure (BSTF)** – BSTF involves a crack initiate in TMAZ / HAZ and propagates into the bottom-sheet parent metal in a similar way of TSTF.

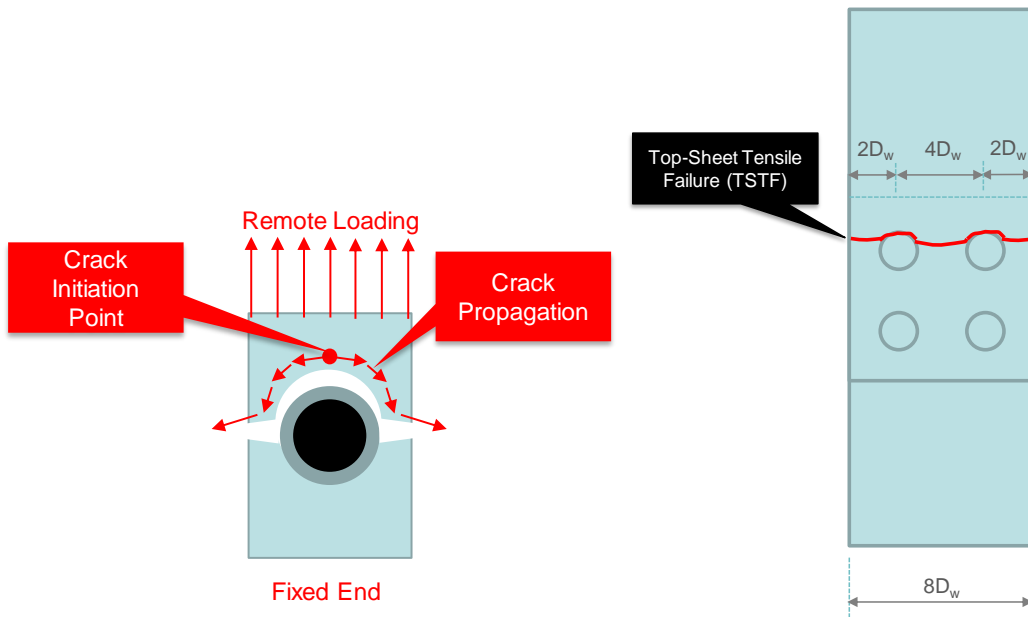


**Fig. 5.12: Top-Sheet Tensile Failure (TSTF) (Left). Crack initiates in TMAZ / HAZ and propagates into the top-sheet parent metal (Right).**

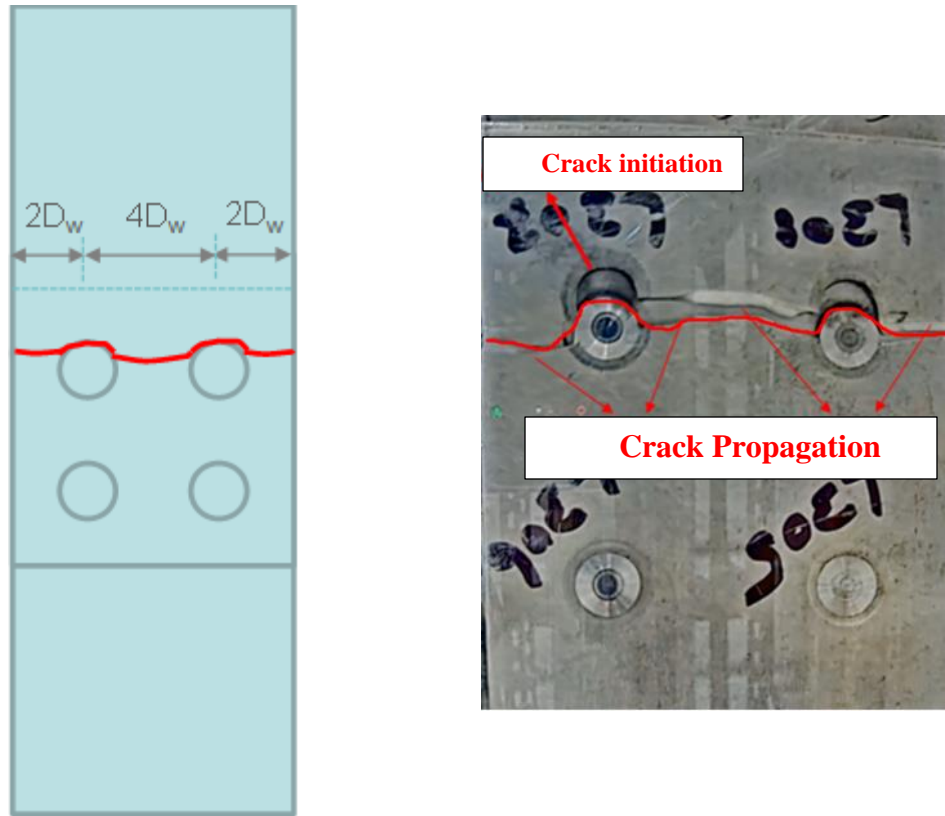


**Fig. 5.13: Crack initiating in TMAZ/HAZ and propagating into the parent metal in a direction that is orthogonal to the loading direction.**

The static test results of four-spot coupons are presented in Table 5.4. All 5 four-spot coupons exclusively demonstrated top-sheet tensile failures. The average ultimate load was 10,575.995 lb. (47,044.369 N). This ultimate load was used for calculating fatigue-test load levels of 35%, 25%, and 15%. The fatigue test results are provided in Table 5.5 and Figure 5.14. Some of the tested four-spot coupons are shown in Figure 5.15 and 5.16.

**Table 5.4: Guided static test results of four-spot coupons per NASM1312-21.**

<b>STATIC TEST</b>			
<b>Coupon #</b>	<b>Failure Load, lb</b>	<b>Failure Load, N</b>	<b>Failure Type</b>
L160-L163	11,016.72	49,004.81	TSTF
L164-L167	10,129.31	45,057.43	TSTF
L168-L171	10,840.43	48,220.64	TSTF
L172-L175	10,257.63	45,628.20	TSTF
L176-L179	10,635.87	47,310.70	TSTF
<b>Average</b>	<b>10,575.99</b>	<b>47,044.35</b>	<b>--</b>

**Table 5.5: Guided fatigue test results of four-spot coupons per NASM1312-21.**

Coupon #	Load Level	R	Frequency	Max load, lbr (N)	Min Load, lbr (N)	Number of Cycles	Failure Type
L100-L103	35%	.1		3,701.59 (16,465.52)	370.16 (1,646.55)	31,827	BSTF
L104-L107						42,360	BSTF
L108-L111						37,306	TSTF
L112-L115						38,892	BSTF
L115-L119						28,694	BSTF
L140-L143	25%			2,643.99 (11,761.09)	264.40 (1,176.11)	145,077	TSTF
L144-L147						63,341	TSTF
L148-L151						107,957	TSTF
L152-L155						92,396	TSTF
L156-L159						84,164	TSTF
L120-L123	15%			1,586.39 (7,056.65)	158.64 (705.67)	271,864	TSTF
L124-L127						446,216	TSTF
L128-L131						297,447	TSTF
L132-L136						359,721	TSTF
L136-L140						295,398	TSTF

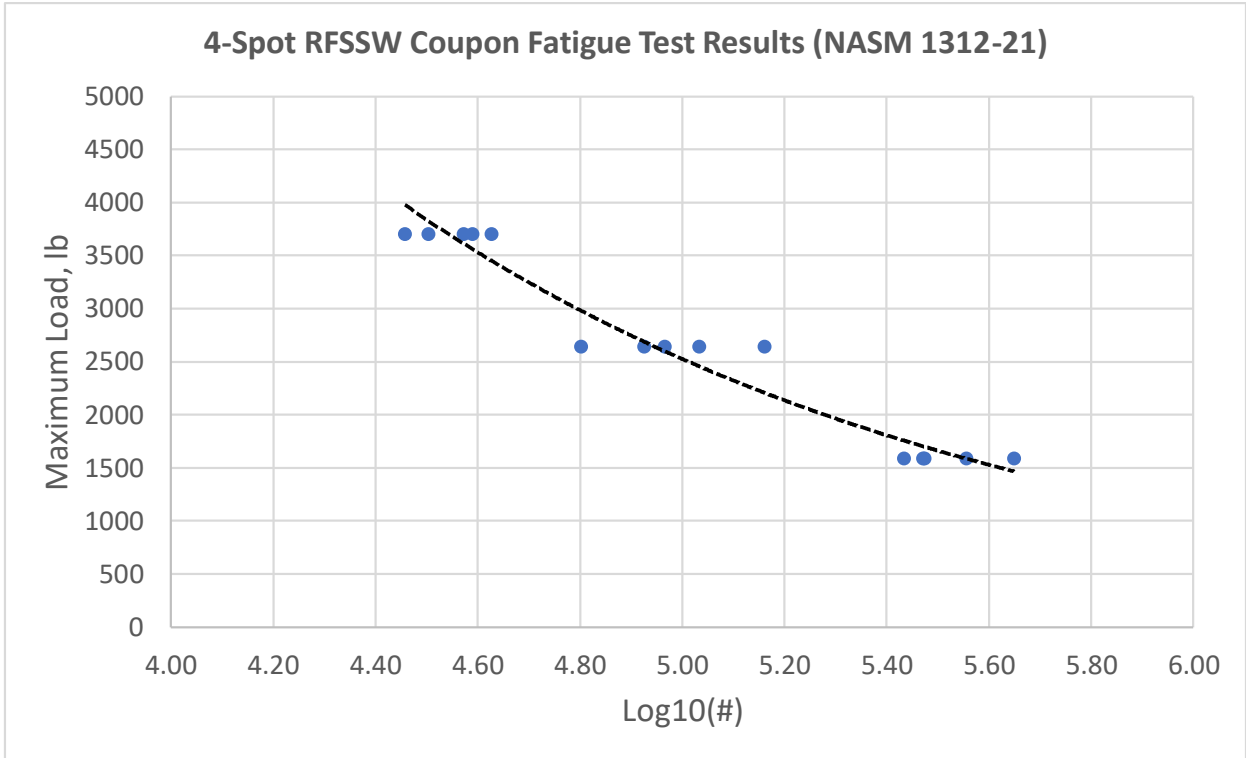


**Fig. 5.14: Guided fatigue test results of four-spot coupons per NASM1312-21.**



**Fig. 5.15: Front and back of Coupon 14.**

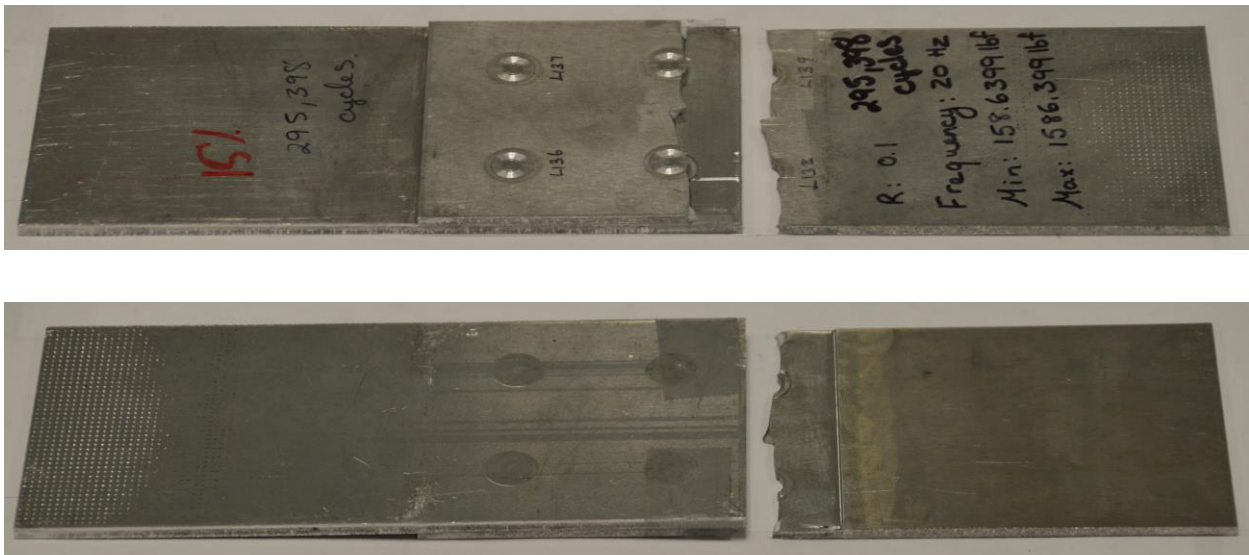


**Fig. 5.16: Front and back of Coupon 15.**

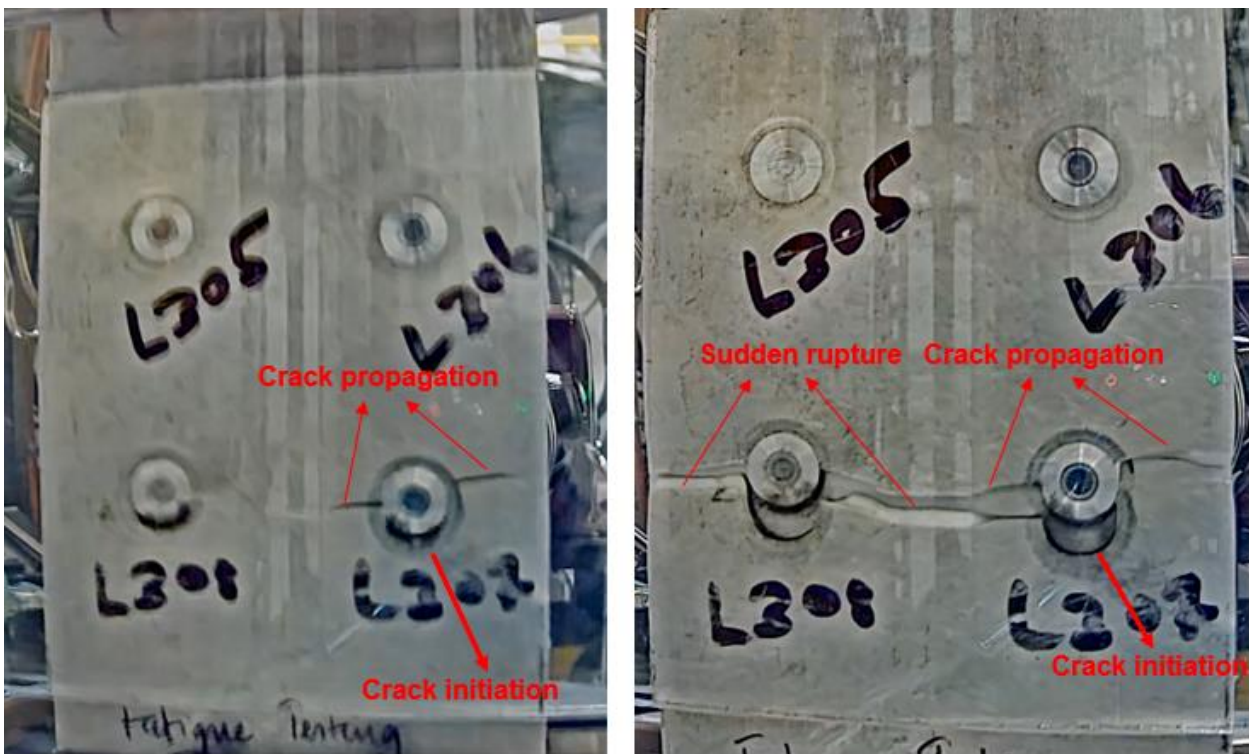


**Fig. 5.17: Crack initiating and propagating through the TMAZ/HAZ in the top sheet (Left). 4 spot coupon after complete failure (Right) (These images were captured during the testing and the vibration caused the blurriness in the images)**

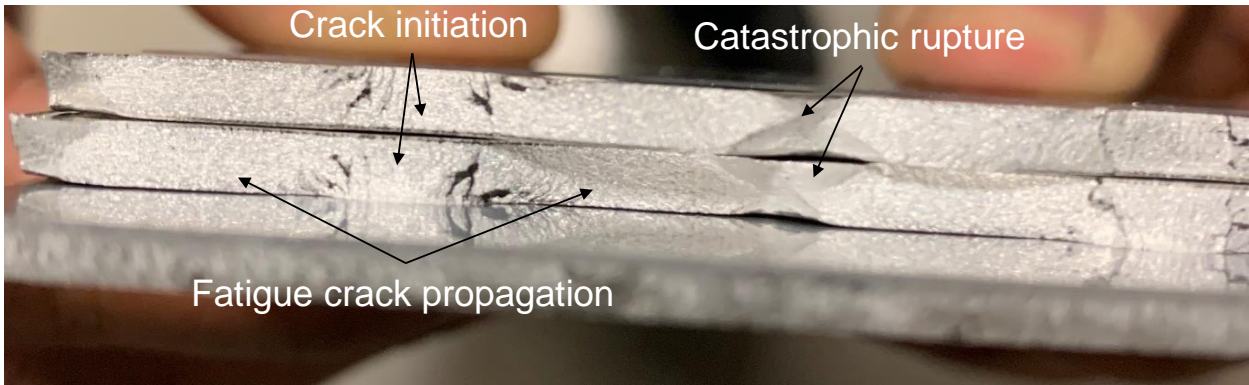


**Fig. 5.18: 4 spot coupon with TSTF (Top); Failure surfaces showing the crack initiation, propagation, and catastrophic rupture (Bottom).**

According to the fatigue test results, 35%-load-level coupons mostly demonstrated BSTF, whereas the lower load level coupons exclusively demonstrated TSTF. To explain why the 35%-load-level coupons mostly demonstrated BSTF, 3 more coupons were produced and tested under high-load level conditions. The coupons were tested at 45% of the load level. The fatigue test results of 45% load level coupons are provided in Table 5.6. All the coupons that were tested at 45% load levels demonstrated top sheet tensile failures. This proves that the fracture mode of coupons tested under high-load levels is similar to the fracture mode of coupons tested under low-load levels. However, during the fatigue tests the cracks propagated at a faster rate in coupons tested under high-load levels compared to coupons tested under low-load levels.

The difference in failure mode that was noticed initially is due to the difference in geometries of the coupons and also due to the different processes involved in producing the coupons. Out of the total 18 coupons, 14 coupons experienced TSTF. The predominance in TSTF is due to the intense plastic deformation that the top sheet experiences during the welding process. As a result of this intense plastic deformation, a much weaker Heat Affected Zone (HAZ) is produced in the top sheet compared to the bottom sheet. Due to the weaker HAZ in the top sheet, the crack initiates

in TMAZ / HAZ and propagates into the top-sheet parent metal at a much faster rate compared to the bottom sheet. This explains why most of the coupons experienced Top Sheet Tensile Failures (TSTF).

**Table 5.6: Guided fatigue test results of 45% load level four-spot coupons**

<b>Coupon #</b>	<b>Load Level</b>	<b>R</b>	<b>Frequency (Hz)</b>	<b>Max Load lbf (N)</b>	<b>Min Load lbf (N)</b>	<b>Number of Cycles</b>	<b>Failure Type</b>
<b>L301-L302</b>	<b>45%</b>	<b>0.1</b>	<b>20 Hz</b>	<b>4759.19</b>	<b>475.91</b>		<b>TSTF</b>
<b>L305-L306</b>						<b>11,630</b>	<b>TSTF</b>
<b>L309-L310</b>						<b>12,601</b>	<b>TSTF</b>

A 25fps camera was used to capture the crack initiation in the coupons. The video was then converted into frames using JPEG converter. The low-resolution frames were further enhanced using an upsampling software Lets Enhance. From the high-resolution images shown in Figure 5.17, the crack was observed to initiate at the boundary between the edge of the welding interface zone and the noninterface zone which is in the Heat Affected Zone (HAZ), and then propagated into the parent metal, orthogonal to the loading direction before the catastrophic rupture of the welded coupons.

By studying the failure surfaces of the 4 spot coupons displayed in Figure 5.18, the crack starts to initiate at the HAZ and starts to propagate into the parent metal before the catastrophic failure of the welded coupons. In Figure 5.18, the HAZ surfaces look shinier than the rest of the surfaces

due to the friction that occurred between the cracked surfaces during the cyclic loading. The catastrophic ruptures shown in Figure 5.18 produced more dull failure surfaces as they are newly created surfaces formed at the end of the fatigue test.

According to (Sutep et al., 2016) In her study, the crack was observed to initiate at the boundary between the edge of the welding interface zone and the noninterface zone which is in the Heat Affected Zone (HAZ). The fatigue crack on the top sheet was found to start at the distal slit and continue to the surface of the sheet up to the concave zone. In addition, the crack initiation sites of all welded joints were the same irrespective of the force amplitude level. [42]

Also, the observations revealed that microstructure near the welded zone hardly affected the fatigue crack initiation and propagation behavior, because the fatigue crack initiated at the slit tip which is located in HAZ regardless of the microstructure [42]

### **Crack Growth Analysis**

In total 12 coupons were produced for the crack growth analysis study. 3 Top sheet parent metal coupons and 3 top sheet welded coupons and 3 bottom sheet parent material coupons and 3 bottom sheet welded coupons. The welded coupons demonstrated top sheet tensile failures and bottom sheet tensile failures during fatigue tests. On the welded coupons, the cracks initiated near the tip of the notch and propagated along the Heat Affected Zone (HAZ) on the top sheet before failing from catastrophic rupture.

- **Top-Sheet Tensile Failure (TSTF)** – TSTF involves a crack initiate in TMAZ / HAZ and propagates into the top-sheet parent metal in a direction that is orthogonal to the loading direction as shown in Figure 5.12.

- **Bottom-Sheet Tensile Failure (BSTF)** – BSTF involves a crack initiate in TMAZ / HAZ and propagates into the bottom-sheet parent metal in a similar way of TSTF.

A 25fps camera was used to capture the crack initiation in the coupons. The video that was captured was converted into frames using JPEG converter. The low-resolution frames were further enhanced using an upsampling software Lets Enhance. The frames were then loaded to the ImageJ software to measure the crack growth on the coupons. Within each high-resolution image, a reference length was utilized to virtualize the crack length into pixels, and a contour was drawn along the crack to determine length based on the total number of pixel connections. These measurements were plotted against the number of cycles to failure to determine the difference in the crack growth rates between the welded and the parent metal coupons and to determine the difference in growth rates between the top sheet and bottom sheet welded coupons. The crack growth vs the number of cycles to failure of the top sheet coupons is shown in Figure 5.19. The Crack growth vs the number of cycles to failure of the bottom sheet coupons is shown in Figure 5.20. The comparison between the top sheet and the bottom sheet performance is shown in Figure 5.21

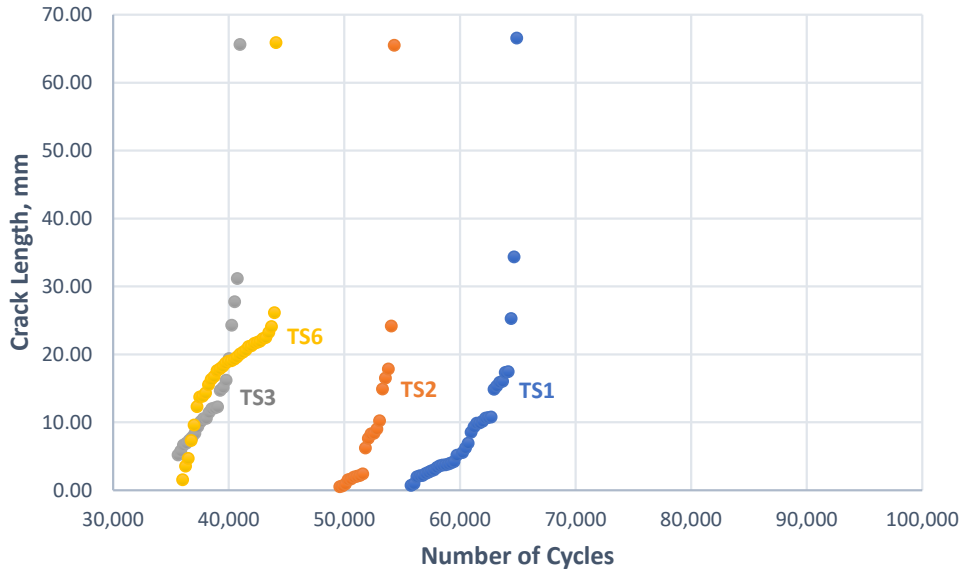


**Fig. 5.19: Crack growth vs the number of cycles to failure of the top sheet coupons.**

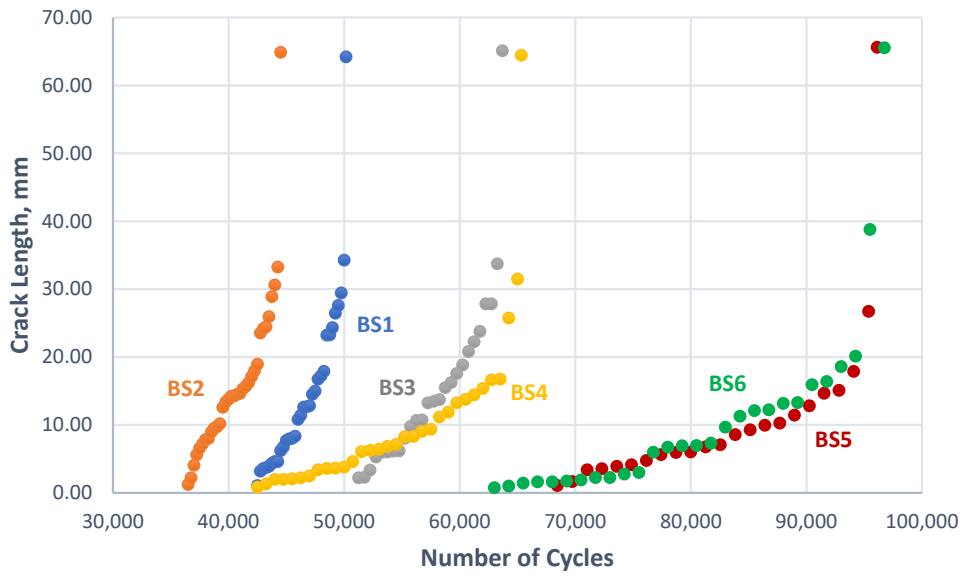


**Fig. 5.20: Crack growth vs the number of cycles to failure of the bottom sheet coupons.**

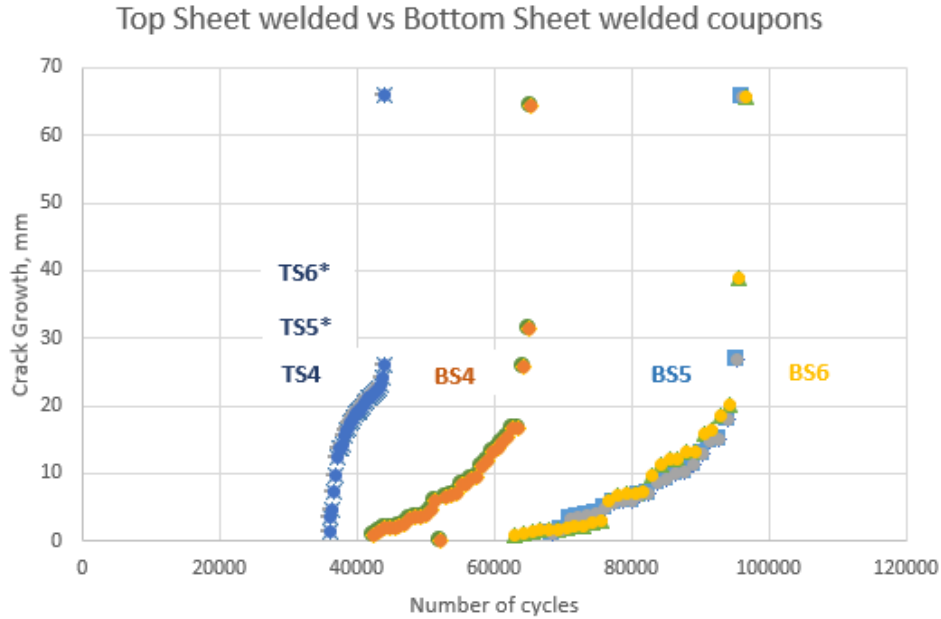


**Fig. 5.21: Crack growth vs the number of cycles to failure (top sheet vs bottom sheet). \* - TS5 and TS6 demonstrated results similar to that of TS4.**

*Crack Growth Rate Calculation:*

The stress intensity factor  $K$  defines the magnitude of the local stresses around the crack tip. This factor depends on the load, crack size, crack shape, and geometry. The equation is given by [43]

$$K = \sigma \sqrt{\pi a} f(a/W) \tag{1}$$

where:

$\sigma$  = applied (remote) stress

$a$  = crack length

$W$  = specimen width

$F(a/W)$  = correction factor that depends on specimen and crack geometry

For example, the stress intensity factor for an edge crack in a semi-infinite body is as follows:

$$KI=1.12 \sigma \sqrt{\pi a} \quad (2)$$

During (cyclic) loading of metals **the yield stress exceeds near the crack tip and as a result a plastic zone develops due to the plastic strains near that region.** The shape and size of the plastic zone are not exactly defined. According to Irwin [44], the monotonic plastic zone size,  $2r_p^m$ , at a stress intensity factor  $K$ , is calculated using:

$$2r_p^m = 1/\pi (K/\sigma_{ys})^2 \quad (3)$$

where:

$\sigma_{ys}$  is the yield strength.

The plastic zone is assumed to be circular in the cross- section. During the decreasing part of the loading cycle the nominal tensile load reduces, i.e., the stress intensity reduces from  $K_{max}$  to  $K_{min}$  and the plastic region near the crack tip is put into compression by the surrounding elastic body. A reversed plastic zone develops near that region due to this compression. This reversed or cyclic plastic zone size,  $2r_p^c$ , depends on the magnitude of  $\Delta K$  and twice the yield strength [43]:

$$2r_p^c = 1/\pi (\Delta K/\sigma_{ys})^2 \quad (4)$$

If there is a crack that can grow, life is determined by the crack growth rate. The rate at which a crack grows is determined from the crack size 'a' as a function of the number of cycles elapsed 'N'. The ASTM E 647 recommends two approaches: the secant or the incremental

polynomial method. The secant method is mainly used in this work to calculate the fatigue crack growth rate from a-N data [49]

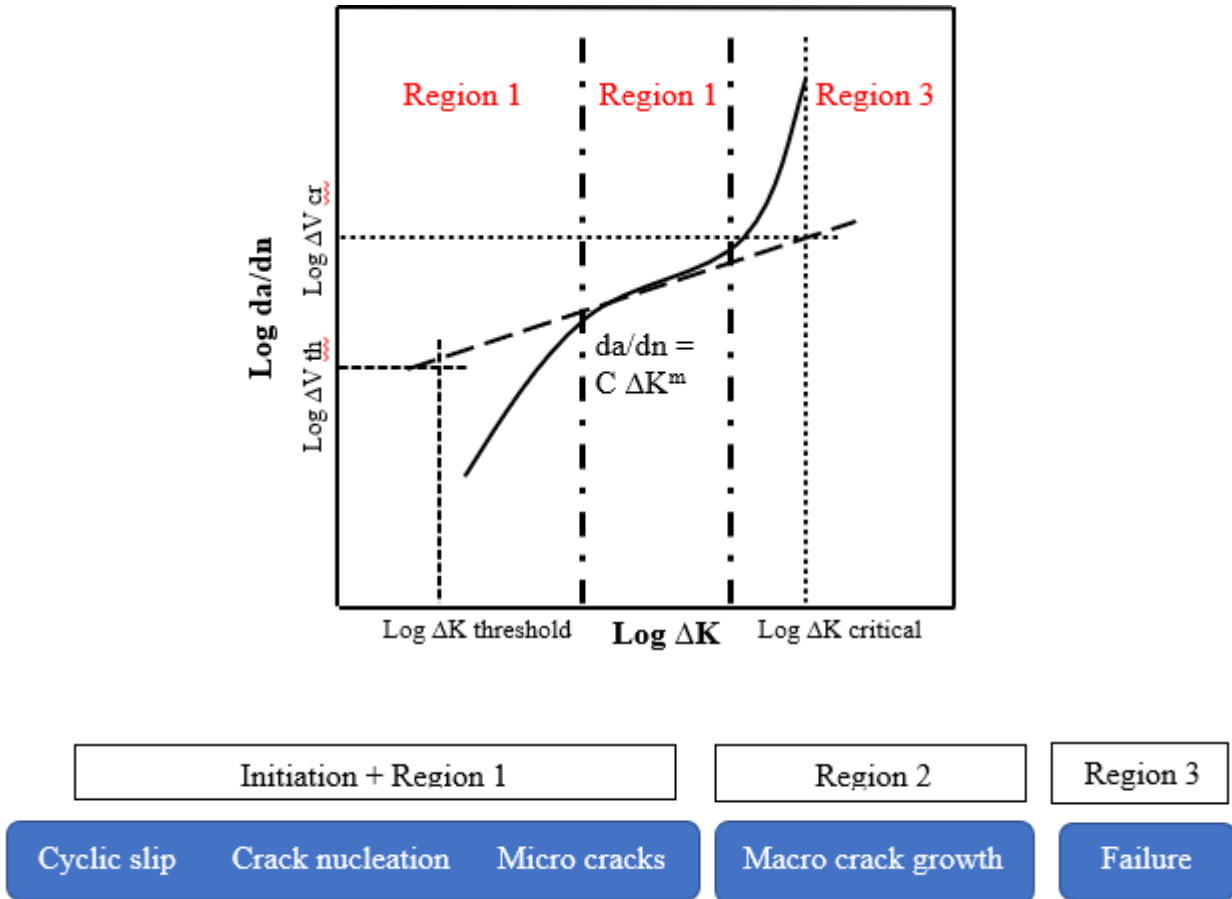


**Figure 5.22: Crack growth phases.**

*Crack Growth Threshold:*

Compressive stresses are generated during crack closing, so there is a threshold needed to make the crack grow. This happens during the decreasing part of the loading cycle where the stress intensity reduces from  $K_{\max}$  to  $K_{\min}$ .  $\Delta K$  threshold is given by,

$$\Delta K_{th} = K_{opening} - K_{min} \quad (5)$$

Where:

$K_{opening}$  = critical value to make the crack open

$K_{min}$  = minimum stress intensity factor

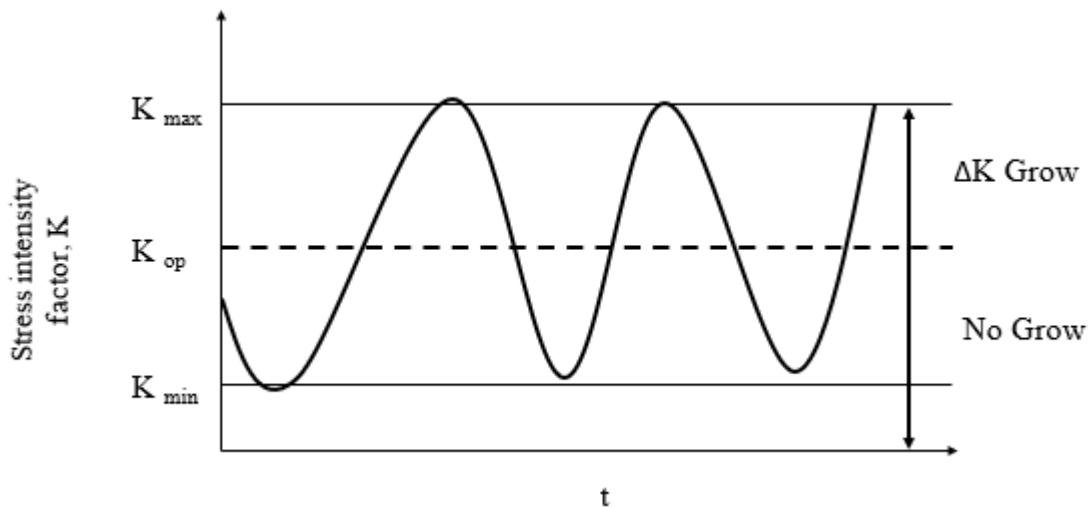


**Figure 5.23: Cyclic stress intensity factor.**

In figure 5.23, the stress intensity factor varies between maximum and minimum values during loading and unloading cycles. The crack starts to grow when the stress intensity factor is higher than the  $K_{\text{opening}}$ . However, the crack doesn't grow between  $K_{\text{min}}$  and  $K_{\text{opening}}$ .

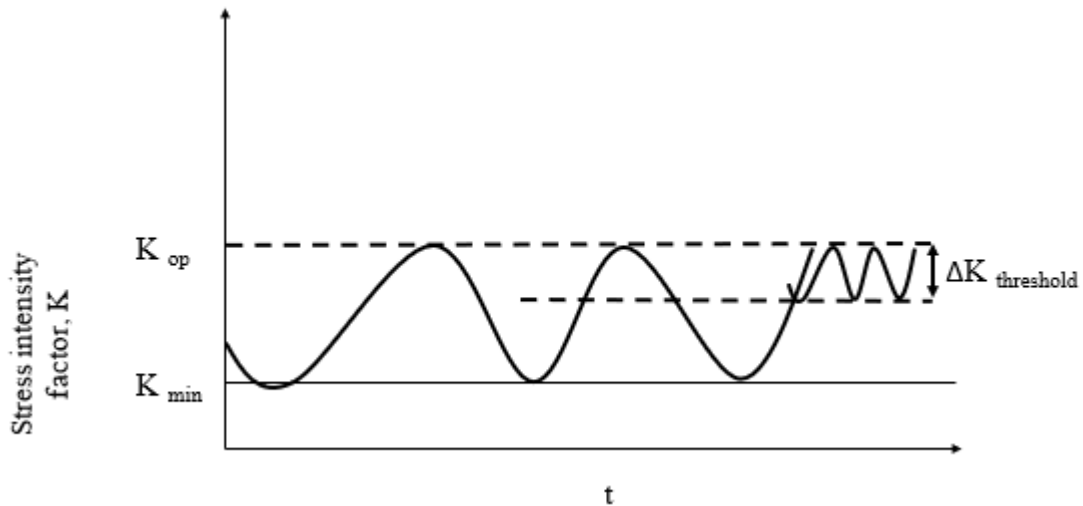


**Figure 5.24: Cyclic stress intensity factor explaining  $\Delta K_{\text{threshold}}$**

Figure 5.24 explains the condition when Stress intensity 'K' does not exceed  $K_{\text{opening}}$ . For a particular  $K_{\text{min}}$  there is a  $\Delta K_{\text{threshold}}$  that must be exceeded before the crack starts to grow. From the figure above, it is understood that the  $\Delta K_{\text{threshold}}$  value depends on the mean stress relative to the value of  $K_{\text{opening}}$ .

In conclusion, if  $\Delta K > \Delta K_{\text{threshold}}$ , there will be crack growth in every cycle. The rate at which the crack grows depends on the part that exceeds  $K_{\text{opening}}$ . It is also important to note that, since  $\Delta K$  is a function of crack length i.e.,  $\Delta K$  increases as the crack grows in size irrelevant of the loading condition.

*Secant Technique:*

Using the secant technique, the crack growth rate is determined by calculating the slope of the straight line connecting two adjacent data points on the a-N curve. It is more formally expressed as follows:

$$(da/dN) = (a_{i+1} - a_i) / (N_{i+1} - N_i) \quad (6)$$

Since the computed da/dN is an average rate over the  $(a_{i+1} - a_i)$  increment, the average crack size,  $\bar{a} = \frac{1}{2} (a_{i+1} + a_i)$ , is normally used to calculate  $\Delta K$ . The secant method often results in an increased scatter in da/dN [45, 46].

Stress intensity 'K' is not well defined close to the plate edges. For this reason, the effects due to the presence of a starter notch is avoided and crack length values obtained close to the plate edges are rejected for calculation [49].

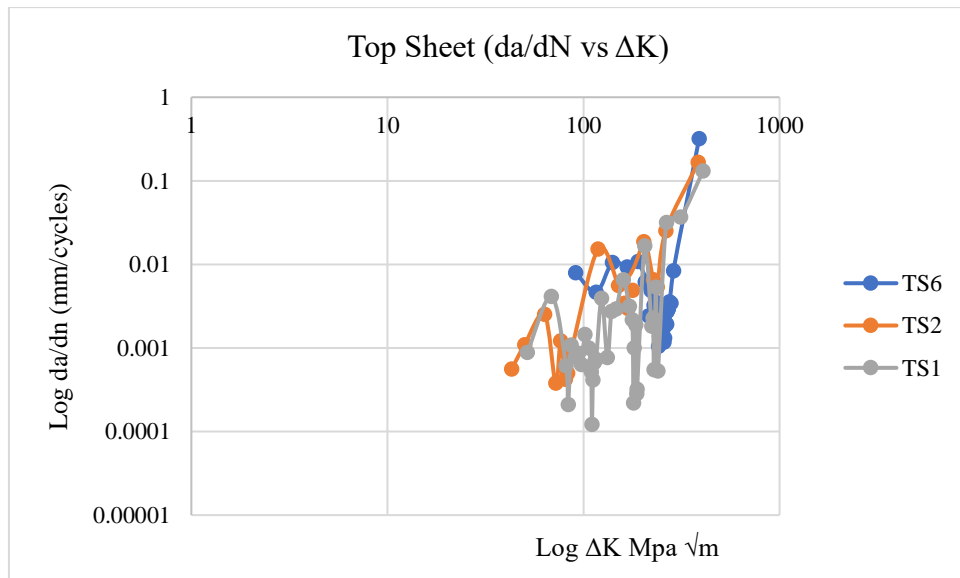


**Figure 5.25: Crack growth rate vs the stress intensity factor (Top sheet welded coupons)**

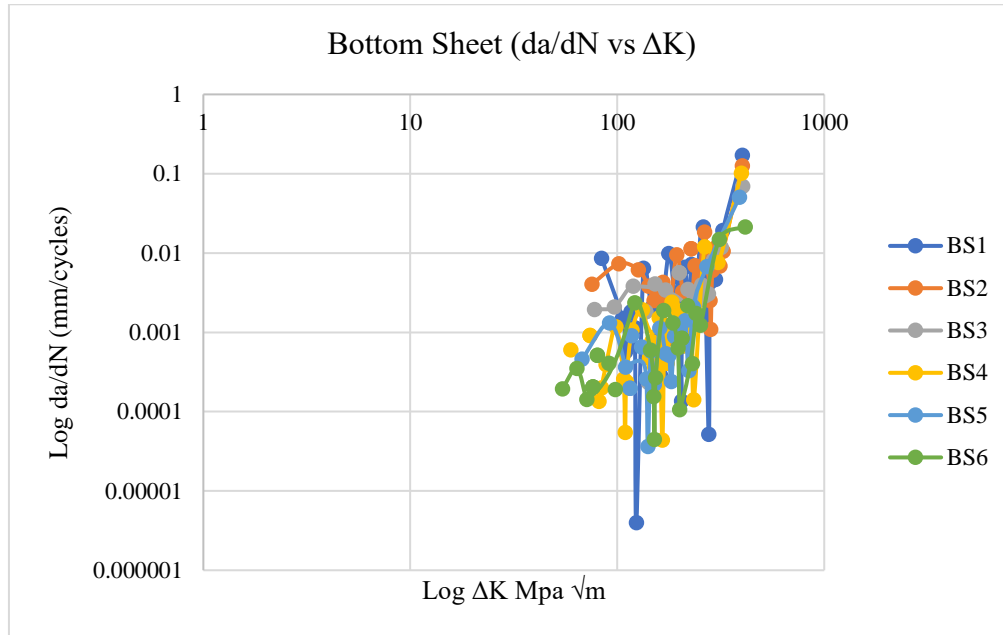


**Figure 5.26: Crack growth rate vs the stress intensity factor (Bottom sheet welded coupons)**

*Exponential Method:*

Based on the concept of exponential nature of crack growth, the crack length vs. number of cycles data have been fitted by an exponential equation of the form [48]

$$a_j = a_i e^{m_{ij} (N_j - N_i)} \quad (7)$$

where,  $a_i$  and  $a^j$  = crack length in  $i^{\text{th}}$  step and  $j^{\text{th}}$  step in 'mm' respectively,

$N_i$  and  $N_j$  = No. of cycles in  $i^{\text{th}}$  step and  $j^{\text{th}}$  step respectively,

$m_{ij}$  = specific growth rate in the interval  $i$ - $j$ ,

$i$  = No. of experimental steps, and  $j = i+1$ .

Table 5.1 explains the procedures of the exponential method. (Since fatigue test data are very large in number, only a small part of data is presented in Table 5.7 for the purpose of explaining the procedure of smoothening the a–N curve):

- The exponent ‘ $m_{ij}$ ’ (i.e., specific growth rate) is the important controlling parameter in the proposed exponential equation. The specific growth rate  $m$  is not a constant quantity. It depends on a number of factors [48]. The specific growth rate ‘ $m_{ij}$ ’ is derived by taking logarithm of equation (7) as follows:

$$m_{ij} = \frac{\ln\left(\frac{a_j}{a_i}\right)}{(N_j - N_i)} \quad (8)$$

- The raw values of specific growth rate ( $m$ ) are calculated using eq (8) from experimental a–N data (columns A and B, Table 5.7). The specific growth rate values  $m_{ij}$  are given in column C of Table 5.7.
- To get a better result, the crack length is incremented by 0.005 mm. The incremented crack length values are tabulated in column D and the corresponding values of specific crack growth rate  $m_{ij}$  are obtained using the polynomial equation (column E).
- The above values of specific crack growth rates are used to calculate the smoothened values of the number of cycles (column F, Table 5.7) using the equation given below:

$$N_j = \frac{\ln\left(\frac{a_j}{a_i}\right)}{m_{ij}} + N_i \quad (9)$$

- The crack growth rates ( $da/dN$ ) are calculated directly from the above calculated ‘ $N$ ’ values. The equation to determine the crack growth rate is given below:

$$(da/dN) = (a_{i+1} - a_i) / (N_{i+1} - N_i) \quad (10)$$

**Table 5.7: Comparison of experimental and smoothed sets of fatigue growth data**

<b>crack growth (mm)</b>	<b>Number of cycles (Exp)</b>	<b>Specific crack growth rate, <math>m_{ij}</math></b>	<b>Crack length incremented by .005 mm (mm)</b>	<b>Sp. Crack growth rate <math>m_{ij}</math> (Polynomial equation)</b>	<b># of cycles calculated from equation</b>
0.70	55775	0.0011	0.705	0.0293	55784
0.92	56022	0.0030	0.923	0.0292	56047
1.94	56269	0.0003	1.944	0.0287	56271
2.09	56515	0.0001	2.095	0.0287	56516
2.14	56762	0.0005	2.147	0.0286	56766
2.41	57009	0.0003	2.413	0.0285	57012
2.60	57256	0.0003	2.605	0.0284	57259
2.81	57503	0.0002	2.818	0.0283	57505
2.97	57750	0.0005	2.974	0.0282	57754
3.33	57997	0.0003	3.330	0.0281	57999
3.57	58244	0.0001	3.576	0.0279	58245
3.70	58491	0.0000	3.703	0.0279	58491
3.73	58738	0.0001	3.733	0.0279	58738
3.83	58984	0.0002	3.835	0.0278	58986
3.99	59231	0.0002	3.999	0.0277	59233
4.17	59478	0.0008	4.178	0.0276	59486
5.14	59725	0.0001	5.143	0.0272	59728

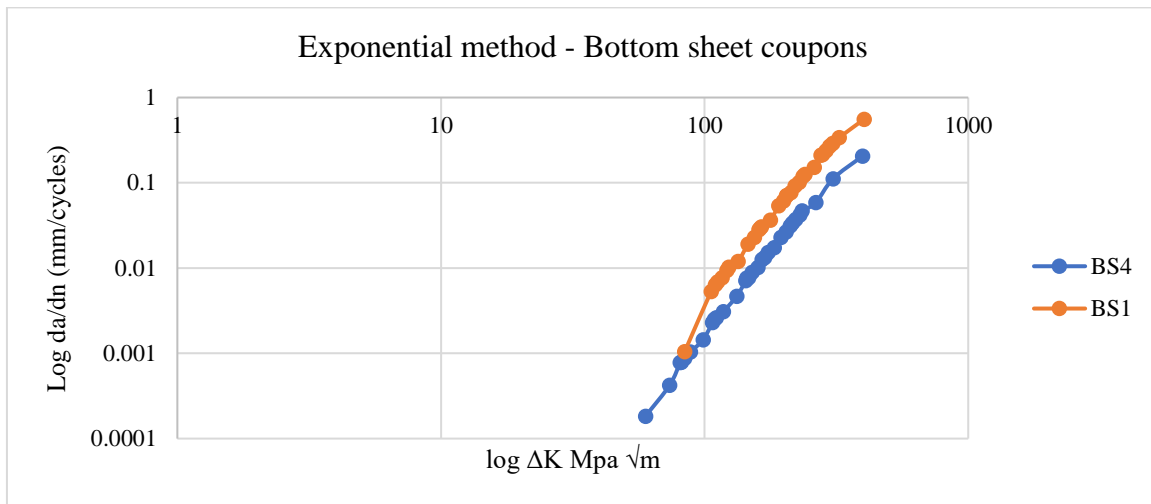
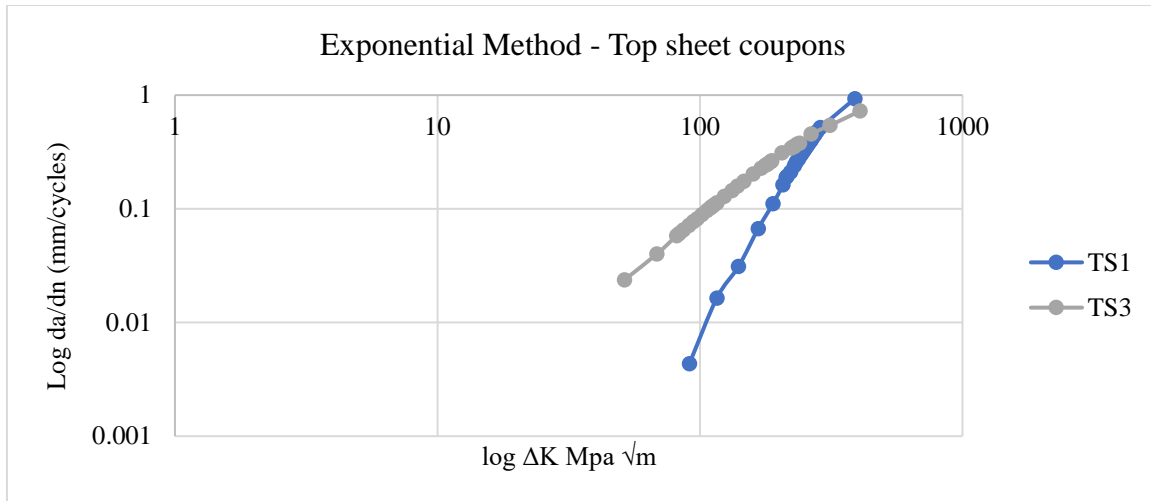


**Figure 5.27: Crack growth rate vs the stress intensity factor of top sheet welded coupons (Top) and Bottom sheet welded coupons (Bottom)**

## DISCUSSION

Figure 5.28 shows the relationship between the crack growth rate and the cyclic stress intensity factor. There is no crack growth until the  $\Delta K$  threshold is reached. At  $\Delta k_{\text{threshold}}$ , the maximum stress intensity factor is equal to the critical value that is needed to open up a crack ( $K_{\text{opening}}$ ). During Stage I, when the stress intensity factor reaches the threshold, the crack growth rate is very fast and then starts to slow down. The stage II region, also called as the steady state crack growth

region is where the crack grows at a steady rate. The region III is where the crack starts to grow very fast. At this region the maximum stress intensity factor is equal to the fracture toughness of the material ( $K_{max} = K_{Ic}$ ).

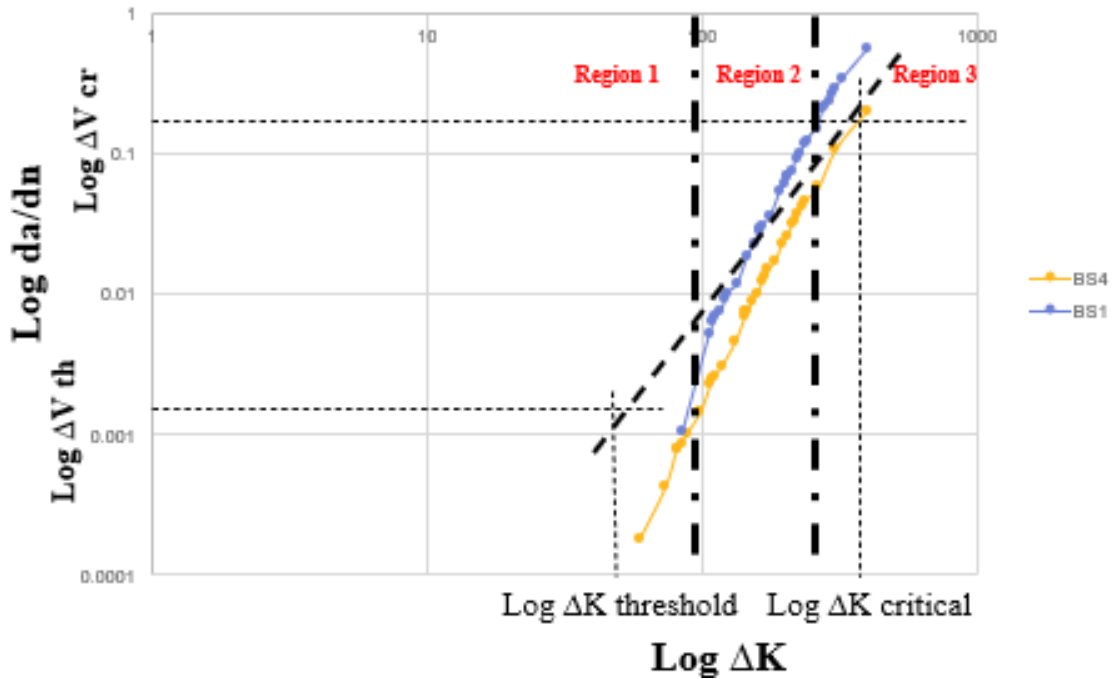


**Figure 5.28: Relationship between the crack growth rate and the cyclic stress intensity factor**

Several methods are used to determine crack growth rate from raw experimental a–N data as already highlighted. Every method has its own merits and demerits. In this study, Secant technique and exponential methods were used in calculating the crack growth rate. The secant method often results in an increased scatter in da/dN. The crack growth rate (da/dN) values obtained by sequential method gives a much smoother curve compared to the secant technique. It is also assumed that errors in crack length are due to random noises and errors in the measurement process. Large number of a–N data can be used to minimize the random error.

From the crack growth analysis results, the fatigue performance of the bottom sheet welded coupons was significantly better than the parent metal coupons and the top sheet welded coupons. The welding process improved the ductility of the bottom sheet. RFSSW process produces considerable grain refinement and recrystallization in the welded coupons. There have been several studies that have investigated the effects of grain size on fatigue crack growth resistance and the occurrence of crack arrest at grain boundaries [50-51]. Grain boundaries can act as barriers and can decrease the fatigue crack growth rate. Grain refinement can also lead to increased fatigue limits [47]. However, the poor performance of the top sheet welded coupons is due to the welding taking place directly on the top sheet side. This induces more heat and as a result, the top sheet is susceptible to intense plastic deformation. Hence, a much weaker Thermomechanically Heat Affected Zone/Heat Affected Zone (TMAZ/HAZ) is produced in the top sheet welded coupons. Also, the mechanical stirring might have altered the material properties of the top sheet aluminum alloy, which could have added to the poor performance of the top sheet welded coupons. The failure surfaces of top sheet parent metal coupon is shown in Fig 5.30. The failure surfaces of top sheet welded coupon is shown in Fig 5.32. Fig. 5.34 depicts the failure surfaces of bottom sheet parent metal coupon. And Fig. 5.36 shows the failure surfaces of bottom sheet welded coupon. According to Figures 5.20, 5.31, 5.33, 5.35 the crack initiates near the notch and starts to propagate through the HAZ. The crack propagates through the HAZ until the coupons completely fail from catastrophic rupture.



**Fig. 5.29: Crack propagating through the top sheet parent metal coupon (Left). Top sheet parent metal after failure (Right) (These images were captured during the testing and the vibration caused the blurriness in the images)**

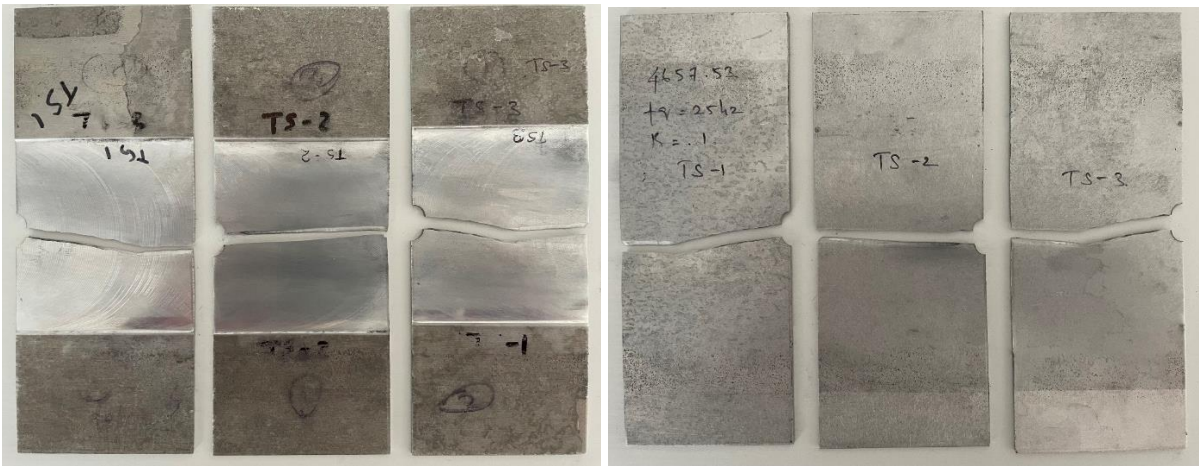


**Fig. 5.30: Front and back of the failure surfaces of top sheet parent metal coupon.**

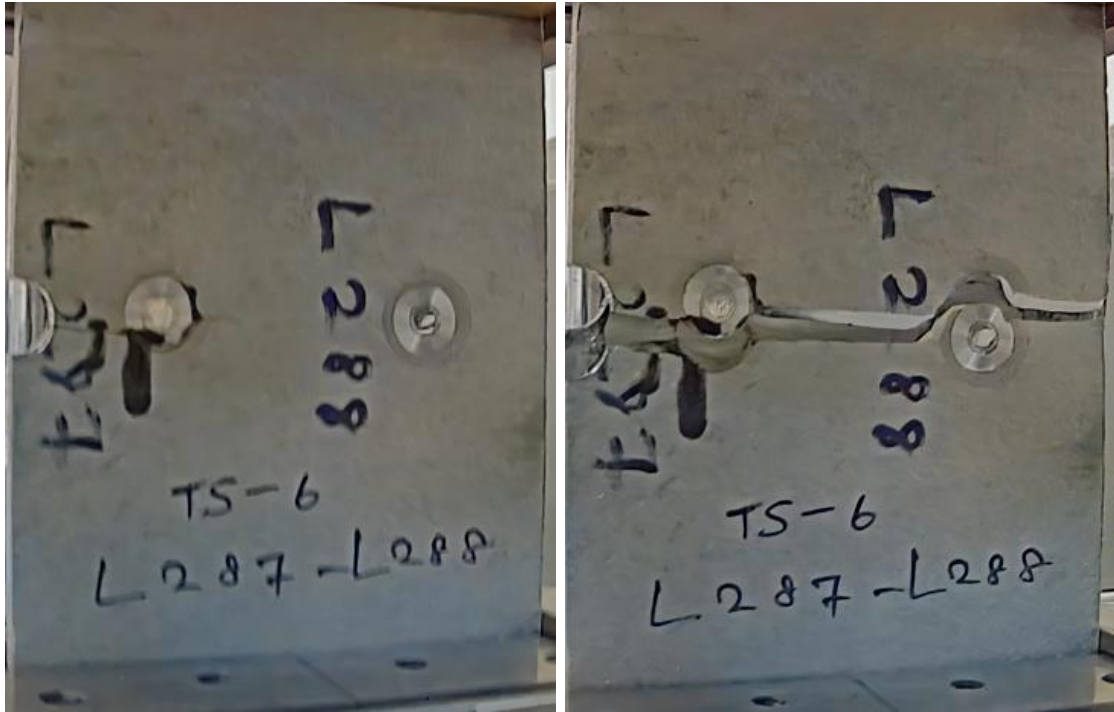


**Fig. 5.31: Crack propagating through the HAZ in the top sheet welded coupon (Left). Top sheet parent welded coupon after complete rupture (Right) (These images were captured during the testing and the vibration caused the blurriness in the images)**



**Fig. 5.32: Front and back of the failure surfaces of top sheet welded coupon.**

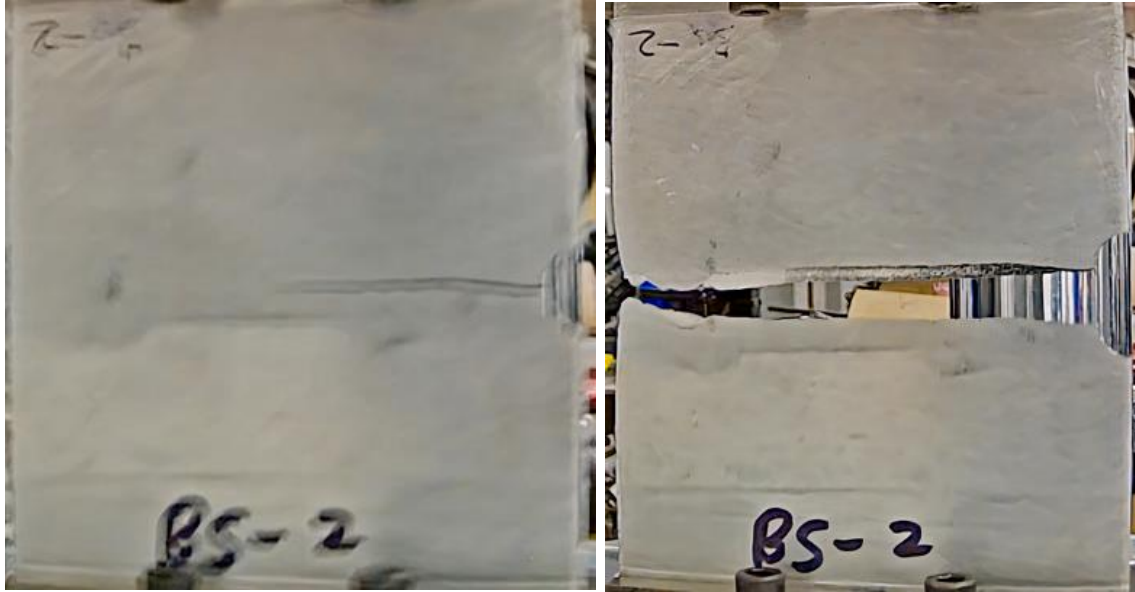


**Fig. 5.33: Crack propagating through the Bottom sheet parent metal coupon (Left). Bottom sheet parent metal after failure (Right) (These images were captured during the testing and the vibration caused the blurriness in the images)**



**Fig. 5.34: Front and back of the failure surfaces of bottom sheet parent metal coupon.**

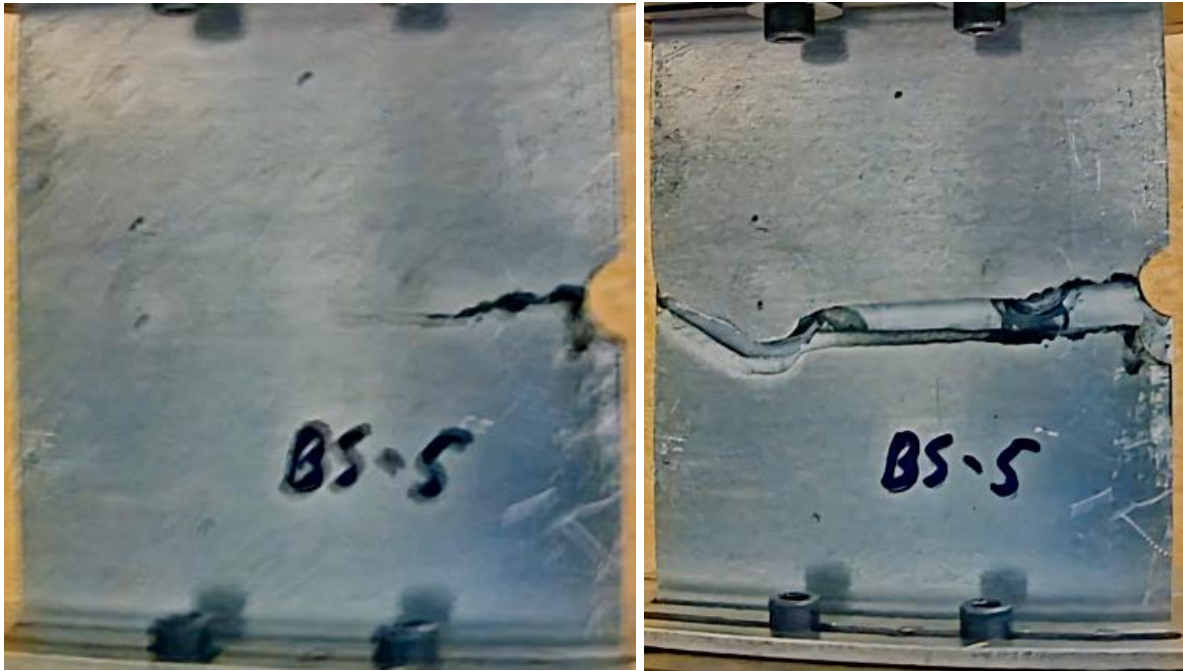


**Fig. 5.35: Crack propagating through the HAZ in the bottom sheet welded coupon (Left). Bottom sheet parent welded coupon after complete rupture (Right) (These images were captured during the testing and the vibration caused the blurriness in the images)**

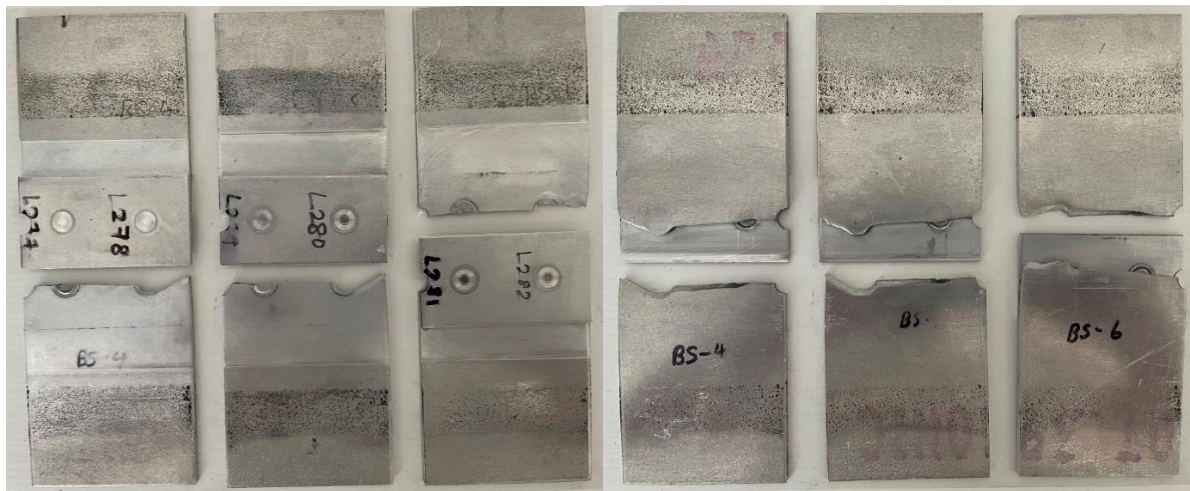


**Fig. 5.36: Front and back of the failure surfaces of bottom sheet welded coupon.**

## **SUMMARY**

The objective of the fatigue study is to investigate fatigue performances of RFSSW with the use of an existing aerospace standard so that the fatigue performances of RFSSW can be compared with existing joining technologies, such as mechanical fastening, resistance spot welding, etc. The results of this study will also be instrumental to advance the RFSSW process to Technology Readiness Level (TRL) 6.

To evaluate the fatigue performances for welding 6013-T6 to 2029-T8 with a 9mm tool, an RFSSW process was developed with the use of a Design-of-Experiments (DoE) method. The DoE method considered three weld parameters, which are the plunge depth, probe speed, and spindle speed of the weld tool, as the DoE factors. The response variable of the DoE method was the ultimate lap-shear load (failure load) of a single spot straight coupon. The weld parameters optimized by the DoE method were used for producing fatigue test coupons with the 9mm tool.

According to the fatigue test results, 35%-load-level coupons mostly demonstrated BSTF, whereas the lower load level coupons exclusively demonstrated TSTF. To explain why the 35%-load-level coupons mostly demonstrated BSTF, 3 more coupons were produced. These coupons were tested at 45% load level. All the coupons that were tested at 45% load levels demonstrated top sheet tensile failures. This proves that the fracture mode of coupons tested under high-load level is similar to the fracture mode of coupons tested under low-load levels. However, the crack propagated at a faster rate in coupons tested under high-load levels compared to coupons tested under low-load levels.

From the high resolution images shown in Figure 5.17, the crack was observed to initiate at the boundary between the edge of the welding interface zone and the noninterface zone which is located in the Heat Affected Zone (HAZ). The failure surfaces of BSTF are displayed in Figure

5.18. According to Figure 4.18, HAZ surfaces look shinier than the rest of the surfaces. The shinier surfaces mean more friction occurred between the cracked surfaces during the cyclic loading. The surface friction, like rubbing makes the surfaces shinier under the cyclic loading. The catastrophic ruptures shown in Figure 5.18 produced more dull failure surfaces as they are newly created surfaces formed at the end of the fatigue test.

In this study, the secant technique and exponential methods were used in calculating the crack growth rate. The secant method often results in an increased scatter in  $da/dN$ . The crack growth rate ( $da/dN$ ) values obtained by sequential method gives a much smoother curve compared to the secant technique. It is also assumed that errors in crack length are due to random noises and errors in the measurement process. Many a-N data points can be used to minimize the random error.

From the crack growth analysis results, the fatigue performance of the bottom sheet welded coupons was significantly better than the parent metal coupons and the top sheet welded coupons. The welding process improved the ductility of the bottom sheet. RFSSW process produced considerable grain refinement and recrystallization in the welded coupons. However, the poor performance of the top sheet welded coupons is due to the welding taking place directly on the top sheet side. This induces more heat and as a result, the top sheet is susceptible to intense plastic deformation. Hence, a much weaker Thermomechanically Heat Affected Zone / Heat Affected Zone (TMAZ/HAZ) is produced in the top sheet welded coupons. Also, the mechanical stirring might have altered the material properties of the top sheet aluminum alloy, which could have added to the poor performance of the top sheet welded coupons.

## REFERENCES

## REFERENCES

1. Ibrahim IJ, Yapici GG (2018) Application of a novel friction stir spot welding process on dissimilar aluminum joints. *Journal of Manufacturing Processes*, 1:35, pp. 282-8.
2. Mehta KP, Badheka VJ. A review on dissimilar friction stir welding of copper to aluminum: process, properties, and variants. *Mater Manuf. Proc.*, 2016;31:233–54.
3. Sakano, R. (2004). Development of spot FSW robot system for automobile body members. In *Proceedings of the 3rd International Symposium of Friction Stir Welding*, Kobe, Japan, 2004.
4. Iwashita, T. (2003). U.S. Patent No. 6,601,751. Washington, DC: U.S. Patent and Trademark Office.
5. Thomas, W. M. (1991). NE; Needham, JC; Nurch, MG; Temple-Smith, P.; Dawes, C. *Friction Stir Butt Welding*. GB.
6. Schilling, C., Dos Santos, J. (2004), “Method and Device for Joining at Least Two Adjoining Work Pieces by Friction Welding,” U.S. Patent No. 6,722,556, April 20.
7. Okada, H., Kamimuki, K., & Fujimoto, M. (2013). Assembly Study of Refill FSSW. *SAE International Journal of Aerospace*,6(1), 299-304. doi:10.4271/2013-01-2310
8. Okada H, Kamimuki K, Yoshikawa S, Fukada S. Refill friction spot joining for aerospace application. *SAE Technical Paper 2015*. 2015-01-2614.
9. E. Boldsaikhan, S. Fukada, M. Fujimoto, K. Kamimuki, H. Okada, B. Duncan, et al, “Refill friction stir joining for aerospace aluminum alloys,” *Friction Stir Welding and Processing IX*, pp. 237-246, ed. Y. Hovanski, R. Mishra et al, Springer Cham, 2017
10. Schmal, C., Meschut, G., & Buhl, N. (2019). Joining of high strength aluminum alloys by refill friction stir spot welding (III-1854-18). *Welding in the World*,63(2), 541-550. doi:10.1007/s40194-018-00690-0
11. Okada, H., Kamimuki, K., & Fujimoto, M. (2013). Assembly study of refill FSSW. *SAE International Journal of Aerospace*, 6(2013-01-2310), 299-304.

12. R.W. Fonda and J.F. Bingert, Micro-structural Evolution in the Heat-Affected Zone of a Friction Stir Weld, *Metallurgical and Materials Transactions*, Volume 35A, May 2004-1487.
13. Paglia, C. S., & Buchheit, R. G. (2008). A look in the corrosion of aluminum alloy friction stir welds. *Scripta Materialia*, 58(5), 383-387.
14. Saad Ahmed Khodir and Toshiya Shibayanagi, Friction stir welding of dissimilar AA2024 and AA7075 aluminum alloys, *Material Science and Engineering*, B 148 (2008) 82–87.
15. Zhao YQ, Liu HJ, Chen SX, Lin Z, Hou JC (2014) Effects of sleeve plunge depth on microstructures and mechanical properties of friction spot welded alclad 7B04-T74 aluminum alloy. *Materials & Design* (1980-2015), 1(62), pp. 40-6.
16. Arul, S. G., Miller, S. F., Kruger, G. H., Pan, T. Y., Mallick, P. K., & Shih, A. J. (2008). Experimental study of joint performance in spot friction welding of 6111-T4 aluminium alloy. *Science and Technology of welding and joining*, 13(7), 629-637.
17. Freeney, T. A., Sharma, S. R., & Mishra, R. S. (2006). Effect of Welding Parameters on Properties of 5052 Al Friction Stir Spot Welds. SAE Technical Paper Series. doi:10.4271/2006-01-0969
18. Tozaki, Y., Uematsu, Y., & Tokaji, K. (2007). Effect of processing parameters on static strength of dissimilar friction stir spot welds between different aluminium alloys. *Fatigue & Fracture of Engineering Materials & Structures*, 30(2), 143-148.
19. Tran, V. X., Pan, J., & Pan, T. (2009). Effects of processing time on strengths and failure modes of dissimilar spot friction welds between aluminum 5754-O and 7075-T6 sheets. *Journal of materials processing technology*, 209(8), 3724-3739.
20. Badarinarayan, H., Yang, Q., & Zhu, S. (2009). Effect of tool geometry on static strength of friction stir spot-welded aluminum alloy. *International Journal of Machine Tools and Manufacture*, 49(2), 142-148
21. Mitlin, D., Radmilovic, V., Pan, T., Chen, J., Feng, Z., & Santella, M. L. (2006). Structure–properties relations in spot friction welded (also known as friction stir spot welded) 6111 aluminum. *Materials Science and Engineering: A*, 441(1-2), 79-96.
22. Su, P., Gerlich, A., & North, T. H. (2005). Friction stir spot welding of aluminum and magnesium alloy sheets (No. 2005-01-1255). SAE Technical Paper.

23. Boldsaikhan, E., Fujimoto, M., Kamimuki, K., Okada, H., Duncan, B., Bui, P., ... & Handyside, A. (2016). Refill Friction Stir Spot Joining Rivet Replacement Technology (No. 2016-01-2130). SAE Technical Paper.
24. Montgomery, D.C., Design and Analysis of Experiments, 6<sup>th</sup> edition, John Wiley & Sons, 2005.
25. *MMPDS-14 Metallic Materials Properties Development and Standardization (MMPDS) Handbook*; Battelle Memorial Institute: Columbus, OH, USA, 2020.
26. Rosario, G.F.J. Static Test Simulation of Refill Friction Stir Spot Welded and Riveted Coupons Using Finite Element Analysis. Master's Thesis, Wichita State University, Wichita, KS, USA, December 2019.
27. Ravichandran, S.P. Comparison of Refill Friction Stir Spot Welding versus Riveting in Aircraft Applications. Master's Thesis, Wichita State University, Wichita, KS, USA, July 2019.
28. Material Property Data. Available online: <http://www.matweb.com/> (accessed on 30 August 2021).
29. Aerospace Industries Association. *NASM1312-4 Fastener Test Methods, Method 4, Lap Joint Shear*; Aerospace Industries Association: Washington, DC, USA, 1997.
30. Boldsaikhan, E.; Fukada, S.; Fujimoto, M.; Kamimuki, K.; Okada, H.; Duncan, B.; Bui, P.; Yeshiambel, M.; Brown, B.; Handyside, B. *Refill Friction Stir Spot Welding Rivet Replacement Technology*; SAE Tech. Paper No. 2016-01-2130; SAE International: Warrendale, PA, USA, 2016.
31. *ISO-14272:2016 Resistance Welding—Destructive Testing of Welds—Specimen Dimensions and Procedure for Cross Tension Testing of Resistance Spot and Embossed Projection Welds*; International Organization for Standardization: Geneva, Switzerland, 2016.
32. *NASM1312-21 Fastener Test Methods, Method 21, Shear Joint Fatigue*; Aerospace Industries Association: Washington, DC, USA, 1997.
33. Hovanski, Y.; Curtis, A.; Michaelis, S.; Blackhurst, P.; Larsen, B. Advances in Refill Spot Welding Productivity. In *Friction Stir Welding and Processing XI*; Springer: Berlin/Heidelberg, Germany, 2021; pp. 189–197.

34. Carlone, P.; Palazzo, G.S. Influence of Process Parameters on Microstructure and Mechanical Properties in AA2024-T3 Friction Stir Welding. *Metallogr. Microstruct. Anal.* 2013, 2, 213–222.
35. Boccarusso, L.; Astarita, A.; Carlone, P.; Scherillo, F.; Rubino, F.; Squillace, A. Dissimilar friction stir lap welding of AA 6082-Mg AZ31: Force analysis and microstructure evolution. *J. Manuf. Process.* 2019, 44, 376–388.
36. Kush, P.M.; Carlone, P.; Astarita, A.; Scherillo, F.; Rubino, F.; Vora, P. Conventional and cooling assisted friction stir welding of AA6061 and AZ31B alloys. *Mater. Sci. Eng. A* 2019, 759, 252–261.
37. Fonda, R.W.; Bingert, J.F. Microstructural evolution in the heat-affected zone of a friction stir weld. *Metall. Mater. Trans. A* 2004, 35, 1487–1499.
38. Li, G.; Zhou, L.; Luo, L.; Wu, X.; Guo, N. Microstructural evolution and mechanical properties of refill friction stir spot welded alclad 2A12-T4 aluminum alloy. *J. Mater. Res. Technol.* 2019, 8, 4115–4129.
39. Lakshmi Balasubramaniam, G., Boldsai Khan, E., Fukada, S., Fujimoto, M., & Kamimuki, K. (2020). Effects of Refill Friction Stir Spot Weld Spacing and Edge Margin on Mechanical Properties of Multi-Spot-Welded Panels. *Journal of Manufacturing and Materials Processing*, 4(2), 55.
40. TW Metals Website. <https://www.twmetals.com/>, Accessed on March 6, 2021.
41. SAE AMS4272 Standard, SAE, 2015.
42. Sutep et al Sutep, J. (2016). Fatigue Fracture Mechanism and Damage Evaluation of Friction Stir Spot Welded AISI 1012 Cold Rolled-steel under Service Loading.
43. M. Janssen, J. Zuidema and R.J.H. Wanhill, Fracture Mechanics, ISBN 90- 407-2221-8, Second edition 2002
44. Tada, Paris, Irwin, The stress analysis of cracks handbook, Del Research Corporation, 1986
45. W. G Clark Jr. and S. J Hudak Jr., Variability in Fatigue Crack Growth Rate Testing, Journal of Testing and Evaluation, Volume 3, No. 6, pages 454- 476, 1975

46. W. G Clark Jr. and S. J Hudak Jr., The Analysis of Fatigue Crack Growth Rate Data, Application of Fracture Mechanics to Design, J.J. Burke and V. Weiss, Eds, Volume 22, Plenum, pages 67-81, 1979
47. A.E. Blom et al, Short fatigue crack growth in Al 2024 and AL 7075, symposium, Sheffield, EGF 1, Sept 1985
48. Mohanty, J. R., Verma, B. B., & Ray, P. K. (2010). Determination of fatigue crack growth rate from experimental data: a new approach. *International Journal of Microstructure and Materials Properties*, 5(1), 79-87.
49. Van Kranenburg, C. (2010). Fatigue crack growth in Aluminum Alloys.
50. J. Petit, Some aspects of near-threshold crack growth: Micro-structural and environmental effects, Proceedings of the international symposium on fatigue crack growth threshold concepts, Philadelphia, 1983
51. L. Lawson, E.Y. Chen, M. Meshii, Near-threshold fatigue: a review, *International Journal of Fatigue* 21, S15-S34, 1999
52. *NASMI312-4 Fastener Test Methods, Method 4, Lap Joint Shear*; Aerospace Industries Association: Washington, DC, USA, 1997.